



CENTRO DE INVESTIGACIÓN EN MATERIALES AVANZADOS, S.C.

DEPARTAMENTO DE ESTUDIOS DE POSGRADO

QUEEN MARY UNIVERSITY OF LONDON

**PIEZO-PHOTOCATALYSTS BASED ON POTASSIUM SODIUM NIOBATE AND
POLYACRYLONITRILE NANOFIBERS WITH REDUCED STABILIZATION
TEMPERATURE FOR THE DEGRADATION OF RHODAMINE B**

THESIS

**for obtaining a double degree in
MASTER IN MATERIALS SCIENCE**

Presents:

Britanny Melissa Klassen González

**Thesis supervisor:
Dr. Gabriel Rojas George**

**External supervisor (QMUL):
Dr. Joe Briscoe
External co-supervisor (QMUL):
Dra. Ana Belén Jorge Sobrido**

**LONDON, UK.
CHIHUAHUA, CHIH., MÉXICO**

NOVEMBER 2024

Abstract

Potassium sodium niobate ($\text{K}_{0.48}\text{Na}_{0.52}\text{NbO}_3$), also known as KNN, has emerged as a promising lead-free ceramic material due to its high piezoelectric coefficient up to 160 pC/N undoped, and its elevated Curie temperature above 400 °C. Additionally, its photocatalytic properties make it a strong candidate for applications combining it with piezoelectricity, known as piezo-photocatalysis. This type of catalysis is mostly used for environmental remediation, such as organic dye degradation like Rhodamine B (RhB). This study aims to develop composite materials by combining KNN particles with polyacrylonitrile (PAN), a polymer with excellent mechanical properties, and scalable synthesis via electrospinning, to enhance dye degradation performance.

The composite materials were synthesized using solid-state reaction for KNN and electrospinning for KNN-PAN fibers. Six samples, including two control groups (pristine PAN and KNN powder) and four composites with varying KNN loads based on the PAN content (10, 20, 30 and 40 wt%), were tested for their ability to degrade RhB using piezo-, photo- and piezo-photocatalysis.

With Rietveld refinement analysis, the existence of the orthorhombic phase in KNN powder was obtained with values of $\chi^2 = 3.78$, and R factors of $R_{wp} = 10.1$ and $R_{exp} = 5.19$, after reducing the calcination temperature from 900 °C to 800 °C, and composite fibers were successfully electrospun with ceramic particles. The required size for the particles was 100 nanometers, using ceramic powder from a post-calcination milling treatment. The KNN optical band gap was determined to be 3.94 eV, reduced to 3.92 eV after 12 hours of the post-calcination milling.

The most efficient samples for RhB degradation were the 10 wt% KNN composite, achieving 76.71% in piezocatalysis, and the 30 wt% KNN composite, with a degradation efficiency of 71.23% in photocatalysis. Finally, the KNN powder showed an enhanced piezo-photocatalytic activity with 54.02% degradation after three hours of testing. Notably, the 20 wt% KNN composite produced a significant color change in RhB, reaching the second place in piezo-photocatalysis after the ceramic powder, with a 45.46% degradation efficiency, suggesting its potential for enhanced degradation mechanisms even after five cycles.

Acknowledgements

First, I want to thank all the institutions that allowed me to finish this project: my scientific home CIMAV, and Queen Mary University of London.

I want to thank my wonderful supervisors, Dr. Gabriel Rojas George, Prof. Joe Briscoe and Prof. Ana Belén Jorge Sobrido, for being my guidance on my way to the Dark Side.

All my gratitude, love and acknowledgement go to my family, Eloy aka Bebé Gerber Joge Egviro, my mom Ofelia aka Laurita Garza, my dad Eloy aka Afedo, for being by my side even though an ocean separated our bodies, and to Oma and Opa as well. And an incredibly special place in my heart, and to whom I dedicate this thesis, Abuelito Alejandro, who taught me that being a scientist was one of the coolest things I could do, and who now will guide me from whichever place he rests.

I also want to thank my forever supporter and best friend, America. Thank you for being present in the distance. Thank you, Aarsha, for being such a lovely company while discovering London.

How could I not acknowledge the impact that my London family had in me, from my group pals: Chloe, Max, Raphael, Tingwei, Jorge, Subhajit, Emanuele, Yuan and Madsar from the Briscoe group, and Jesús, Mauricio, Carlos, Hattie, Michael, Jie, Natalia, Maadri and Vanessa from Ana's group. And my favorite people, the Mexicans: Mónica, Jesús, Anna, Ana Karen, Farid, Rogelio, Carlos, Adriana, Aldo, Augusto, David, Gabriel, Luis Ángel, Nelly and Ricardo.

I also want to thank all the technicians, researchers and students that helped me through this process.

And lastly, but not less important, I want to thank myself for finishing this thesis on a random Thursday night, for being so strong and brave, and crossing 8633 km away from home into a city that captured my heart forever.

Thank you, Bri xikita, we are a step closer to being the first and greatest Mennonite scientist of them all.

And a thank you to Griselda as well, little ball of purring fur that wrote her chunk of the thesis but was only readable in cat language.

Para mi Abuelito Alejandro,
Que me enseñó el mundo de los libros,
Lo precioso de la ciencia,
Y que la magia está presente
Aún en rompecabezas metálicos
Y en corazones de madera.

Y para ti, pequeña Bri,
Conquistaste Europa.
Sé lo mucho que te costó,
Pero henos aquí con 2 grados más
Y, técnicamente, es nuestro 2do libro.

Sigue haciendo 100cia.

I. Index

II. Figures List	7
III. Tables List	9
IV. Nomenclature and Abbreviations	10
V. Introduction.....	12
5.1. State of the Art.....	13
5.1.1. Potassium Sodium Niobate.....	13
5.1.2. Polyacrylonitrile.....	15
VI. Theoretical Framework	15
6.1. Potassium Sodium Niobate (KNN).....	15
6.1.1. Chemical and Physical Properties, and Applications.....	16
6.1.2. Synthesis Methods	18
6.2. Piezoelectricity and Ferroelectricity.....	19
6.3. Polyacrylonitrile (PAN).....	22
6.3.1. Carbon Nanofibers (CNF) Synthesis via Electrospinning	22
6.4. Catalysis	23
6.4.1. Photocatalysis	24
6.4.2. Piezocatalysis.....	25
6.4.3. Piezo-photocatalysis.....	27
VII. Justification	29
VIII. Hypothesis	30
IX. Objectives.....	30
9.1. General	30
9.2. Specifics.....	30
X. Experimental Methodology	31
10.1. Potassium Sodium Niobate Synthesis.....	31
10.2. Particle Size Reduction	31
10.3. Polyacrylonitrile Nanofibers Synthesis	32
10.4. Electrospinning Technique and Stabilization.....	32

10.5. Nanofibers Polarization Via Corona Poling.....	33
10.6. Characterizations	35
10.7. Catalysis Tests	36
XI. Results and Discussion	38
11.1. Potassium Sodium Niobate (KNN).....	38
11.1.1. XRD & TGA-DTA	38
11.1.2. Rietveld Refinement.....	44
11.1.3. SEM-EDS	46
11.1.4. UV-Vis.....	49
11.1.5. FT-IR	52
11.1.6. Raman Spectroscopy	53
11.2. Polyacrylonitrile (PAN) Fibers and KNN + PAN Composites.....	55
11.2.1. XRD & TGA-DTA	55
11.2.2. SEM	60
11.2.3. FT-IR	63
11.2.4. Raman Spectroscopy.....	64
11.2.5. Corona Poling.....	65
11.3. Catalysis Tests	67
11.3.1. Piezocatalysis.....	67
11.3.2. Photocatalysis	69
11.3.3. Piezo-photocatalysis	71
11.3.4. Analysis of Post-catalysis Tests	76
11.4. Summary of Results	80
XII. Conclusions	84
XIII. Recommendations.....	84
XIV. References.....	86

II. Figures List

Figure 1. Tetragonal crystallographic structure (group P4mm) from the potassium sodium niobate (KNN), drawn with the Vesta program [35].	16
Figure 2. Phase transition temperatures in KNN [34].	17
Figure 3. Representation of the ferroelectric domains alignment before and after applying an electric field.	20
Figure 4. Example of an electrical hysteresis loop. 1) Virgin material that has not been subjected to a previous electric field. 2) Maximum saturation polarization. 3) Remanent polarization after changing the direction of the field. 4) Coercive field, where the polarization value is 0. 5) Furthest polarization the material can hold in the opposite direction [70,71].	21
Figure 5. Chemical structure of polyacrylonitrile's monomer, acrylonitrile [75].	22
Figure 6. General scheme of electrospinning equipment, and the formation of the Taylor cone [79] at the tip of the needle.	23
Figure 7. Mechanism of a photocatalyst [86].	24
Figure 8. a) Piezocatalysis mechanism explained by Band Theory, just as it happens in photocatalysis. b) Piezocatalysis mechanism via screening effect [95].	26
Figure 9. MoS ₂ and KNbO ₃ nanorods when they work as piezo-photocatalysts [95].	27
Figure 10. Corona poling setup scheme.	33
Figure 11. Experimental methodology summarized in a flow diagram.	37
Figure 12. XRD pattern for KNN (K _{0.48} Na _{0.52} NbO ₃) powder calcined at 900 °C for 1 hour with the tetragonal 50:50 composition and the secondary phase K ₂ Nb ₄ O ₁₁ .	39
Figure 13. XRD pattern showing a pure phase acquired for 48:52 KNN.	40
Figure 14. TGA-DTA analysis of 48:52 KNN powder before calcination.	41
Figure 15. XRD patterns for the different calcination temperatures of K _{0.48} Na _{0.52} NbO ₃ , including a 50:50 composition and secondary phase.	42
Figure 16. XRD patterns for KNN powder milled post-calcination, from 0 to 14 hours.	44
Figure 17. a) XRD pattern done with Rietveld refinement, along the b) tetragonal and c) orthorhombic structures of K _{0.48} Na _{0.52} NbO ₃ obtained from the refinement.	45
Figure 18. SEM images from 48:52 KNN powder at different post-calcination milling times, including histograms from the particle size distribution: a) 0 hours, b) 2 hours, c) 4 hours, d) 6 hours, e) 8 hours, f) 10 hours, g) 12 hours and h) 14 hours.	48
Figure 19. Tauc plots for obtaining the optical band gap of KNN powder with post-calcination milling process: a) 0 hours, b) 6 hours and c) 12 hours.	51
Figure 20. Infrared spectra of the KNN powder a) before and b) after calcination.	52

Figure 21. a) Raman spectrum with deconvolution for 48:52 KNN composition; and b) Theoretical and experimental studies done by Saha et al. with the composition $K_{0.50}Na_{0.50}NbO_3$ [109].	55
Figure 22. a) XRD pattern for a 10 wt% pristine PAN sample stabilized at 250 °C for 2 hours; b) XRD pattern obtained for pristine PAN samples stabilized at 250 °C for different times, extracted from the study conducted by Lee et al. [113].	56
Figure 23. XRD patterns for the composite samples, including the tetragonal structure in the 50:50 KNN composition (PDF 00-061-0315).	57
Figure 24. TGA plot, showing the fibers with and without ceramic nanoparticles.	58
Figure 25. TGA-DTA of a) pristine PAN and b) 40 wt% KNN composite.	60
Figure 26. SEM images from pristine fibers and composite samples, stabilized at 250 °C for 2 hours, 10k magnifications. a) Pristine PAN, b) 10 wt% KNN composite, c) 20 wt% KNN composite, d) 30 wt% KNN composite, and e) 40 wt% KNN composite.	62
Figure 27. FT-IR spectra of pristine PAN and composite samples, with the following bonds: 1) Nb-O: 615 cm^{-1} ; 2) C=C-H: 806 cm^{-1} ; 3) C-O: 1365 cm^{-1} ; 4) C-C: 1451 cm^{-1} ; 5) C=C: 1587 cm^{-1} ; and 6) C≡N: 2243 cm^{-1} .	64
Figure 28. Raman spectra for a) pristine PAN and b) 20 wt% KNN composite, measured with a 442 nm laser.	65
Figure 29. Pristine PAN mat after corona poling. Image conditions: Samsung A14 5G, screenshot from a video.	66
Figure 30. SEM images from poled pristine PAN (a & b) and 30 wt% KNN (c & d) samples.	67
Figure 31. Piezocatalysis samples tested from 0 to 180 min, including the dye itself, the control groups and the composite materials.	69
Figure 32. Photocatalysis samples tested from 0 to 180 min, including the dye itself, the control groups and the composite materials.	71
Figure 33. Piezo-photocatalysis samples tested from 0 to 180 min, including the dye itself, the control groups and the composite materials.	72
Figure 34. Repetitions of the piezo-photocatalysis tests, with the best composite material (20 wt%), along with the control groups (pristine PAN and KNN powder). a) 2nd repetition; and b) 3rd repetition.	74
Figure 35. UV-Vis spectra from the third repetition samples from piezo-photocatalysis: a) pristine PAN, b) KNN powder and c) 20 wt% KNN composite; d) chemical structure of Rhodamine B [123].	76
Figure 36. Rhodamine B degradation, obtained from the third repetition of piezo-photocatalysis using 20 wt% KNN composite after a) 30 min, b) 60 min, c) 90 min, d) 120 min, e) 150 min and f) 180 min of degradation. Image conditions: Camera Canon EOS 1300D Rebel T6 with an 18 - 55 mm lens, f: 5, ISO: 400, focal distance: 41 mm, speed: 1/100 s, with a white background.	77

Figure 37. FT-IR spectra from the mats before and after being used in the catalysis tests.	78
Figure 38. Images comparing fibers from the same match, before and after the catalysis tests: a) pristine PAN, b) 10 wt% KNN composite, c) 20 wt% KNN composite, d) 30 wt% KNN composite, and e) 40 wt% KNN composite. Images conditions: Canon EOS 1300D Rebel T6 with an 18 - 55 mm lens, f: 5.6, ISO: 640, focal distance: 55 mm, speed: 1/100 s, with a white paper background.	79
Figure 39. a) Image taken of the 40 wt% KNN composite, showing the hole on the sample. Image conditions: Samsung Galaxy A14 5G, f: 1.8, ISO: 640, focal distance: 26 mm, speed: 1/30 s. b) The same sample after it was removed from the liquid and dried on a hot plate. Image conditions: Canon EOS 1300D Rebel T6, f: 5.6, ISO: 640, focal distance: 47 mm, speed: 1/100 s.	80

III. Tables List

Table 1. KNN-based ceramics, with their respective piezoelectric coefficient d_{33} (pC/N) and their Curie temperature (T_c), with the year in which the composition was reported.	15
Table 2. Summary of various applications from polyacrylonitrile composites with different inorganic fillers.	15
Table 3. Crystallite size calculation using the Scherrer equation from the XRD pattern shown in Figure 13.	43
Table 4. Rietveld refinement parameters obtained for tetragonal and orthorhombic phases for $K_{0.48}Na_{0.52}NbO_3$, compared to $K_{0.50}Na_{0.50}NbO_3$: lattice parameters (\AA), angles ($^\circ$) and cell volume (\AA^3) [98].	45
Table 5. Rietveld refinement parameters comparing the orthorhombic and tetragonal phases, individually and altogether, reporting R_{wp} , R_{exp} , χ^2 and the phases percentage (%).	46
Table 6. Average particle size with standard deviation (nm) from the KNN powder after the particle size reduction process with high energy milling.	49
Table 7. EDS results for the KNN samples before and after post-calcination milling in atomic percentage (at%), including theoretical values for $K_{0.48}Na_{0.52}NbO_3$	49
Table 8. Vibrational modes analyzed in Raman for KNN powder with a 48:52 composition, compared to a 50:50 KNN composition.	54
Table 9. Relation between the ceramic load in the samples and the shifting in the stabilization temperature ($^\circ\text{C}$), measured with TGA-DTA.	59
Table 10. Average nanofibers diameter (nm) from pristine PAN and composite materials measured from SEM images, and the voltage at which the solution was electrospinned.	63

Table 11. Average absorbance (a.u.) of the piezo-photocatalysis tests, including the first round and the two repetitions with the best performer (20 wt% KNN composite) and the control groups (pristine PAN and KNN powder).....75

IV. Nomenclature and Abbreviations

χ^2	Squared Chi (Rietveld refinement)
ϵ_r	Relative permittivity
ABO₃	General formula of a perovskite structure
AFM	Atomic Force Microscopy
at%	Atomic percentage
BT	Barium Titanate (BaTiO ₃)
C	Cubic crystallographic structure
C₃H₃N	Acrylonitrile chemical abbreviation, polyacrylonitrile monomer
CB	Conduction Band
cm	Centimeter
CNF	Carbon Nanofibers
<i>d</i>₃₃	Piezoelectric coefficient
DC	Direct Current
DMF	N,N-Dimethylformamide
DTA	Differential Thermal Analysis
E	Electric field
EDS	Energy-Dispersive X-ray Spectroscopy
eV	Electron Volt
FeRAM	Ferroelectric Random Access Memory
FT-IR	Fourier Transform Infrared spectroscopy
K	Dielectric constant (dimensionless)
K	Kelvin (temperature)
KNN	Potassium Sodium Niobate (K _{1-x} Na _x NbO ₃)
kV	Kilovolt
mg	Milligram
min	Minute

ml	Milliliter
mm	Millimeter
MPB	Morphotropic Phase Boundary
N₂	Nitrogen gas
nm	Nanometer
O	Orthorhombic crystallographic structure
PAN	Polyacrylonitrile
pC/N	Picocoulombs per Newton (Piezoelectricity coefficient units)
PFM	Piezoresponse Force Microscopy
pm/V	Picometre per Volt (Piezoelectricity coefficient units)
ppm	Parts per million
P_r	Remanent polarization
PZT	Lead Zirconate Titanate (PbZr _{1-x} Ti _x O ₃)
R	Rhombohedral crystallographic structure
R	Residual factor (Rietveld refinement)
Redox	Reduction and oxidation chemical reactions
R_{exp}	Expected <i>R</i> factor (Rietveld refinement)
RhB	Rhodamine B, organic dye
R_{wp}	Weighted profile <i>R</i> factor (Rietveld refinement)
SEM	Scanning Electron Microscopy
T	Temperature (°C)
T	Tetragonal crystallographic structure
T_c	Curie temperature (°C)
T_g	Glass transition temperature (°C)
TGA	Thermogravimetric Analysis
TTB	Tetragonal Tungsten-Bronze, variant of the tetragonal structure
US	Ultrasonic
UV-Vis	Ultraviolet-Visible Spectroscopy
VB	Valence Band
wt%	Weight percentage
XRD	X-Ray Diffraction

V. Introduction

Piezoelectric materials have evolved since their discovery and description by the Curie brothers in the late 19th century, who were intrigued by why an electric response was produced after applying mechanical stresses to certain materials. The first materials used to describe this phenomenon were the Rochelle salts and quartz, studied by Walter Guyton Cady in 1921 to generate electrical oscillators [1][1].

Piezoelectricity is a property of materials whose crystalline structure is non-center-symmetric, when applying mechanical stress or strain produces an electrical response, and vice versa: when an electric field is applied, there is a mechanical deformation. This property is directly linked to the Curie temperature (T_c), a phase transition temperature, where materials lose their piezoelectricity by modifying their crystalline structure [2][2].

During the Second World War, barium titanate (BaTiO_3 , abbreviated as BT) was used for the construction of sonar and radar devices due to its dielectric constant, K (between 1200 and 1500) and its Curie temperature (120 °C). Unfortunately, its relatively low TC makes the use of BT in other possible applications difficult [3][3]. In 1952, lead zirconate titanate, abbreviated as PZT, which exceeds the dielectric ($K = 1700$) and piezoelectric constants ($d_{33} = 600 \text{ pC/N}$) of barium titanate, began to be studied [4][4]. The problem with PZT is the presence of lead, which sometimes reaches up to 60% by weight of the total compound, thus leading to the search and study of other lead-free ceramic materials, such as potassium sodium niobate ($\text{K}_{1-x}\text{Na}_x\text{NbO}_3$, abbreviated as KNN).

On the other hand, semiconductor materials, such as ceramics, have been developed for catalytic applications, specifically those procedures that are activated by sunlight, known as photocatalysts. Various materials have been used, such as oxides, arsenides, nitrides, various polymers such as polyacrylonitrile and lignin, pure elements such as silicon and phosphorus, among others. The mechanism in photocatalysis is as follows: the electrons in the valence band (VB) get excited by the energy in sunlight in a semiconductor material, which then jump to a higher energy level known as the conduction band (CB), creating a pair of electron-hole. These pairs have enough energy to produce reduction-oxidation sites (Redox),

where the environment that surrounds the photocatalyst reacts in these sites like breaking or creating chemical bonds [5]5. Photocatalysts have been used in the treatment of atmospheric pollutants, either in aqueous media or in air, as well as in generation of solar fuels [6]6.

In this work we will delve into potassium sodium niobate (KNN), including its properties and synthesis methods, as well as polyacrylonitrile (PAN) as a support material for the ceramic material, where we seek to take advantage of the piezo-photocatalytic effect of both KNN and PAN. Other concepts such as piezoelectricity and photocatalysis will be described separately, leading to the piezo-photocatalytic effect, a combination of both. This work also covers the experimental methodology by which potassium sodium niobate nanoparticles will be synthesized and embedded in carbon nanofibers from polyacrylonitrile for applications in the degradation of organic dyes.

Then, the state of the art of the different piezoelectricity values obtained is developed, from the first studies of its structure to the highest values reported so far for KNN.

5.1. State of the Art fibers

The first records of the synthesis of potassium sodium niobate ($K_{1-x}Na_xNbO_3$) are by Shirane *et al.* in 1954, where the dielectric properties of sodium niobate and KNN were studied [7]. In this study, the phase diagram between potassium niobate ($KNbO_3$) and sodium niobate ($NaNbO_3$) as well as the lattice parameters were obtained by X-ray diffraction (XRD) in a study to understand the phase transitions at different temperatures and with different compositions between sodium and potassium.

Piezoelectric measurements of KNN began with a 50:50 ratio of K to Na. Subsequently, this ratio was varied, where $x=0.48, 0.49, 0.50, 0.505, 0.51, 0.515, 0.52, 0.525, 0.53$ and 0.54 in the $K_{1-x}Na_xNbO_3$ composition. Dai *et al.* performed this study in 2009, obtaining the highest piezoelectricity value at 160 pC/N when $x=0.52$ [8]8. Saito *et al.*, in 2004, started to investigate the concept of morphotropic phase boundary in KNN, where the piezoelectricity increases with phase coexistence. In

the case of this study, they worked with the synthesis of potassium niobate with lithium and tantalum with the composition $\{(K_{0.50}Na_{0.50})_{1-x}Li_x\}(Nb_{1-y}Ta_y)O_3$, where $x=0.06, 0.04, 0.03$, and $y=0, 0.10, 0.20$, in addition to the composition $(K_{0.44}Na_{0.52}Li_{0.04})(Nb_{0.86}Ta_{0.10}Sb_{0.04})O_3$. The latter is the one with the highest d_{33} value of 416 pC/N, obtained at $T_c=253$ °C, comparable to the 410 pC/N of PZT4 [9]9.

Within the research scope for this work, the KNN composition that has reported the highest value of piezoelectric constant (d_{33}), synthesized by Li *et al.* in 2018 by molten salts, was $0.96(K_{0.50}Na_{0.50})(Nb_{0.965}Sb_{0.035})O_3-0.01CaZrO_3-0.03(Bi_{0.50}K_{0.50})HfO_3$, abbreviated as (96KNNS-1CZ-3BKH). This composition reached a d_{33} value ≈ 700 pC/N, with a Curie temperature (T_c) of 242 °C. The d_{33} was also measured in a temperature range of 25 to 150 °C, which is a range where some of the applications of piezoelectric materials work, obtaining values of 540 pC/N, close to the values reported for some variants of lead zirconate titanate (PZT), such as PZT-5H, a variant of PZT with enhanced piezoelectric properties, with 590 pC/N reported [10]10. Table 1 lists the compositions of KNN that have been worked on, with the values of d_{33} with their respective Curie temperature.

As the piezoelectric constant increases, the Curie temperature decreases, although there does not appear to be a linear decrease; most of the compositions reviewed are between 200 and 270 °C, with values above 400 pC/N. Lithium and antimony are usually found in the compositions, and as the value of d_{33} increases, the amount of compounds present increases, reaching three types of perovskites with ~ 700 pC/N, which are sodium potassium niobate antimonate, calcium zirconate and bismuth potassium hafnate.

Table 1. KNN-based ceramics, with their respective piezoelectric coefficient d_{33} (pC/N) and their Curie temperature (T_c), with the year in which the composition was reported.

Composition	d_{33} (pC/N)	T_c (°C)	Year	Reference
0.96(K_{0.5}Na_{0.5})(Nb_{0.965}Sb_{0.035})O₃-0.01CaZrO₃-0.03(Bi_{0.5}K_{0.5})HfO₃	~ 700	242	2018	[10] 10
(1-x-y)K _{1-w} Na _w Nb _{1-z} Sb _z O ₃ -yBaZrO ₃ -xBi _{0.5} K _{0.5} HfO ₃	570	~ 200	2016	[11] 11
[Li _{0.06} (K _{0.9} Na _{0.1}) _{0.94}](Nb _{0.9} Ta _{0.1})O ₃ - 25 wt% MnO ₂	545	~ 250	2017	[12] 12
(1-x)K _{0.4} Na _{0.6} Nb _{0.96} Sb _{0.04} O ₃ -x(Bi _{0.45} Sm _{0.05})Na _{0.5} ZrO ₃	~ 508	~ 268	2020	[13] 13
(1-x)(K _{0.48} Na _{0.52})(Nb _{0.95} Sb _{0.05})O ₃ - xBi _{0.5} Ag _{0.5} ZrO ₃	490	~ 200	2014	[14] 14
(1-x)K _{0.4} Na _{0.6} Nb _{0.96} Sb _{0.04} O ₃ -xBi _{0.5} K _{0.5} Zr _{0.9} Hf _{0.1} O ₃	451	258	2017	[15] 15
(1-x)(K _{0.5} Na _{0.5}) _{0.98} Ag _{0.02} (Nb _{0.96} Sb _{0.04})O ₃ -x(Bi _{0.5} Na _{0.5})ZrO ₃	~ 440	~ 250	2019	[16] 16
0.96(K_{0.5}Na_{0.5})_{0.95}Li_{0.05}Nb_{0.93}Sb_{0.07}O₃-0.04CaZrO₃	420	~ 250	2020	[17] 17
{(K _{0.5} Na _{0.5}) _{1-x} Li _x }(Nb _{1-y} Ta _y)O ₃	416	~ 250	2004	[9] 9
(K _{0.48} Na _{0.52})NbO ₃	160	410	2009	[8] 8

181920212223,

The used and33

VI. Theoretical Framework

6.1. Potassium Sodium Niobate (KNN)

Potassium sodium niobate (KNN) is a ceramic material with the chemical formula K_{1-x}Na_xNbO₃ [\[18\]](#)34, whose crystalline structure is shown in [Figure 1](#). The color representation per atom is as follows: sodium is shown in purple, potassium in gray, niobium in green, and oxygen in red.

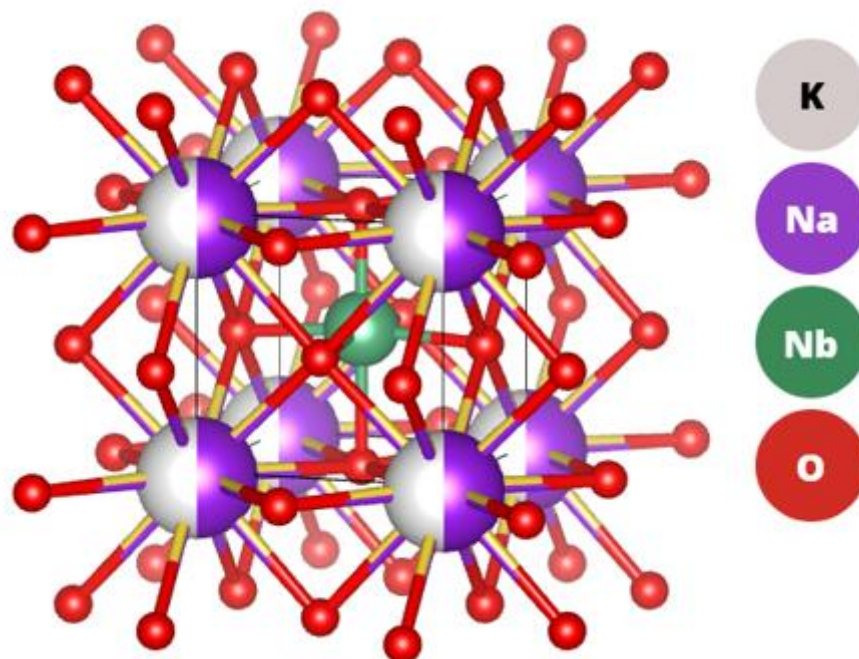


Figure 1. Tetragonal crystallographic structure (group $P4mm$) from the potassium sodium niobate (KNN), drawn with the Vesta program [19]35.

KNN has been studied as a possible substitute for lead zirconate titanate (PZT), mainly for its piezoelectric properties, and its Curie temperature (T_c), in applications such as actuators, sensors, and energy harvesters [20]36.

In the following sections, its physical and chemical properties, synthesis methods, and the applications in which it has been used will be discussed in more detail, comparing KNN with other ceramic materials.

6.1.1. Chemical and Physical Properties, and Applications

KNN has a perovskite-type crystal structure, with formula ABO_3 , where the A-site is occupied by potassium and sodium, and niobium occupies the B-site. Among the crystalline structures it can present are rhombohedral (R) with space group $R\bar{3}m$, orthorhombic (O) with space group $Amm2$, tetragonal (T) with space group $P4mm$, and cubic (C) with space group $Pm\bar{3}m$ [21]37. The phase transition temperatures (T), which can be visualized in the phase diagram in Figure 2, are: $T_{R-O} = -123^\circ\text{C}$ [34]18, [22]38, $T_{O-T} = 210^\circ\text{C}$ [18]34, [22]38, $T_{T-C} = 410^\circ\text{C}$ [18]34, [22]38, [23]39; the last transition temperature coincides with the Curie temperature (T_c) of KNN [22]38. The

Curie temperature, which is another phase transition temperature, in ceramic materials causes the loss of piezoelectric and ferroelectric properties [24]40.

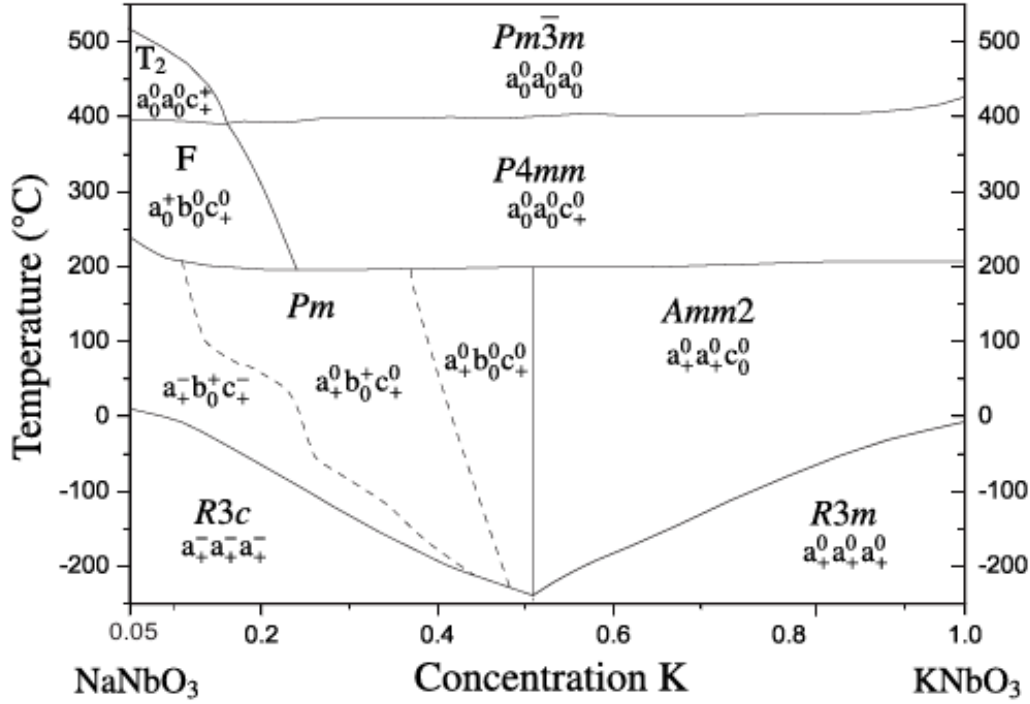


Figure 2. Phase transition temperatures in KNN [18]34.

KNN a piezoelectric material exhibits a piezoelectric constant (d_{33}) that has reached values of 490 pC/N with a composition $(1-x)(K_{0.48}Na_{0.52})(Nb_{0.95}Sb_{0.05})O_3 - xBi_{0.50}Ag_{0.50}ZrO_3$, synthesized by Wang *et al.* in 2014 [14]. In another study, carried out by Xu *et al.* in 2016, by means of a ternary system with $K_{1-x}Na_xNb_{1-y}Sb_yO_3 - BaZrO_3 - Bi_{0.50}K_{0.50}HfO_3$, a maximum d_{33} value of 570 pC/N was achieved, close to the 590 pC/N presented by PZT-5H [11]. Undoped KNN has a d_{33} value of 80 to 160 pC/N [2], and a $TC = 410^\circ C$ [4]. The range between 80 and 160 pC/N in pure KNN is due to the atomic percentage ratio of sodium to potassium, where a higher amount of Na decreases the piezoelectric constant [2]. These two characteristics are the ones that have boosted its study as a substitute material for PZT in some applications, as mentioned above. It is not the only lead-free ceramic material that has been studied; other candidates include barium titanate ($BaTiO_3$), bismuth sodium titanate ($Bi_xNa_{1-x}TiO_3$), bismuth sodium zirconate titanate ($Bi_xK_{1-x}TiO_3$),

potassium tantalate (KTaO_3), bismuth ferrite (BiFeO_3), among others [2339,2541,2642].

The morphotropic phase boundary (MPB) is the phase coexistence boundary where the piezoelectricity is higher compared to a single phase [27]43, mainly studied in PZT. In the case of KNN, the phases that coexist and where a higher piezoelectricity has been found are with the orthorhombic and tetragonal phases, and it is found in a composition where $x=0.52$ in $\text{K}_{1-x}\text{Na}_x\text{NbO}_3$, studied by Saito *et al.* in 2004, where its piezoelectricity value (490 pC/N with this composition) begins to be related to the coexistence of tetragonal and orthorhombic phases [9].

The optical properties of KNN are also important, as it is a semiconductor material with a band gap energy between 3.2 and 3.6 eV in bulk [28]44. This property is applied in photocatalytic systems, such as hydrogen generation from water splitting, dye degradation and in smart windows as a photochromic material [2844-3046].

Among other physical properties of KNN, it has a dielectric constant (ϵ_r) between 272 and 648 [31]47, and a remnant polarization (P_r) of up to 33 $\mu\text{C}/\text{cm}^2$ when K^{1+} and Na^{1+} are at a ratio of 0.5 each [32]48, and its calculated density for pellets is 4.26 g/cm^3 [33]49. The piezoelectric and dielectric properties of KNN have been applied in transducers [34]50, energy harvesters [3551,3652], and even in biomedical applications for antibacterial responses [37]53.

6.1.2. Synthesis Methods

Potassium sodium niobate is a solid solution of potassium niobate (KNbO_3) and sodium niobate (NaNbO_3), which can be synthesized by different methods, depending on whether powders, ceramics or films are sought. KNN ceramic powders can be synthesized by physical methods such as molten salt [39]54 or solid state [40]55, or by chemical methods such as sol-gel [41]56 or hydrothermal [42]57. The selection of the methodology is made based on the reagents and equipment available, as well as the general characteristics of the KNN sought, such as particle size, grain size, as a matrix or reinforcement in a composite material, among others.

Employing solid state, which can be done with manual or high energy milling, powders with micrometric particle size are obtained, which can be reduced by post-

calcination milling. The precursors generally used for this methodology are sodium and potassium carbonates (Na_2CO_3 and K_2CO_3) and niobium oxide (Nb_2O_5). The calcination temperature can range from 600 to 900 °C, while the sintering temperature does not exceed 1140 °C, due to the volatilization of potassium and sodium ions, as shown in the phase diagram in [Figure 234](#). Milling times are usually between 2 and 24 hours, both dry and wet, generally using ethanol as a process control agent [\[43\]](#)⁵⁸.

6.2. Piezoelectricity and Ferroelectricity

Within the classification of materials, specifically in ceramics, there is a category of dielectric materials; these materials have a set of specific characteristics, and based on them, phenomena such as ferroelectricity and piezoelectricity occur [\[59-61\]](#).

At the end of the 19th century, the brothers Pierre and Jacques Curie studied piezoelectric materials, where applying mechanical stress produces an electrical response, and vice versa: by inducing an electric field, there is a mechanical deformation [\[62-64\]](#). The piezoelectric coefficient, quantified in picocoulombs per Newton (pC/N), can be calculated using the following equations [\[63\]](#):

$$D = d \cdot T + \varepsilon^T E \quad (1)$$

$$S = s^E T + d \cdot E \quad (2)$$

Where:

D = Dielectric displacement

T = Elastic tension

E = Electric field vector

S = Stress tensor

S^E = Stress tensor in the presence of an electric field

d = Piezoelectric coefficient

ε^T = Electric permittivity

Piezoelectric materials have been used in many general and technological applications, such as cigarette lighters, energy harvesters, Ferroelectric Random Access Memory (FeRAM), photovoltaic cells, sensors and actuators [\[65\]](#).

For piezoelectricity to exist in a crystal, it must have a perovskite-type structure32-point, with the formula ABO_3 , where it is an oxide of a metal A and a metal B, generally with the atomic radius of A being greater than that of B. Perovskites have a non-center-symmetrical structure, such as rhombohedral, orthorhombic or tetragonal structures [661].

In piezoelectric materials, there are both natural and synthetic ones; silk, quartz and topaz are examples of natural piezoelectrics, while among the best-known synthetic materials are PZT, barium titanate, tantalates, and lithium, potassium and sodium niobates ($ATaO_3$ or $ANbO_3$, where $A=Li, K, Na$) [65,67,683]. Speaking specifically of KNN, the orthorhombic phase has the highest piezoelectricity value, with values of 210 pC/N with cation substitutions [48,694].

After the description of piezoelectricity, the concept of ferroelectricity arises. Ferroelectricity, as well as piezoelectricity, requires non-centrosymmetric crystal structures; when an electric field is applied to a material, its ferroelectric domains will align with the applied field, as shown in Figure 3 [66,70,71].

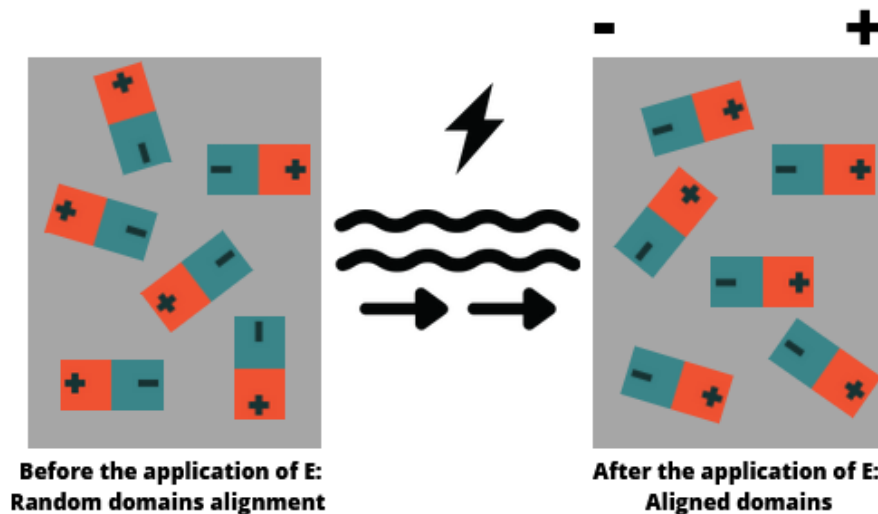


Figure 3. Representation of the ferroelectric domains alignment before and after applying an electric field.

When the electric field is removed, the domains do not return to their initial position but are slightly deflected from the direction they took according to the electric field (E). This position is known as remnant polarization and can be measured by

means of an electrical hysteresis loop (Figure 4). When the application of the electric field is initiated, the material will reach the point of maximum saturation, where, no matter how much field is applied, no further polarization can occur.

When the field is withdrawn, the polarization will start to decrease, until it reaches the coercive field (polarization equal to 0). An electric field is applied in the opposite direction, and a negative saturation polarization will also occur. Once the field is applied again in the initial direction, the cycle is repeated. Materials that have not previously been subjected to any electric field start at the origin of the graph, but never recover this initial state [705,716].

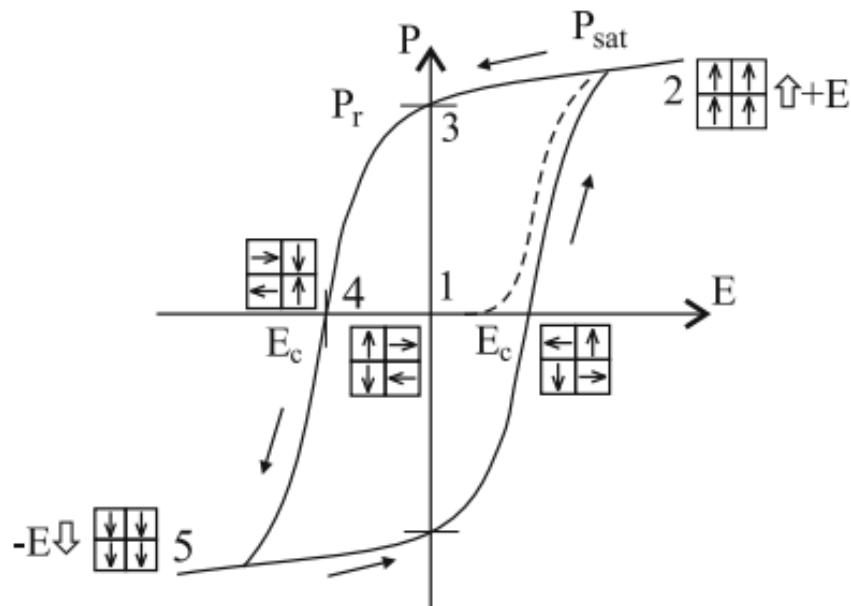


Figure 4. Example of an electrical hysteresis loop. 1) Virgin material that has not been subjected to a previous electric field. 2) Maximum saturation polarization. 3) Remanent polarization after changing the direction of the field. 4) Coercive field, where the polarization value is 0. 5) Furthest polarization the material can hold in the opposite direction [70,71].

Ferroelectric materials have been applied in electronic devices, such as RAM and batteries, mentioned above; in energy applications, such as energy harvesters and photovoltaic cells; and even in biomedical applications [57].

6.3. Polyacrylonitrile (PAN)

Polyacrylonitrile (PAN) is a polymer with the repeating acrylonitrile (C_3H_3N) unit (Figure 5), which has been used for carbon nanofiber production by electrospinning, as well as in energy storage applications, as reinforcement in polymeric matrices, water remediation, agricultural welfare, and even in medical applications as a biomaterial [72-75].

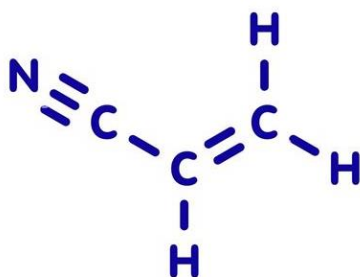


Figure 5. Chemical structure of polyacrylonitrile's monomer, acrylonitrile [75].

The high carbon content (from 66 to 92 wt%), the flexibility it possesses as carbon nanofibers (CNF), as well as high porosity and surface area, are outstanding properties of PAN [74,76]. These characteristics have well defined the applications mentioned above. Despite being a polymer known since the 19th century, its synthesis has been complicated due to its difficulty in solvation [77].

6.3.1. Carbon Nanofibers (CNF) Synthesis via Electrospinning

Among the various methods of nanofiber synthesis, the electrospinning technique has been mostly studied because of the terminal characteristics of the nanofibers, such as their diameter, between 10 nm and 10 μ m, which is related to the concentration of monomer in the solvent [78]. The technique consists of introducing a polymer into solvent through a syringe, where the flow is controlled with the help of an electric field. As the polymer exits the syringe, a phenomenon known as a Taylor cone is generated (Figure 6) [79], where the solvent evaporates, and the polymer fibers randomly fall onto a metal plate. CNFs are porous, with an approximate diameter between 5 and 50 nm [80].

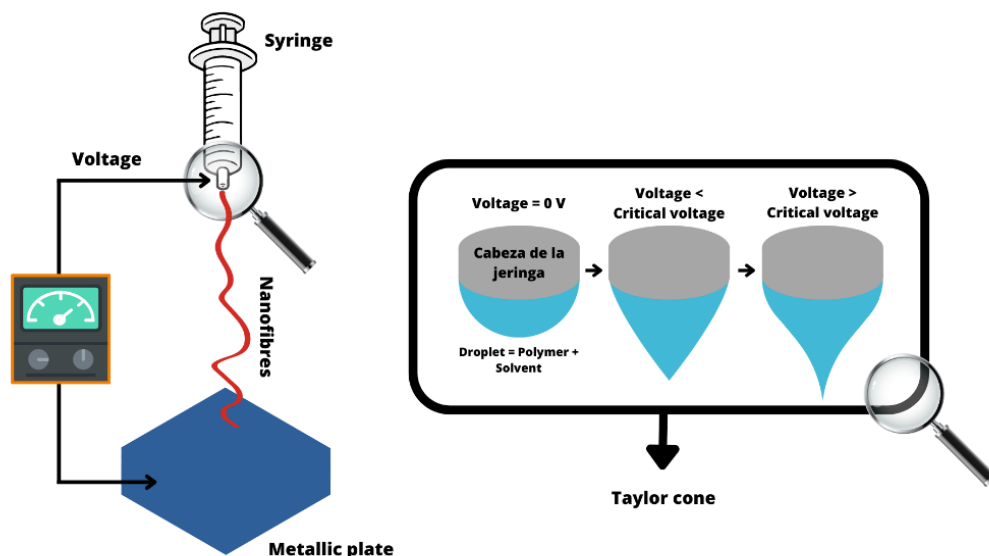


Figure 6. General scheme of electrospinning equipment, and the formation of the Taylor cone [79] at the tip of the needle.

Process variables are the fluid mechanics related to the polymer and the solvent, with an average polymer concentration of 8 to 15% by weight; viscosity (between 1 and 20 poises), surface tension, temperature (the process is generally carried out at room temperature), humidity, as well as the electrical potential to which the system is subjected (9 to 25 kV) and the separation from the syringe to the metal plate (10 to 20 cm) [78,81-83].

6.4. Catalysis

For a chemical reaction to be carried out, it requires a certain energy, generally known as activation energy, which the reactants must overcome to break their bonds and form new ones, resulting in products, which are new chemical species. Certain reactions require such a high activation energy that the products do not form; in these cases, it is necessary to add an external source that lowers the activation energy, and the reaction is carried out. These external sources are known as catalysts and can be atoms, molecules, or more complex structures, such as enzymes, or even other process variables, such as temperature [84,85].

6.4.1. Photocatalysis

Within catalysis, there is a process known as photocatalysis: the incidence of electromagnetic radiation, especially in the ultraviolet-visible (UV-Vis) region, which moves electrons from the valence band to the conduction band of a material. Photocatalysis has various applications related to degradation, such as water splitting, degradation of air pollutants, and generation of biodiesel from organic waste [86].

Figure 7 describes the mechanism of action of a photocatalyst: a semiconducting material, with a given band gap energy, is incident by photons, where the promotion of electrons in the valence band (VB) to the conduction band (CB) takes place. The promoted electron leaves a hole in the VB, which results in a potential difference and causes the rest of the electrons in the VB to move and reach a minimum energy state. This interaction between holes and electrons generates reduction-oxidation (redox) reactions with chemical species in the surrounding medium (air, solutions, etc.) and thus generates or degrades bonds [86,87].

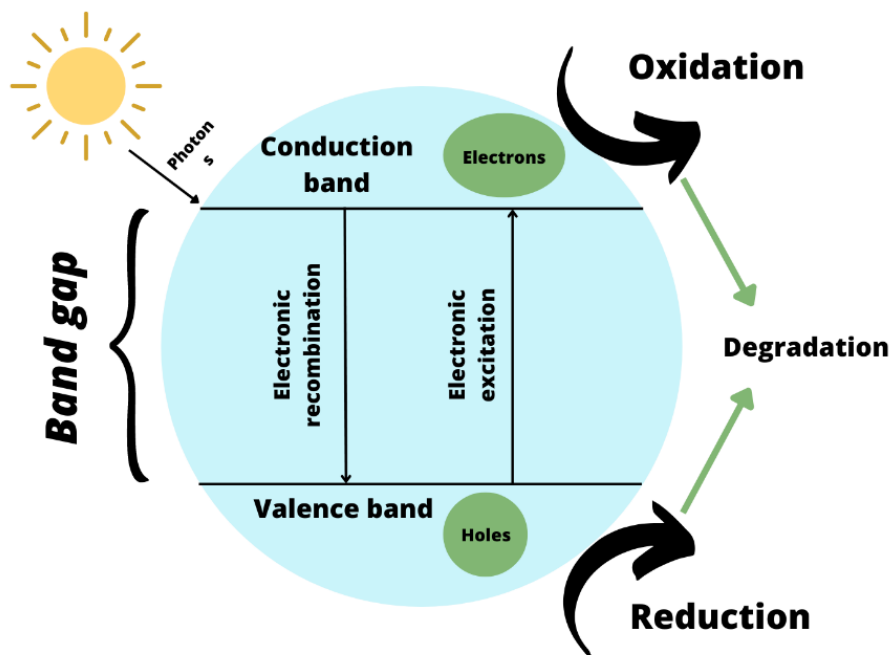


Figure 7. Mechanism of a photocatalyst [86].

Some parameters to consider for photocatalytic applications include catalyst concentration, light intensity, pH value, and catalyst composition [86].

Titanium dioxide (TiO₂) is one of the most widely studied and used materials due to its abundance, compared to platinum and ruthenium. TiO₂ has high stability to degradation and oxidation when in contact with sunlight, as well as being easy to synthesize by 'soft' methods, such as sol-gel. One of the disadvantages is the range in which it can absorb light, which is in the ultraviolet and blue region of the visible light spectrum, as well as rapid recombination between electron-hole pairs, which decreases its efficiency when carrying out redox reactions [85-91].

These disadvantages have led to the synthesis of other materials, either organic or inorganic, which have higher performance and can further expand the applications of photocatalysis, such as KNN. The photocatalytic activity of KNN has been applied mostly for dye degradation and hydrogen production. Regarding the dye degradation, Kujur *et al.* [44] and Lun *et al.* [92] studied the degradation of Rhodamine B (RhB) with KNN as nanoparticles and ceramics, with an effectiveness above 90% after one hour of photocatalysis test. Another dye that has been tested is Basic Blue 41 (BB41), by Praxedes *et al.*, in this case with the 50:50 composition in KNN, and an effectiveness of 95% after six hours in a basic pH (pH = 10) [93]. In these three cases, the nanoparticles or ceramics were poled with corona poling [44] or direct contact polarization [92,93].

6.4.2. Piezocatalysis

Just as solar radiation is responsible for activating the catalytic function of a photocatalytic material, piezocatalysis takes advantage of the piezoelectricity of materials to carry out catalytic processes. Piezocatalysis can occur by means of two mechanisms (Figure 8): by means of Band Theory (CB and VB) as in photocatalysis, and the second is the screening charge effect. The screening effect 'divides' the charges within the piezoelectric material by polarization, and the medium in which the material is located will organize its charges based on the charges on the surface of the material [94].

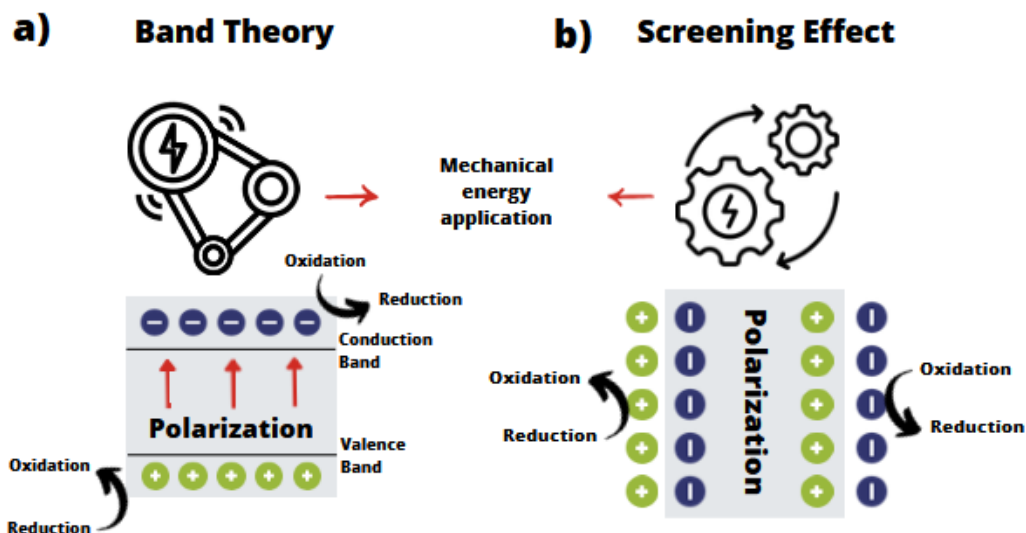


Figure 8. a) Piezocatalysis mechanism explained by Band Theory, just as it happens in photocatalysis. b) Piezocatalysis mechanism via screening effect [95].

The piezoelectric coefficient potential used to describe piezocatalysis is known as the piezopotential, i.e. the efficiency of charges to polarize in the material in the presence of mechanical stress specifically for catalytic mechanisms. According to the literature review, the mechanism that is mostly presented is the shielding effect, being a little more descriptive when talking about the piezocatalysis event [94,96].

In 2006, Wang and Song synthesized zinc oxide (ZnO) nanowires on an alumina substrate by placing gold droplets on the tip of the nanowires. Employing Atomic Force Microscopy (AFM), the piezopotential of these nanowires was measured, for their subsequent application as electrical nanogenerators. The synthesis of this type of material at the nanoscale makes it possible to harness the mechanical energy produced by small forces such as falling raindrops or noise [97].

This work on ZnO nanowires marks the beginning of a new application for piezoelectric materials: catalysis. In addition to zinc oxide, other ceramic materials already known for their piezoelectric coefficient have been used, such as BaTiO₃, calcium titanate (CaTiO₃), molybdenum selenides and sulphides (MoSe₂, MoS₂), and potassium sodium niobate (K_{1-x}Na_xNbO₃) [94,95].

6.4.3. Piezo-photocatalysis

The piezo-photocatalysis process starts with the piezopotential in the material: the material is subjected to a mechanical deformation or stress, which promotes an electrical polarization. This polarization aligns the charges, and the electron-hole pair generation process is more effective, causing the incidence of light to activate the excitation of electrons to the conduction band. In this way, a larger number of reaction sites are available, but with much less electronic recombination due to the electrical polarization derived from piezoelectricity. In addition, the electric polarization allows a bend in the VBs and CBs, which could generate indirect bands and, thus, a greater difficulty for electronic recombination.

Most of the applications in which piezo-photocatalysis has been used are for the degradation of organic dyes, such as Rhodamine B or methylene blue, and for obtaining hydrogen from the cleavage of the water molecule [92,95,98]. A scheme studied for a molybdenum sulfide (MoS_2) material with potassium niobate (KNbO_3) is presented in Figure 9.

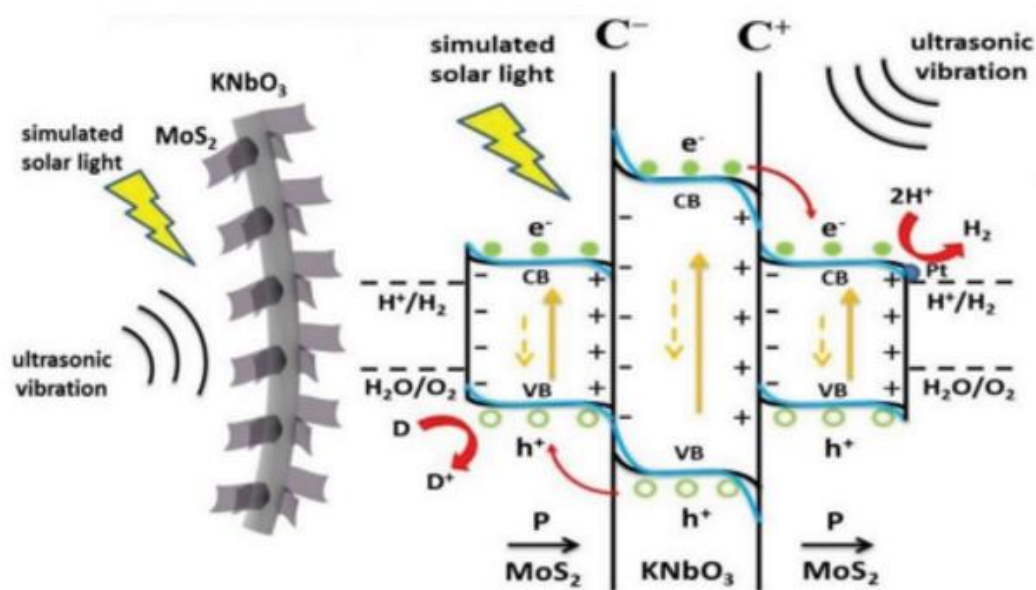


Figure 9. MoS_2 and KNbO_3 nanorods when they work as piezo-photocatalysts [95].

The diagram initially schematizes how a KNbO_3 skeleton with MoS_2 inlay is subjected to ultrasonic vibrations and simulated sunlight. In the second part of the

schematic, a picture of how the holes in the VB of KNbO_3 move to the VB of MoS_2 by the action of sunlight (photocatalysis), bending the bandgap of both materials is depicted. The electrons that were excited to the CB of KNbO_3 move to the CB of the next MoS_2 structure by the action of ultrasonic vibrations. These contributions cause a modification in the bands, as mentioned above, so that the active sites occur both in the regions where there are more holes and in the area with the highest concentration of electrons.

It is this effect that we seek to highlight in potassium sodium niobate (KNN), given its piezoelectric properties, where up to 570 pC/N response has been achieved, and optical, with a band gap that has reached up to 2.2 eV, it is a good option for piezo-photocatalytic applications.

VII. Justification

Potassium sodium niobate, with an atomic ratio of 0.48 K¹⁺ and 0.52 Na¹⁺, has been studied for presenting the highest piezoelectric constant values, reaching up to 160 pC/N when pure. Speaking of KNN used as a photocatalyst, generally the ratio is 0.50 K - 0.50 Na, obtaining band gap values like other semiconductor materials, such as TiO₂.

Taking advantage of the piezoelectricity of KNN with this ratio, and its photocatalytic properties, has opened a new possibility of application as a piezo-photocatalyst. This work allows exploring this area of piezo-photocatalysis, using KNN individually or embedded as nanoparticles in carbon nanofibers synthesized from different polymeric materials, such as polyacrylonitrile.

PAN has, in turn, been used as a photocatalyst for hydrogen production. KNN has been tested with other polymers, such as PVDF, which is a piezoelectric polymer, but embedding nanoparticles in carbon nanofibers from PAN has been little reported, and the photocatalytic activity of the polymer may be overcome by including KNN, both for its piezoelectric property and photocatalytic property.

The aim is to treat pollutants, such as the degradation of Rhodamine B, which are organic dyes. This process is carried out by means of photocatalysis, which is enhanced by the piezoelectric effect of the material, in this case KNN.

VIII. Hypothesis

Potassium sodium niobate, with an atomic relation of 0.48 K – 0.52 Na and a particle size below 100 nm, will reduce the band gap in the range employed for piezo-photocatalytic applications of dye degradation as powder electrospun .

IX. Objectives

9.1. General

Synthesize piezo-photocatalysts based on pure potassium sodium niobate for pollutants treatment.

9.2. Specifics

Synthesize potassium sodium niobate powders, with a stoichiometric relation of 0.48 K – 0.52 Na through solid-state route, optimizing the milling time.

Find the optimal calcination temperature with a temperature scanning.TA (Thorn Scientific STA1500).

Identify the crystallographic structure of the ceramic powders via X-Ray Diffraction (X'Pert Pro, CuK α 1.541874 Å).

Measure the particle size with images from Scanning Electron Microscopy (FEI Inspect F).

Analyze the morphology via Scanning Electron Microscopy.

Determine the optical band gap for KNN with Ultraviolet-Visible Spectroscopy (Perkin Elmer Lambda950 UV-vis spectrometer).

Produce composite materials of KNN nanoparticles in polyacrylonitrile with the electrospinning technique.

- Test the piezo-, photo- and piezo-photocatalytic activity, with the individual and composite materials.

X. Experimental Methodology

10.1. Potassium Sodium Niobate Synthesis

The synthesis of $(K_{0.48}Na_{0.52})NbO_3$ was achieved with a solid-state reaction, using potassium carbonate (K_2CO_3 , ACS reagent $\geq 99.0\%$, Sigma-Aldrich), sodium carbonate (Na_2CO_3 , BioXtra $\geq 99.0\%$, Sigma-Aldrich) and niobium oxide (Nb_2O_5 , 99.9%, trace metals basis, Sigma-Aldrich) as precursors.

Before weighing the precursors, and to avoid any retained humidity due to the hygroscopic nature of the potassium and sodium carbonates, these two reagents were dried in a box furnace (Carbolite Box Furnace 1100) for 24 hours at $150\text{ }^{\circ}\text{C}$. The solid-state reaction was manually carried out with agate mortar, pestle, and acetone as a process control agent. After drying, a first dry mill was completed to homogenize the powder and break down agglomerates for 15 minutes. Afterward, acetone was added to the powder and milled in circular movements for 2 hours, adding more acetone when the consistency was like mud. The powder was then transferred to a 100 ml beaker and placed on top of a hot plate (Cole-Parmer StableTemp), to dry the acetone for an hour at $155\text{ }^{\circ}\text{C}$.

The powder was calcined in an alumina crucible in the furnace at $800\text{ }^{\circ}\text{C}$ for one hour, with a $5\text{ }^{\circ}\text{C}/\text{minute}$ heating and cooling rate. Lastly, the powder was broken down in the mortar for 15 minutes before packing and labelling it.

A ceramic pellet was made using a 10 mm die (Specac 10mm DIE) and pressed 15 seconds with one ton in a hydraulic press (Specac Manual Hydraulic Press). Next, the pellet was sintered in a furnace (Nabertherm 30-3000 $^{\circ}\text{C}$) for 2 hours at $1100\text{ }^{\circ}\text{C}$. For piezoelectric measurements, the pellet was polished until a mirror-like surface was acquired using sandpaper. Lastly, for density determination, a caliper (Toolzone Vernier Calliper New GM-000899) was employed to measure both the thickness and the diameter of the pellet and weigh it to calculate the density.

10.2. Particle Size Reduction

As the KNN will be used as a nanofiller in the polymeric nanofibers, they need to be reduced in size, below 100 nm hence the term “nanofiller”. This is done to avoid

changing the morphology of the nanofibers, to have a uniform dispersion in the electrospinning solution and also to benefit from other properties that the KNN possesses: conductivity, thermal stability and mechanical properties that can be useful for the polymeric matrix [96].

The particle size was reduced via high energy milling using the calcined ceramic powder, employing a planetary mill (Fritsch Pulverisette 5) in a Teflon vial with acetone and twenty zirconia balls with a diameter of 5 mm. The cycles were divided into millings of 15 minutes and resting time of 15 minutes, to avoid the accumulation of segregated powder, as well as the internal pressure due to the acetone, until 2 hours of total milling were completed.

In total, seven full cycles were completed from 2 to 14 hours, extracting around 0.2 grams from an initial 2-gram sample after each cycle, to analyze the particle size and morphology with Scanning Electron Microscopy (FEI Inspect F) and measuring the band gap with Ultraviolet-Visible Spectroscopy (Perkin Elmer Lambda35 UV-vis spectrometer). The powder was dried on a hot plate using the same process as the solid-state reaction stated in the previous section.

10.3. Polyacrylonitrile Nanofibers Synthesis

To prepare the polyacrylonitrile nanofibers, a 10 wt% solution was prepared using polyacrylonitrile (PAN, Mw 150,000 Sigma-Aldrich), dissolved in N,N-Dimethylformamide (DMF, ≥99.5% HPLC grade, Fisher Scientific). After adding the PAN to the DMF, the solution was stirred for 24 hours at room temperature. A pristine solution of only PAN was used as a control group.

In order to prepare the composite materials, more batches of 10 wt% PAN solution were used, adding KNN nanoparticles in different weight percentages based on the PAN content (10, 20, 30, and 40 wt%). The ceramic powder was added to the solution before PAN, to avoid any agglomeration of the powder before the polymer was completely dissolved in DMF, stirring for 24 hours at room temperature.

10.4. Electrospinning Technique and Stabilization

After the stirring was completed, the solution was transferred to a 12 ml syringe with a 3 cm blunt needle for the electrospinning process. A pump (World

Precision Instruments) was used for a fixed 0.5 ml/hour flow, using a voltage between 15 and 17.5 kV with a direct current (DC) negative voltage source (SPELLMAN SL10) for the nanofibers production. These were collected on a flat metallic plate (20 x 30 cm), covered in an aluminum sheet. The current was connected to the end of the blunt needle and to the middle top of the metallic plate to avoid any short circuit. All the solutions were electrospun for 6 hours, using a total of 3 ml per solution.

The nanofibers mat was cut into squares of approximately 5 x 5 cm with a scalpel and stored in petri dishes. Next, a flat alumina crucible was used to support the nanofibers mat for the stabilization process, which was performed in an oven (Thermo SCIENTIFIC HERATHERMOven) for two hours at 250 °C. The stabilization process is done on the nanofibers to form the PAN cyclization due to its chemical structure, and to make the fibers conductive, so that they are able to perform the catalysis tests.

10.5. Nanofibers Polarization Via Corona Poling

A corona discharge setup was used to pole and activate the piezoelectric activity in the ceramic nanoparticles and the polymeric nanofibers, both the control powder and pristine PAN samples, as well as the four composites. An array of six needles soldered to a stripboard was used as the corona electrode, to create a dome of ionized air that would serve as the ions for aligning the dipoles in the piezoelectric materials, leaving a 1 cm gap between the sample and the needles, with an electric field of 1.5 kV/mm. The samples were grounded to a metallic plate, and the polarization direction was normal to the surface of the sample.

Dependent on the humidity and temperature in the lab, the corona setup was located inside a fume hood as a safety measure, due to the equipment requiring a high voltage with DC between 11 and 14 kV for a constant 0.03 mA current. The samples were left at room temperature for 30 minutes under the corona discharge and rested for 15 minutes with the high voltage source (GLASSMAN HIGH VOLTAGE Series FR) turned off for the ozone to flow out of the setup before manipulating the samples.¹⁰

9.6. Catalysis Tests

A rhodamine B (RhB) solution was prepared with a concentration of 10 ppm. To avoid any degradation due to light, the volumetric flask was covered in aluminum foil and placed in a cupboard. Three catalysis tests were done on the control groups (KNN powder and pristine PAN fibers) and the composite materials: piezocatalysis, photocatalysis and piezo-photocatalysis. 15 mg of catalyst were submerged in 10 ml of the RhB solution for 30 minutes before the test began. An aliquot of 0.5 ml was extracted from a glass vessel (Adams & Chittenden Scientific Glass) every 30 minutes using a micropipette, until 3 hours of catalysis were completed. The dye was also tested by itself, to analyze its behavior and changes in the concentration that could happen due to the evaporation of water.

For the piezocatalysis tests, the vessel was covered in aluminum foil and placed in an ultrasonic bath (Fisher Scientific FB15050 Ultrasonic Bath). The aluminum cover was moved aside for taking the aliquots and placed back again for the test to continue. Each aliquot was placed in a 3 ml sample vessel, left in a cardboard box to avoid degradation by light.

The photocatalysis tests required a top-down light (Newport Oriel ABB Solar Simulator and Newport Thermo Oriel 69907 Power Supply) that worked as a solar simulator, with an intensity of 250 Watts. The vessel was covered with a quartz lid for the light to penetrate, which was also removed for every aliquot. To keep the process as standardized as possible, the height of the ultrasonic bath was measured, and a small platform was adjusted to this height for the piezo-photocatalysis tests. The same storage system was employed.

Lastly, the ultrasonic bath was placed under the central section of the lamp for the piezo-photocatalysis tests, and a 100 ml beaker was used as a barrier so the vessel would not move with the vibrations. The quartz lid was left on top of the vessel in the same fashion as the photocatalysis tests and the sample vessels for aliquots storage.

After all the samples were collected, a polymethyl methacrylate (PMMA) vessel with a small slit for 1.5 ml samples were employed for measuring the concentration via UV-Vis spectroscopy (Perkin Elmer Lambda35 UV-Vis

Spectrometer), from 340 to 900 nm. The samples taken from the KNN powder control group needed to be centrifuged (Eppendorf Mini Spin Plus Centrifuge) due to the particle size below 100 nm and to avoid any noise in the measurements that could come from the powder. Once all the samples were measured, the data was processed to generate the corresponding plots.

10.7. Characterizations

For potassium sodium niobate powder, a crystallographic study was performed with X-Ray Diffraction (X'Pert Pro, $\text{CuK}\alpha$ 1.541874 Å) to confirm the presence of a pure phase after the calcination and after each milling cycle, as well as after sintering a pellet for piezoelectric testing. X-ray diffraction was also used for the pristine fibers and the composite materials, to analyze the contribution of both materials to the X-Ray pattern. The range set in the Diffractometer was from 5 to 70° (2 θ , with a 0.016 second step. To analyze the presence of the phases involved in the XRD, Rietveld refinement was done with the FullProf software [97]. To determine the lowest calcination temperature, the powder without calcination was analyzed with Thermogravimetric Analysis (Thorn Scientific STA1500), with an air atmosphere from room temperature to 1100 °C.

The powder, the pristine fibers, and the composites were observed with Scanning Electron Microscopy (FEI Inspect F), to analyze their morphology and measure the particle and fiber sizes, as well as the semi-quantitative atomic percentage of the elements present in the samples with an Energy Dispersive X-Ray Spectroscopy detector (EDS). The fibers and composites were also analyzed the stabilization temperature with Thermogravimetric Analysis and Differential Thermal Analysis (Thorn Scientific STA1500).

With the use of Ultraviolet-Visible Spectroscopy (Perkin Elmer Lambda950 UV-Vis Spectrometer), the band gap was determined for the KNN powders, measuring between 200 and 900 nm with an integrating sphere, due to the quantity of the powder available. UV-Vis was also used to measure the concentration of Rhodamine B once the dye degradation was executed for several days. Using Fourier Transform Infrared Spectroscopy (FT-IR Bruker Tensor 27 Spectrometer),

the vibrational modules were measured for the powder, the pristine fibers, and the composites, in a range between 4500 and 500 cm^{-1} . Raman spectroscopy (RENISHAW inVia Raman Microscope) was also employed for the vibrational modules, helpful with the graphitic content in the nanofibers and the niobium-oxygen octahedras in the KNN structure. In Figure 11, the summary of the methodology is presented in a flow diagram. 10 Rhodamine was

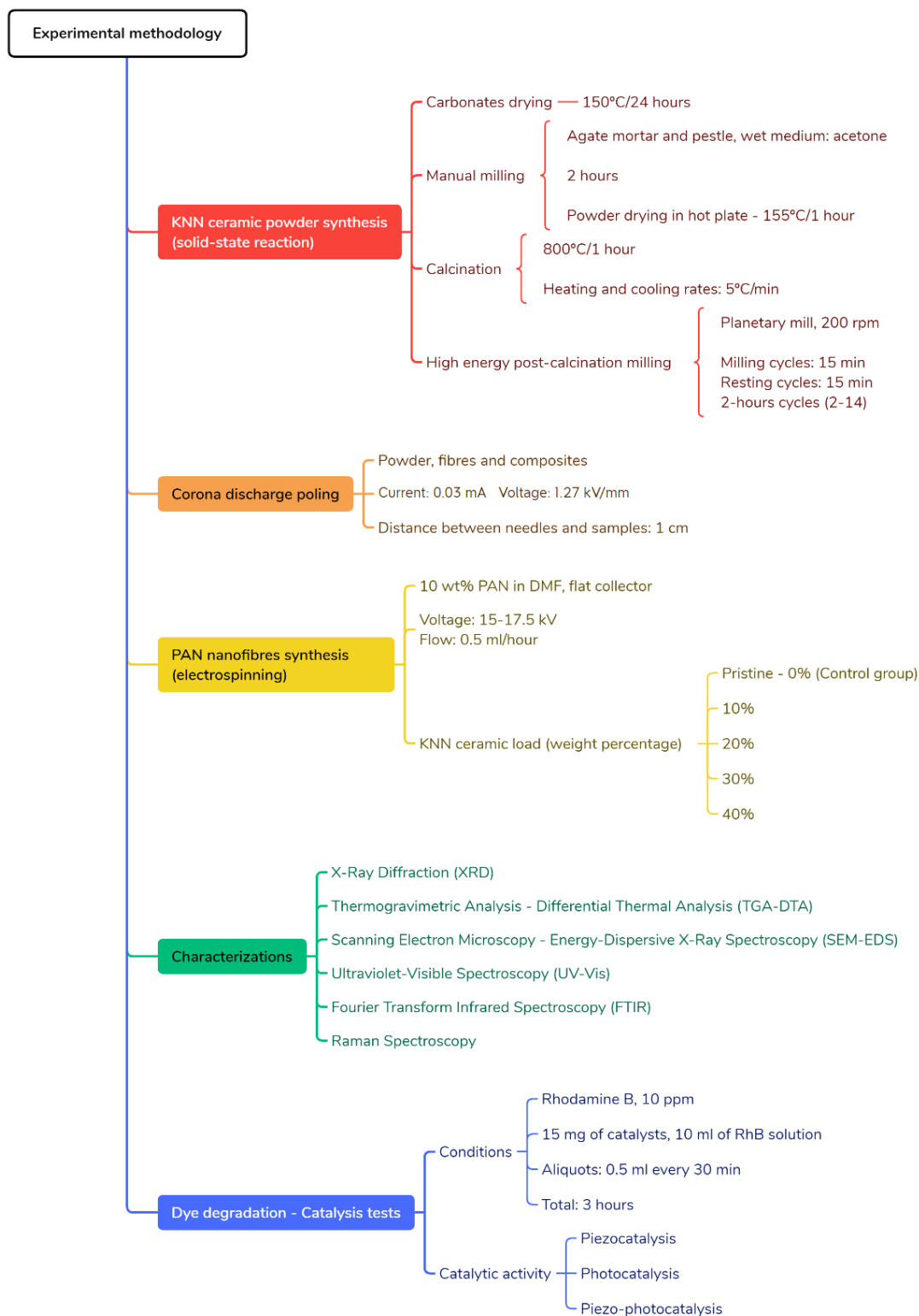


Figure 11. Experimental methodology summarized in a flow diagram.

XI. Results and Discussion

This chapter will be divided into four sections: the results corresponding to the ceramic material (potassium sodium niobate), to the polymeric material and the composites (polyacrylonitrile), the catalysis tests and, lastly, a summary of the results.

11.1. Potassium Sodium Niobate (KNN)

11.1.1. XRD & TGA-DTA

The first approach to confirm a correct solid-state synthesis in ceramic materials is a crystallographic study, done with X-Ray Diffraction (XRD). The potassium sodium niobate (KNN) composition for this project is $K_{0.48}Na_{0.52}NbO_3$, which has shown an increase in the piezoelectric coefficient due to the morphotropic phase boundary (MPB) of various crystallographic structures, as mentioned in previous chapters. The closest KNN composition reported is $K_{0.50}Na_{0.50}NbO_3$ (PDF 00-061-0315), which was used with a tetragonal (P4mm) and an orthorhombic (Amm2) structures to understand which crystalline structure was present with the 48:52 KNN composition [98].

In the first synthesis attempts, a secondary phase appeared at the same time as the 50:50 KNN composition, as shown in Figure 12. This secondary phase was identified as potassium niobate ($K_2Nb_4O_{11}$), with a tetragonal tungsten-bronze structure (TTB), which is commonly observed in solid-state reaction for KNN. The KNN perovskite has two alkaline elements in the A-site, sodium and potassium. Sodium tends to evaporate with higher temperatures during the calcination process, creating a secondary phase rich in potassium ($K_2Nb_4O_{11}$). This phase has photocatalytic properties and is used as a catalyst, when synthesized by a sol-gel route [99].

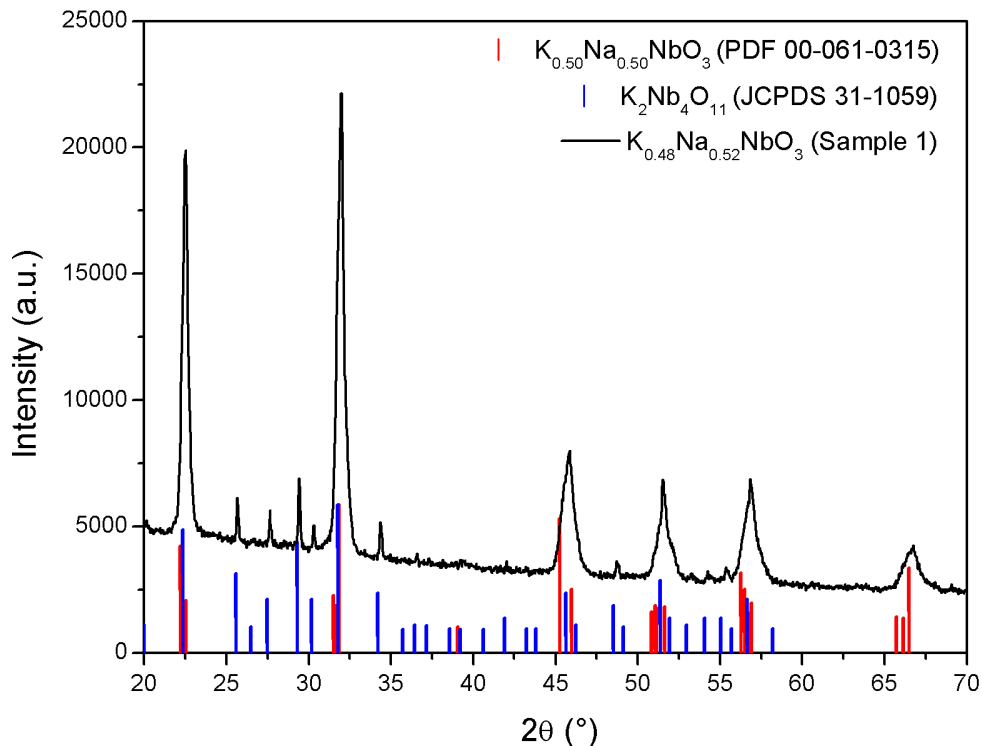


Figure 12. XRD pattern for KNN ($K_{0.48}Na_{0.52}NbO_3$) powder calcined at 900 °C for 1 hour with the tetragonal 50:50 composition and the secondary phase $K_2Nb_4O_{11}$.

The possible factors that could help this secondary phase to grow include: 1) acetone not being fully evaporated after the manual milling; 2) not enough energy administered to the milling process; 3) not enough milling time; 4) incorrect program in the furnace for the calcination process; and 5) the furnace not reaching the temperature set for the calcination; and 6) water molecules stored in the reagents, due to the hygroscopic nature of the carbonates, causing a lower weight added compared to the theoretical values.

Each factor was addressed individually: 1) the powder was dried in a hot plate after the milling process, before the calcination, to avoid any humidity within the powder; 2) and 3) were discarded; 4) and 5) were monitored during the whole calcination process, confirming that the calcination temperature was actually reached and that it followed the sequence programmed in the beginning. Lastly, two new bottles of sodium and potassium niobate arrived while doing the KNN synthesis, and after using these, a pure XRD pattern of $K_{0.48}Na_{0.52}NbO_3$ powder was acquired (Figure 13). The 48:52 composition has a slight shift to the right compared to the

50:50 composition, as the A-site has a 2% atomic difference for this project, and the position is expected to shift, but not the shape of the peaks.

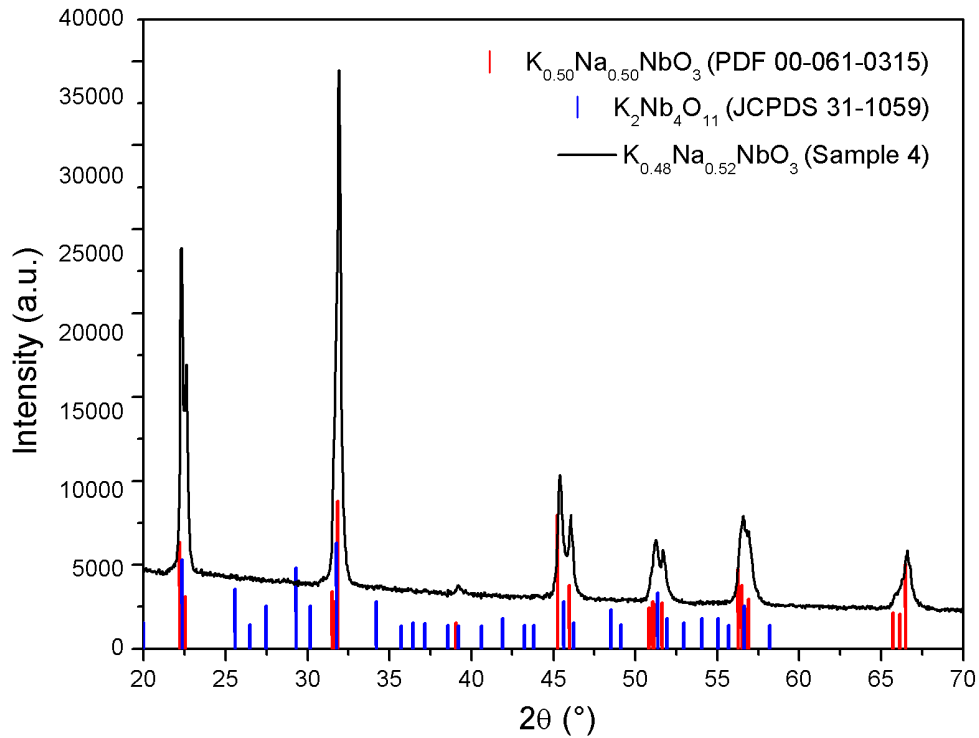


Figure 13. XRD pattern showing a pure phase acquired for 48:52 KNN.

Previously, one of the possible affecting factors mentioned was related to the calcination temperature. Depending on the stoichiometric ratio between the A- and B-sites in the perovskite structure, the calcination temperature can be as low as 675 °C, as tested by Acker *et al.* [100]. As the composition for this project is different to that used in the study mentioned above, the powder before calcination was analyzed with a Thermogravimetric Analysis equipment (TGA-DTA), to check the minimum temperature at which the KNN is completely formed.

In Figure 14, two major transitions happen in the DTA section, which represents the behavior in the thermal changes in the materials, of the test (black line). First, the evaporation of the remaining acetone is shown with exothermic waves below 220 °C, with an approximate 8% in weight loss. The next weight loss occurs around 440 °C, which could indicate the evaporation of carbon in the form of carbon dioxide, and after 700 °C the ceramic powder remains stable, without any weight

loss below 82%. Finally, the crystallization temperature occurs at 740 °C, corresponding to the plateau in the TGA, and confirmed with a small peak in the DTA. For the calcination temperature study, temperatures below and above 740 °C were set for the new batches of KNN powder, all samples left for one hour in the furnace (700 °C, 750 °C, 800 °C, 850 °C and 900 °C).

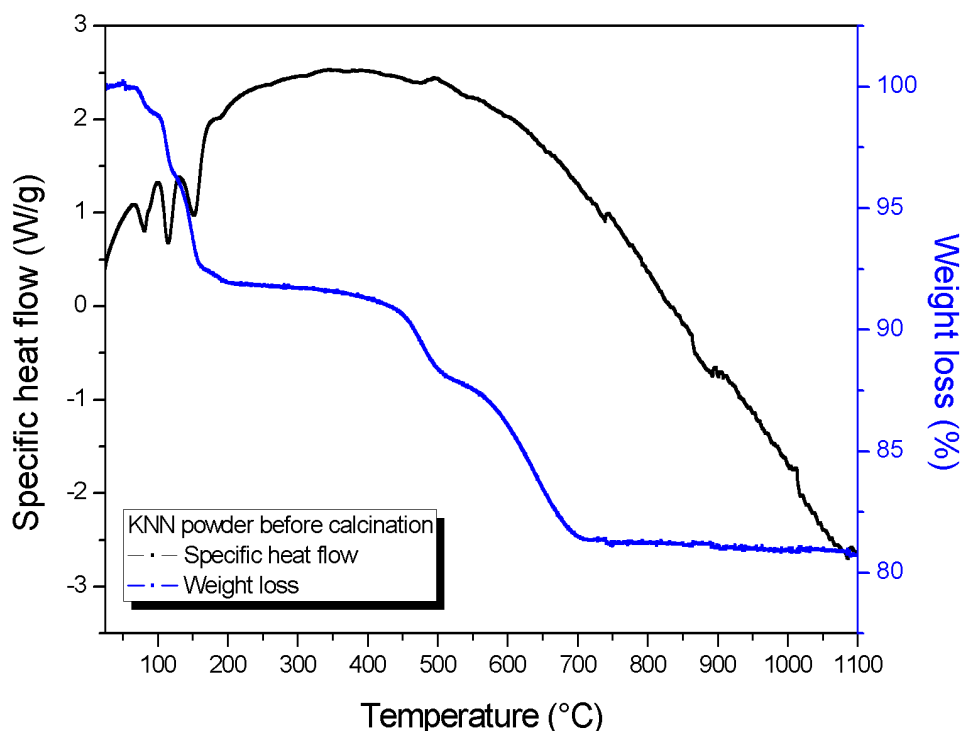


Figure 14. TGA-DTA analysis of 48:52 KNN powder before calcination.

Five XRD patterns were obtained for the calcination temperatures stated above. Figure 15 includes the XRD patterns for those five samples and the indexed data for the $K_2Nb_4O_{11}$ secondary phase and the 50:50 KNN composition. Using the 740 °C mark from the TGA-DTA, the sample calcined at 750 °C should appear without any secondary phase, but at this temperature the $K_2Nb_4O_{11}$ phase is present, and the peaks are not sharp enough nor with the same shape, as seen in Figure 13. The lowest temperature at which no visible secondary phases form in the KNN and sharp peaks are present in the pattern, at least with a 48:52 composition and following a solid-state route for its synthesis, is 800 °C.

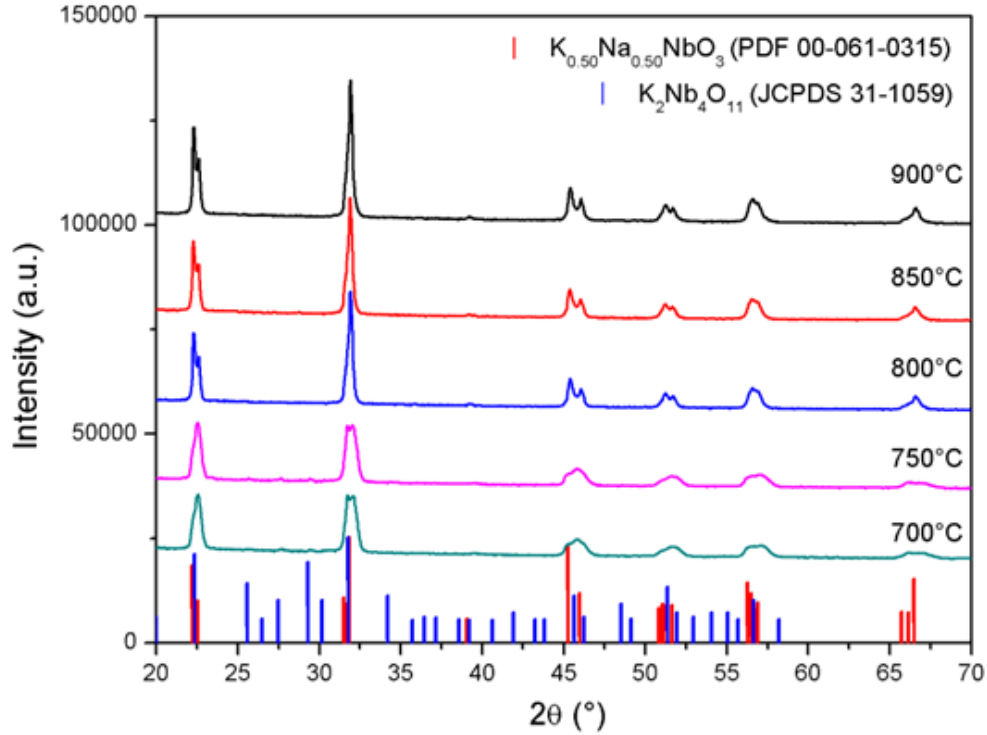


Figure 15. XRD patterns for the different calcination temperatures of $K_{0.48}Nb_{0.52}NbO_3$, including a 50:50 composition and secondary phase.

Once the pure phase at a lower temperature was acquired, a pellet was pressed and sintered at 1100 °C for two hours to calculate the density of this ceramic. Using the diameter, height and weight of the pellet, the density of 48:52 KNN under the solid-state reaction conditions was 3.45 g/cm³. Other values reported for KNN pressed in a pellet with the same sintering conditions to be 4.28 g/cm³, as reported by Jenko *et al.* [101].

The next step was to reduce the particle size below 100 nm from an initial 287.25 ± 127.16 nm (this result is included in the section 11.1.3. SEM-EDS), for it to be used as part of the composite material in the electrospinning process. Before any milling was done, the Scherrer equation [102] was used to calculate the crystallite size from the XRD peaks (Figure 13):

$$D = \frac{K\lambda}{\beta \cos \theta} \quad (3)$$

Where:

D = Crystallite size (nm)

K = Scherrer constant (0.89)

λ = Wavelength from XRD equipment (1.5418740 Å)

β = Full Width at Half Maximum (FWHM) of the peak

θ = Bragg angle (°)

In Table 3, the data obtained from the XRD pattern are shown in dependence on the peak position, with the average at the bottom. The crystallite size for a 48:52 KNN composition, calcined at 900 °C was 22.32 ± 6.69 nm.

Table 3. Crystallite size calculation using the Scherrer equation from the XRD pattern shown in Figure 13.

Peak position (° 2 θ)	Crystallite size (nm)
22.33	26.72
22.54	38.51
31.92	23.94
39.19	17.58
45.38	20.77
46.14	20.13
51.23	16.83
51.67	22.48
56.62	14.95
56.91	18.27
65.87	20.37
66.27	32.09
66.58	17.49
Average crystallite size	22.32 ± 6.69 nm

Subsequently, a planetary mill was employed to reduce the particle size, using acetone as the liquid medium. The powder was milled for 14 hours in total, taking small samples every 2 hours. The first three samples were analyzed in XRD to ensure that the secondary phase did not grow with the high energy from the milling process. In Figure 16, the milled samples are compared to the sample without any milling post-calcination, where the lack of a secondary phase indicates that the powder is stable enough to endure high energy from agitation.

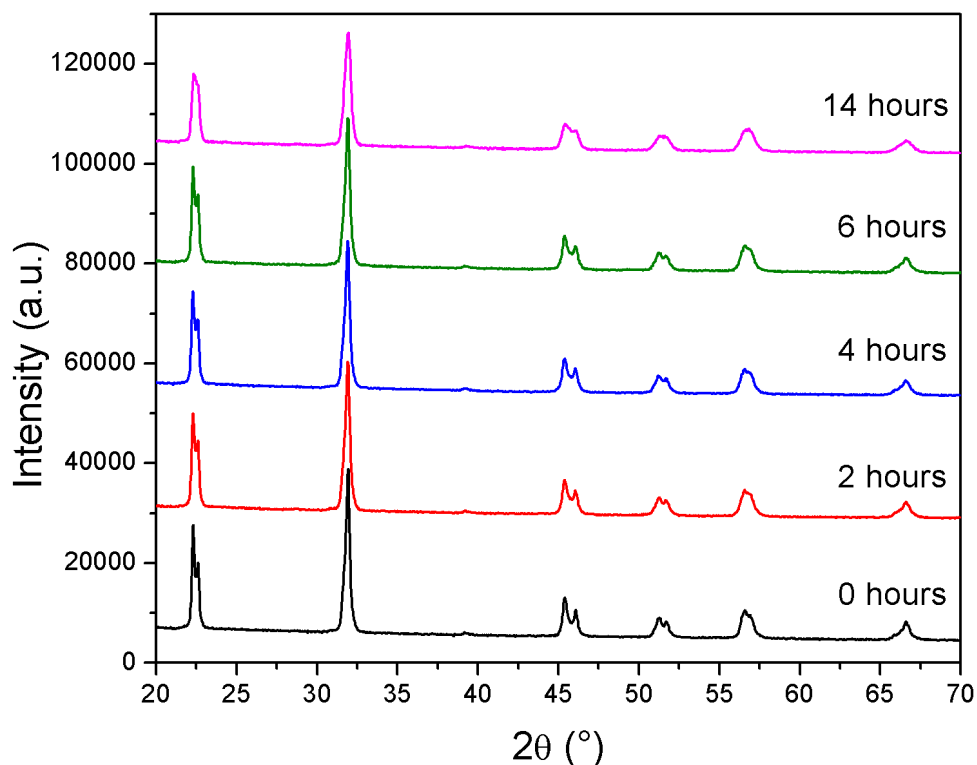


Figure 16. XRD patterns for KNN powder milled post-calcination, from 0 to 14 hours.

11.1.2. Rietveld Refinement

As mentioned before, the potassium sodium niobate can present multiple crystalline structures, depending on the temperature at which the ceramic works. At room temperature, the most likely crystalline structure is orthorhombic, and the following structure is orthorhombic. To confirm the presence of one or another, or both phases, a Rietveld refinement with a Pseudo-Voigt peak shape was conducted on the XRD pattern shown in Figure 13 using FullProf software for it [97]. In Table 4, the final results of the refinement are presented, for the lattice parameters, the angles and the cell volume, comparing both the tetragonal and the orthorhombic phase from the 48:52 to the 50:50 composition. After the refinement was completed, the residual factors (R) [103] resulted in $R_{wp} = 7.99$ and $R_{exp} = 5.21$, with a $\chi^2 = 2.3568$.

Table 4. Rietveld refinement parameters obtained for tetragonal and orthorhombic phases for $K_{0.48}Na_{0.52}NbO_3$, compared to $K_{0.50}Na_{0.50}NbO_3$: lattice parameters (Å), angles (°) and cell volume (Å³) [98].

Composition	Phase	a (Å)	b (Å)	c (Å)	α (°)	β (°)	γ (°)	Volume (Å ³)
48:52	Tetragonal (P4mm)	3.9926(7)	3.9926(7)	3.9496(6)	90.00	90.00	90.00	62.959(19)
	Orthorhombic (Amm2)	3.9454(2)	5.6470(4)	5.6755(3)	90.00	90.00	90.00	126.448(14)
50:50	Tetragonal (P4mm)	3.9551	3.9551	4.0210	90.00	90.00	90.00	63.539
	Orthorhombic (Amm2)	3.9551	5.6573	5.6717	90.00	90.00	90.00	126.330

In Figure 17, the XRD pattern with the Rietveld refinement is presented, where a total of 57.63(1.97) % of tetragonal structure and 42.37(1.23) % of orthorhombic phase are present in the 48:52 KNN composition synthesized via solid-state reaction, confirming that the MPB is present in this composition, as suggested by Saito *et al.* [9]. Also, in Figure 17 the structures drawn with the Vesta program [35] are presented.

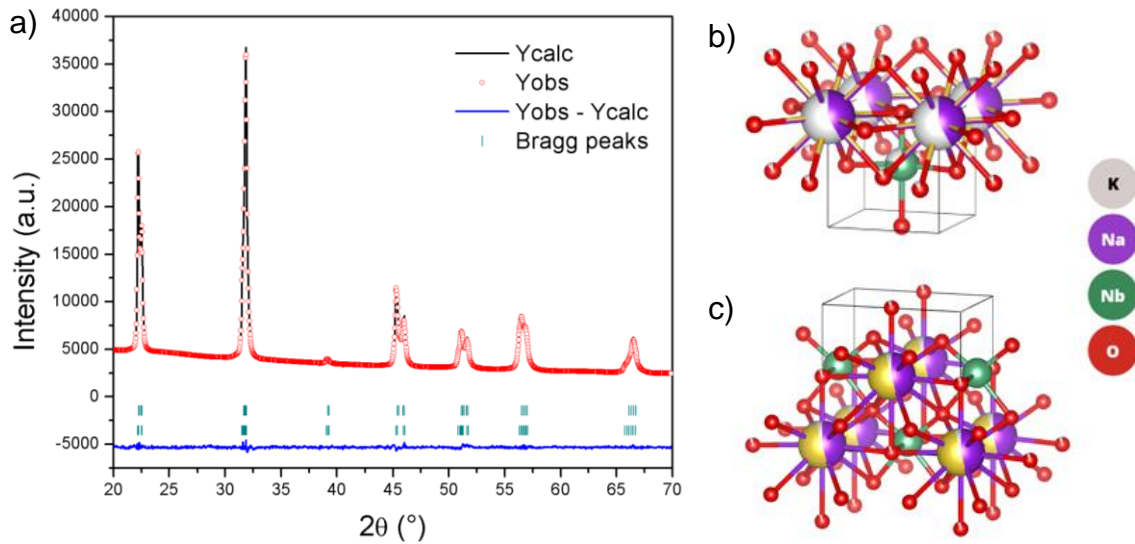


Figure 17. a) XRD pattern done with Rietveld refinement, along the b) tetragonal and c) orthorhombic structures of $K_{0.48}Na_{0.52}NbO_3$ obtained from the refinement.

After this analysis, a refinement was calculated individually for both the orthorhombic and the tetragonal phases, to observe closely the contribution of each to the KNN powder measured with XRD. The R factors and χ^2 are reported in Table

5, where the orthorhombic phase has a better fit to the XRD pattern compared to the tetragonal.

Table 5. Rietveld refinement parameters comparing the orthorhombic and tetragonal phases, individually and altogether, reporting R_{wp} , R_{exp} , χ^2 and the phases percentage (%).

Phases	R_{wp}	R_{exp}	χ^2	Phases percentage (%)
Tetragonal	33.7	5.31	40.2	100
Orthorhombic	10.1	5.19	3.78	100
Tetragonal - Orthorhombic	7.99	5.21	2.36	Tetragonal: 57.63 Orthorhombic: 42.37

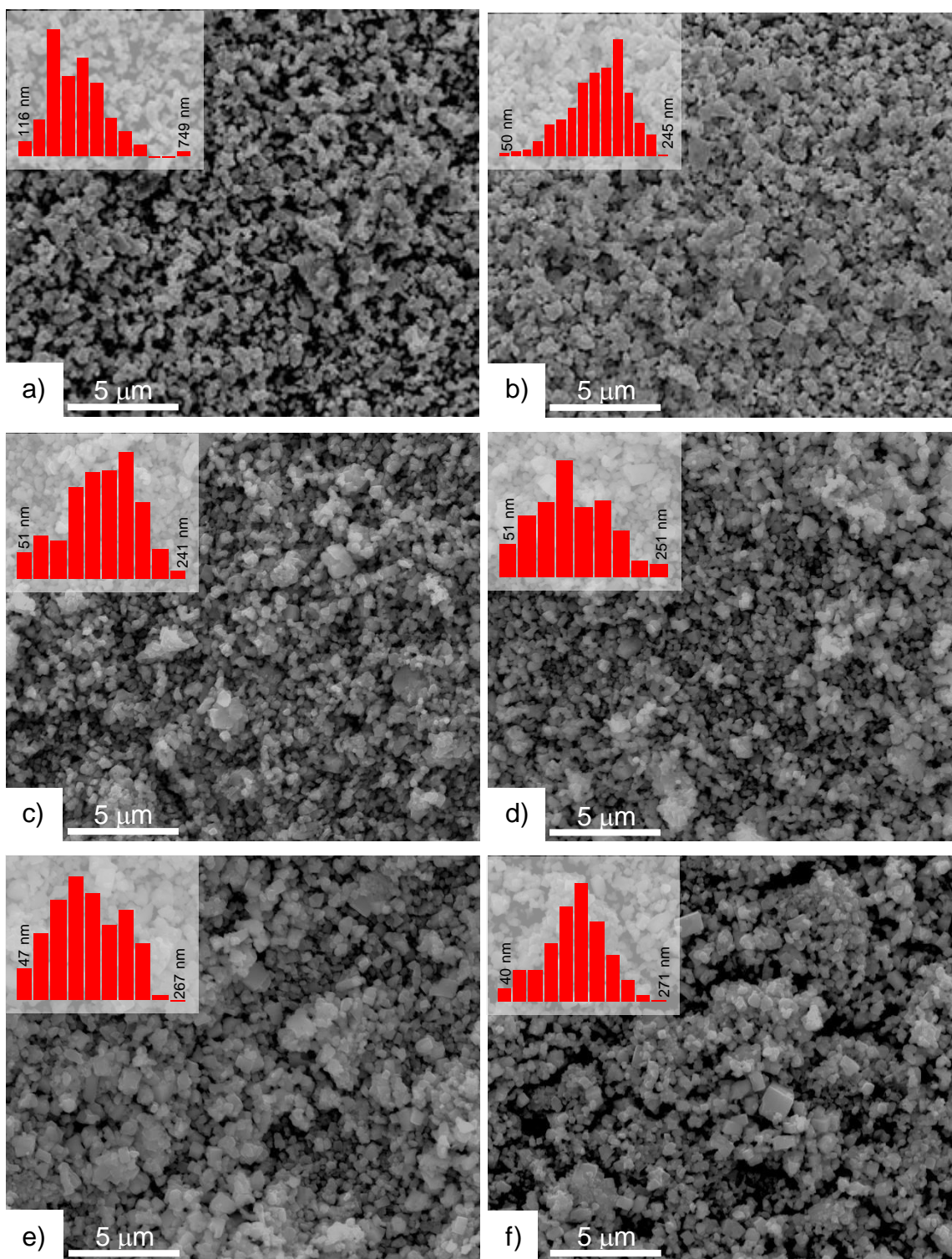
11.1.3. SEM-EDS

After the high energy milling was completed, the samples were analyzed via Scanning Electron Microscopy with Energy Dispersive X-Ray Spectroscopy (SEM-EDS), to obtain images and atomic percentage of the elements present in the samples, to confirm that the 48:52 composition was maintained before and after the milling was done. For this analysis, the control group was the sample without any post calcination milling, as shown in the group of images in Figure 18.

In this set of SEM images, KNN powder with different stages of post-calcination milling can be seen, including in each image the particle size distribution with the minimum and maximum values. Regarding the particles shape, the majority of the powder had a rectangular or squared form, that is softened at the edges with the milling time increase. The agglomeration that was visible in Figure 18a and 18b is reduced with time as well, allowing the smaller particles to be separated from the bigger ones. Before doing the size analysis, the atomic percentage for the 48:52 composition was calculated in theory following the stoichiometric ratio, and later compared to the results from EDS. This comparison can be seen in Table 6.

The distribution followed a normal behavior with 0, 2, 10, 12 and 14 hours with negative skewness in 0 and 12 hours and positive skewness in 2 and 14 hours, having a scattered trend between 4 and 6 hours of milling. In Figure 18 f), the 10-hour sample presented the most normal behavior compared to the other samples.

The lowest particle size range in any of the samples corresponded to the 12-hour sample, with a minimum of 25 nm and a maximum of 213 nm.



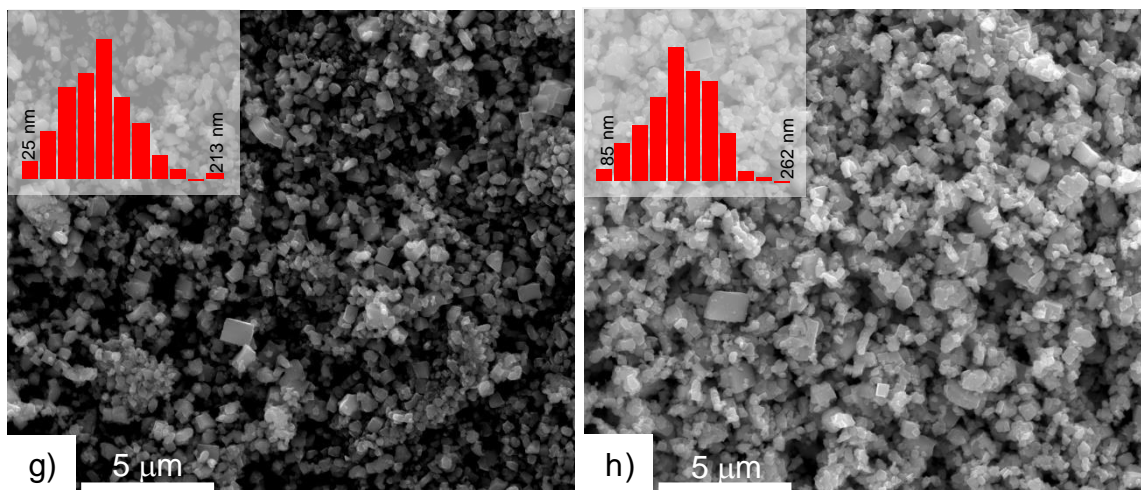


Figure 18. SEM images from 48:52 KNN powder at different post-calcination milling times, including histograms from the particle size distribution: a) 0 hours, b) 2 hours, c) 4 hours, d) 6 hours, e) 8 hours, f) 10 hours, g) 12 hours and h) 14 hours.

Using the ImageJ software [104], the particle size was measured for each sample, from 0 to 14 hours of post-calcination milling (8 samples in total), with 300 individual measurements to obtain the average particle size listed in Table 6. The Table shows that all samples have a high standard deviation, due to a large distribution in size of the particles within the powder; this could be due to particles that were stuck to the walls of the vessel for the majority of the milling time, and came loose after taking samples out for their measurement in SEM. It can be concluded that the post-calcination milling is working, but it would require more time, even up to 24 hours or more to reach the average particle size mark of 100 nm required for the project, as a smaller particle size is better for the morphology of the nanofibers.

Table 6. Average particle size with standard deviation (nm) from the KNN powder after the particle size reduction process with high energy milling.

Sample	Particle size (nm)
0 hours	287.25 ± 127.16
2 hours	288.41 ± 130.41
4 hours	268.99 ± 114.74
6 hours	243.01 ± 108.11
8 hours	245.67 ± 117.08
10 hours	236.16 ± 112.66
12 hours	228.03 ± 116.26
14 hours	189.95 ± 104.78

While working with the EDS, general and punctual measurements were conducted on each sample, showing that with a higher post-calcination milling time, the atomic percentages are closer to the theoretical value for a 48:52 composition, shown in Table 7. The oxygen and niobium percentages are the two elements that change the most in the samples, stabilizing around 4 and 6 hours. This could be due to the sampling before the measurements, or probably oxygen vacancies due to the amount of energy supplied during the milling process.

Table 7. EDS results for the KNN samples before and after post-calcination milling in atomic percentage (at%), including theoretical values for $K_{0.48}Na_{0.52}NbO_3$.

Element	Theoretical (at%)	0H (at%)	2H (at%)	4H (at%)	6H (at%)
K	9.60	13.25	10.12	9.22	9.68
Na	10.40	10.99	12.23	12.72	11.54
Nb	20	28.94	24.17	17.48	17.28
O	60	45.91	53.48	60.58	61.50

11.1.4. UV-Vis

The nature of the project and the application for the composites require knowledge of the optical band gap of the material. For this, the powder was measured in reflectance mode in a UV-Vis spectrometer with an integrating sphere, using the Tauc method to obtain the energy value:

$$(\alpha \cdot h\nu)^{1/\gamma} = B(h\nu - E_g) \quad (4)$$

Where:

α = Absorption coefficient

h = Planck constant (1240 eV*nm)

ν = Photon's frequency

γ = Nature of electron transition (1/2 – direct transition, 2 – indirect transition band gap)

B = Constant

E_g = Band gap energy (eV)

For this case, as the obtained data was in reflectance mode, the Kubelka-Munk method was employed to calculate the optical band gap, as it uses a function for the reflectance instead of the absorption coefficient:

$$F(R) = \frac{K}{S} = \frac{(1 - R)^2}{2R} \quad (5)$$

Where:

$F(R)$ = Reflectance function

K = Absorption coefficient calculated from reflectance

S = Scattering coefficient

R = Reflectance

With this, the reflectance function is substituted where the absorption coefficient is in the Tauc equation [105]:

$$(F(R) \cdot h\nu)^{1/\gamma} = B(h\nu - E_g) \quad (6)$$

The powder measured with UV-Vis was before the post calcination milling process (0 hours), and two more samples milled in the planetary mill (6 and 12 hours). In Figure 19, the three samples are presented with the value of the optical band gap. It has been tested that with the reduction of the particle size, it is possible to reduce the optical band gap as well, as done by Kujur *et al.* [44]. As shown in the plots, and what was initially stated in the hypothesis of this work, the band gap should reduce with the particle size reduction. The optical band gap does indeed reduce, but it is only a small variation between 12 hours of post calcination milling compared to the sample that did not undergo any milling process. For a 50:50 composition, the

optical band gap has been reported to be around 2.9 eV for an average grain size of 270 nm, using the solid-state reaction for its synthesis [92].

This slight change could originate from the possibility that the smaller particles were not extracted from the sample, but rather the whole range of particle size was sandwiched between two slides of microscope glass. Correlating the band gap with the average particle size for each sample, the following data are compared: for 0 hours, the average particle size is 287.25 ± 127.16 nm with a 3.94 eV in the optical band gap; for 6 hours, 243.01 ± 108.11 nm have a 3.93 eV band gap; and lastly, 12 hours of post calcination milling present a 3.92 eV band gap for an average particle size of 228.03 ± 116.26 nm. At least two more samples would be sufficient to create a trending line and try to understand if there is a direct or indirect correlation between the particle size in the KNN ceramic powder and its optical band gap.

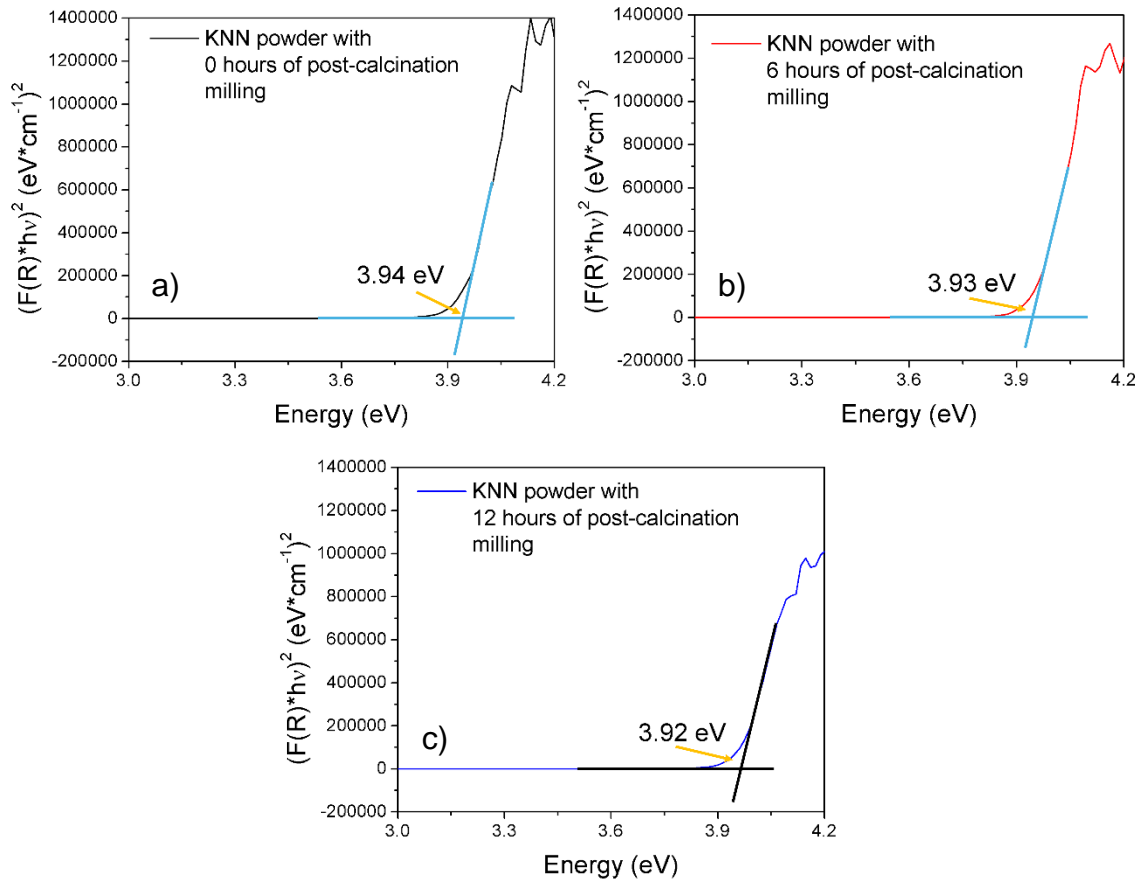


Figure 19. Tauc plots for obtaining the optical band gap of KNN powder with post-calcination milling process: a) 0 hours, b) 6 hours and c) 12 hours.

11.1.5. FT-IR

FT-IR spectra were obtained for KNN powders before and after it was calcined. Figure 20a, presents two peaks in 2339 and 2359 cm^{-1} , that correspond to the interaction between carbon and oxygen, usually related to the carbon dioxide molecule (CO_2) [106]. This could be due to two reasons: firstly, the appearance of CO_2 in the spectrum as background noise when running a background check in the FT-IR equipment; secondly, is the carbon-oxygen double bond ($\text{C}=\text{O}$), with an asymmetric stretch, coming from the sodium and potassium carbonates used as reagents for the KNN synthesis.

This peak does not appear in Figure 20b, which shows the IR spectrum for the powder after being calcined at 900 $^{\circ}\text{C}$ for an hour. The only visible peak is a depression occurring at 615 cm^{-1} , which correlates with a niobium oxide bond ($\text{Nb}-\text{O}$). In 2010, De Oliveira Cantão *et al.* studied niobium oxide (Nb_2O_5) with infrared spectroscopy, where one of the peaks appeared in 621 cm^{-1} , among others, that refers to the interaction $\text{Nb}-\text{O}$ [107].

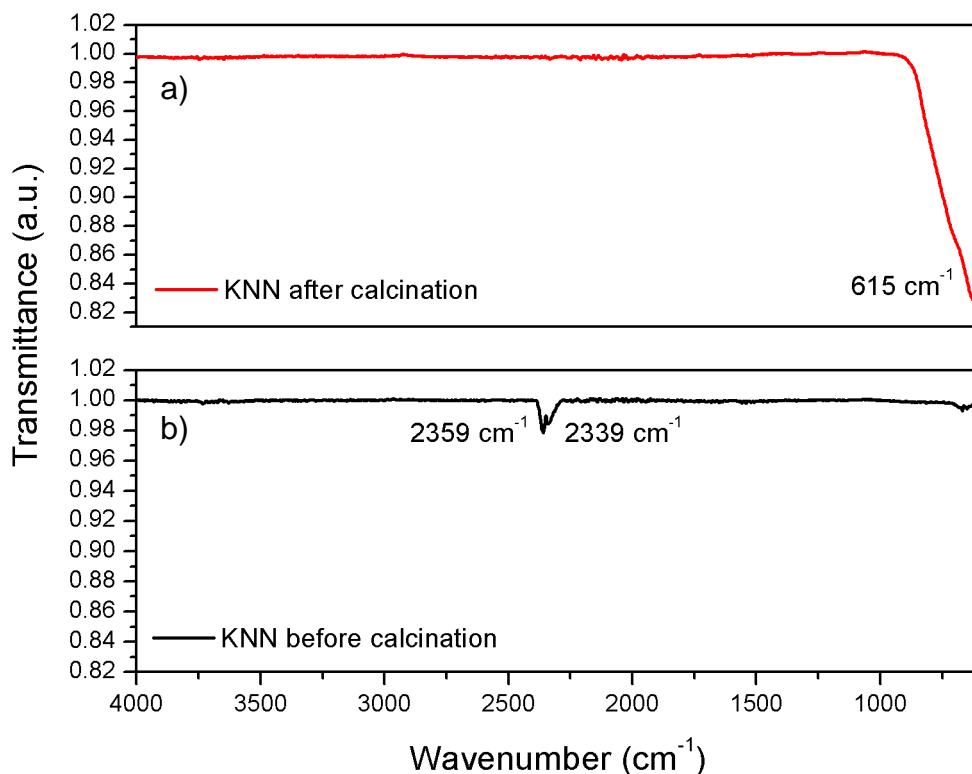


Figure 20. Infrared spectra of the KNN powder a) before and b) after calcination.

11.1.6. Raman Spectroscopy

Continuing with vibrational modes, the KNN powder was analyzed with Raman spectroscopy, using a 442 nm laser, obtaining Figure 21. In this spectrum, 5 distinctive peaks can be observed, which are compared to other experimental data from a 50:50 KNN composition. This comparison is made to observe a shift, as was the case in XRD, where the peaks shifted towards the right with a 48:52 composition, as shown in Table 8 [55]. For the KNN, the orthorhombic phase has 27 optical phonon vibrations, as mentioned by Saha *et al.* [108], in a theoretical and experimental study done for a 50:50 composition in 2024. According to Saha *et al.*, the group that represents the optical phonon vibrations for the KNN are within the C_{2v}^{14} point group in the zone-center (Γ -point):

$$\text{Raman} \equiv \Gamma \equiv 9A_1 \oplus 9B_1 \oplus 7B_2 \oplus 2A_2 \quad (7)$$

Kakimoto *et al.*, in 2005, studied $K_{0.50}Na_{0.50}NbO_3$ with a 514.5 nm laser and obtaining the same point group as Saha *et al.*, but they only present half of the vibrations:

$$\text{Raman} \equiv 4A_1 \oplus 4B_1 \oplus 3B_2 \oplus A_2 \quad (8)$$

where the A_2 vibration is not infrared active [109]. This difference is due to the number of atoms that were studied by Saha *et al.*, where they used 10 atoms in their theoretical study, whereas they confirm that its equivalence in 5 atoms represents what was studied by Kakimoto *et al.*

Table 8. Vibrational modes analyzed in Raman for KNN powder with a 48:52 composition, compared to a 50:50 KNN composition.

Vibrational mode	$K_{0.48}Na_{0.52}NbO_3$ (cm^{-1})	$K_{0.50}Na_{0.50}NbO_3$ (cm^{-1}) [55]
$F_{2u}(\nu_6)$ [A_1]	142.00	200.00
$F_{2g}(\nu_5)$ [A_1]	248.78	250.00
$E_g(\nu_2)$ [B_1]	578.77	550.00
$A_{1g}(\nu_1)$ [A_1]	616.86	617.00
$A_{1g}(\nu_1) + F_{2g}(\nu_5)$ [A_1]	856.72	858.00

All the shifts, excluding E_g , have a left shift compared to the 50:50 KNN. This vibrational mode (E_g) is related to the NbO_6 octahedron, in an asymmetrical vibration sense. This shift to the right could explain why FT-IR also shifts to a smaller wavenumber in the Nb-O interactions. The rest of the peaks, as mentioned, shift towards the left. From the vibrational modes, A_{1g} , E_g and F_{2u} correspond to stretching modes, whereas F_{2g} and ($A_{1g} + F_{2g}$) are bending modes, as mentioned in Dwivedi *et al.* study in 2018 [110]. Using the Fityk software [111] a deconvolution was done to the peaks with a Voigt function, obtaining Figure 21 a). With this deconvolution, it can be seen that there is a peak that was not considered in Table 8, around 201 cm^{-1} that would correspond to F_{2u} , and the first peak shifts to the left and is at 135 instead of 142 cm^{-1} , which then should belong to an A_1 vibrational mode, mentioned by Saha *et al.* to be around 131 cm^{-1} in their theoretical study [109]. The other peaks do not shift compared to the deconvolution. In Figure 21 b), the Raman intensity spectra obtained by Saha *et al.* is shown with the peaks with highest intensities, as well as their position. Comparing the spectrum obtained for this work and the theoretical and experimental study done by Saha *et al.*, it can be concluded that the pattern corresponds to an orthorhombic phase in the KNN.

Even though it was mentioned above that there are 27 phonon vibrations, when analyzing Saha's study [109] only 14 of these have Raman intensities above 0.01, and five of these 14 present intensities above 0.10, which coincide with those

reported in Table 8. At least five peaks are visible before doing the deconvolution, where an additional peak can be perceived at a lower value, between the first two peaks in Table 8 (142.00 and 248.78 cm^{-1}). This extra peak is located around 200 cm^{-1} , which corresponds to a B_1 vibration, and the 142 cm^{-1} peak is an A_1 vibration or the movement of alkali elements (sodium and potassium) within the niobium-oxygen octahedra.

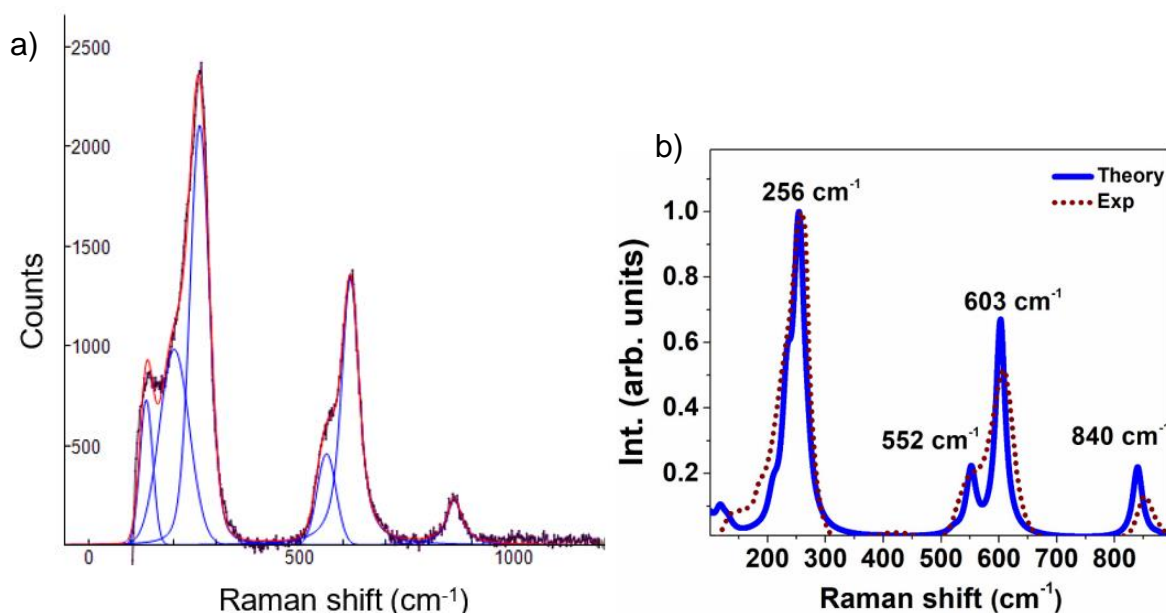


Figure 21. a) Raman spectrum with deconvolution for 48:52 KNN composition; and b) Theoretical and experimental studies done by Saha *et al.* with the composition K_{0.50}Na_{0.50}NbO₃ [109].

11.2. Polyacrylonitrile (PAN) Fibers and KNN + PAN Composites

11.2.1. XRD & TGA-DTA

PAN shows only two crystalline diffracted planes in its fibers, located in $\sim 17^\circ$ and $\sim 29^\circ$ (2θ), as seen in Figure 22a. The peak that should appear sharper at about 17° (2θ) is for a (100) hexagonal plane, as studied by Mathur *et al.* in 1991 [112]; the next peak, at about 29° (2θ), softens as the stabilization time increases, as done by Lee *et al.* by stabilizing PAN with different times (Figure 22 b) [113].

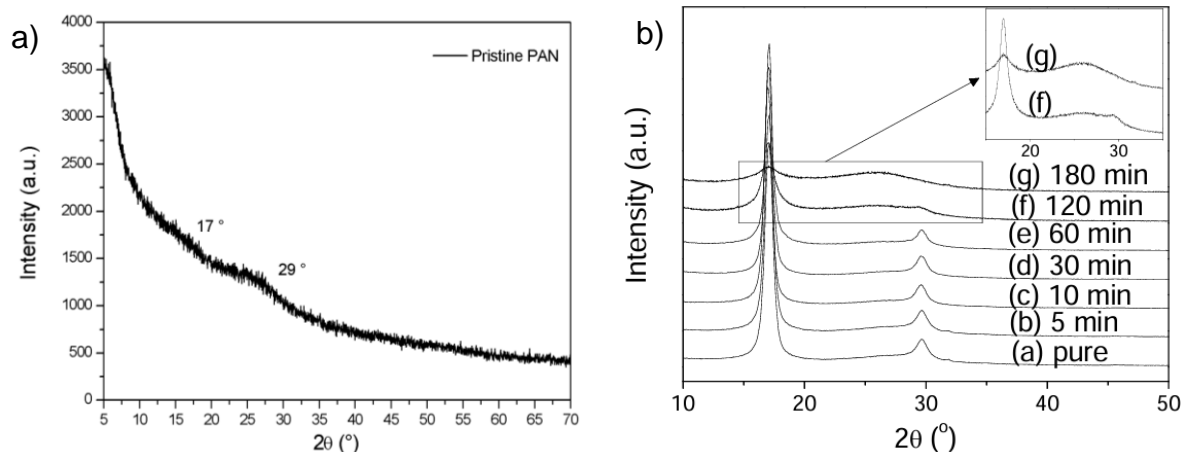


Figure 22. a) XRD pattern for a 10 wt% pristine PAN sample stabilized at 250 °C for 2 hours; b) XRD pattern obtained for pristine PAN samples stabilized at 250 °C for different times, extracted from the study conducted by Lee *et al.* [113].

Figure 23 includes four different KNN-PAN composites with different KNN wt% load. Comparing this plots in Figure 22a, the peak in 17° (2 θ), which corresponds to PAN, loses intensity from the 10 wt% until it flattens with the 40 wt% KNN composite. The shoulder between the two highest peaks from the crystalline phase from the KNN, at about 22° and 32° (2 θ), corresponds to PAN at about 29° (2 θ), which also decreases in intensity with a higher amount of KNN. A possible explanation for this correlates with the TGA results, which will be discussed further down in this section.

The peaks for 30 and 40 wt% KNN composites lose the sharpness, quite visible in the peaks between 45° and 60° (2 θ), as well as the peak at 22° (2 θ). This could be due to the agglomeration that was also visible with the SEM images and how the particles are covered by the PAN nanofibers. This, as previously mentioned, could be a reduction in the crystallization of the PAN due to a higher ceramic load within the fibers. In 2021, Doumeng *et al.* studied the effect of four different fillers in polyetheretherketone composites, a polymer used for its stiffness. One of the fillers was alumina, where it showed that by increasing the particle load into the composite from 2.5 to 5 wt%, a reduction in crystallinity from 43.1 to 33.1% was observed in the XRD patterns. They conclude that due to a higher particle load, there is less opportunity for the particles to move in the polymer and create a stress in the

nucleation process, hence the reduction in the crystallinity [114]. The agglomeration of KNN particles could also present this behavior, as the particles have a lower surface area where the PAN can interact with and a lower crystallization activity as a consequence.

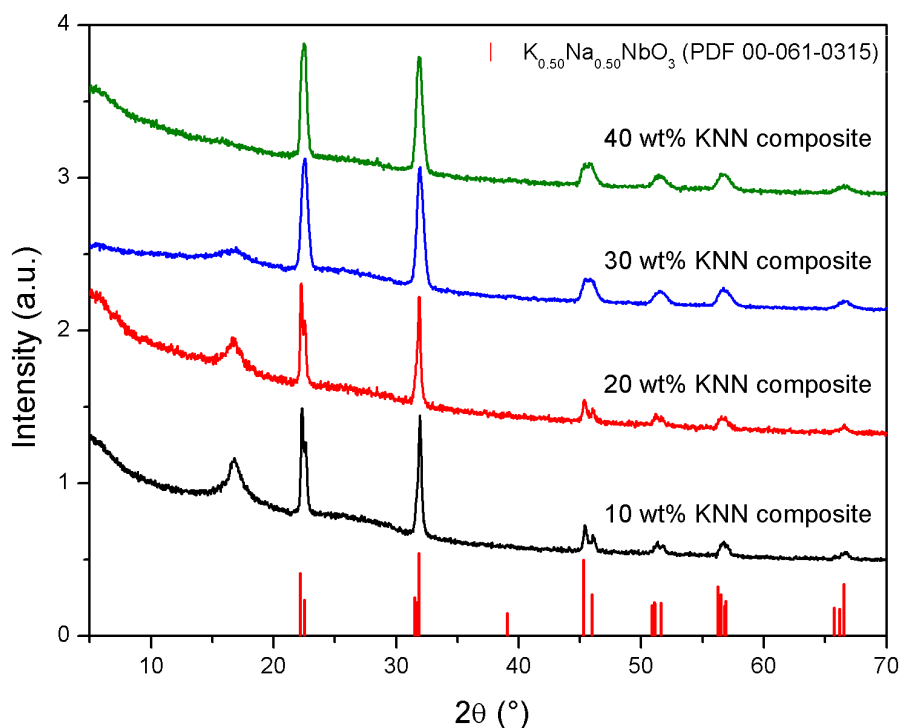


Figure 23. XRD patterns for the composite samples, including the tetragonal structure in the 50:50 KNN composition (PDF 00-061-0315).

Due to the organic nature of the fibers, measuring them in TGA-DTA resulted in a helpful way of understanding how the ceramic nanoparticles were impacting the weight changes in correlation with the temperature at which the fibers were subjected. In Figure 24, all the curves are shown between 50 and 900 °C in a nitrogen (N₂) atmosphere, with fibers that did not receive any thermal treatment, also known as stabilization. All the samples, up until 250 °C, are quite stable to the temperature increase, but after this point the first weight drop is noticeable, even though it does not happen at the same temperature for all the samples.

This first weight loss is due to the cyclization in the PAN structure, where the nitrogen in the nitrile groups ($\text{-C}\equiv\text{N}$) bonds with the carbon in the nitrile group next

to it, leading to the formation of an aromatic ring, as explained by Jin *et al.* [102]. After this change in the chemical structure, the fibers continue to lose weight until 900 °C; this temperature was chosen as the upper limit because it would not have any effect on the ceramic particles. The remaining weight was mostly the KNN added to the solution and the fibers ashes. The composite that has the least weight loss is 20 wt% with a remanent weight of 39%, whereas the 30 wt% has the highest weight loss with a remanent weight of 18%. This behavior could be due to the fibers collection site, as the mid-section of the mat after being collected in the aluminum foil has the highest concentration of fibers and particles as well.

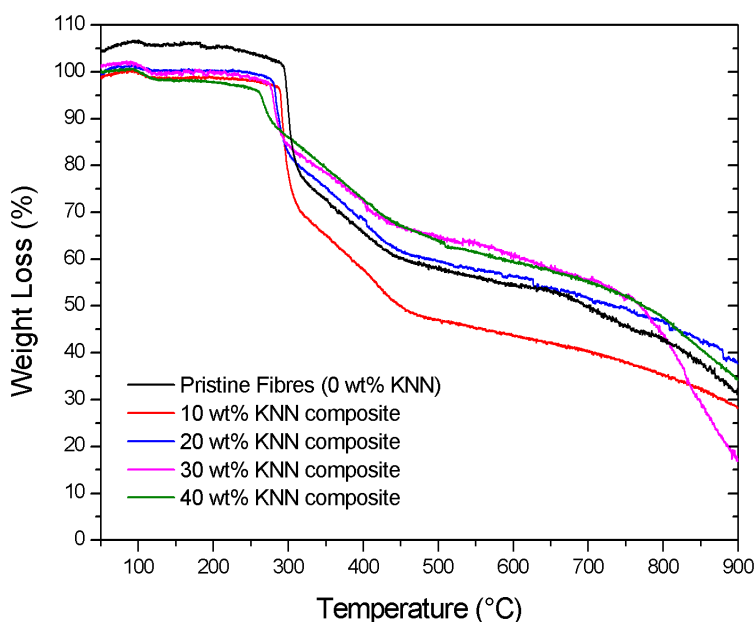


Figure 23. TGA plot, showing the fibers with and without ceramic nanoparticles.

As a composite, the properties of the material will change due to adding a different compound, and in this case, the ceramic particles had a direct effect on the stabilization temperature mentioned above. In Table 9, the stabilization temperatures are listed for the pristine fibers, as well as the composites, going from 10, 20, 30 to 40 wt% of KNN in the solutions. The weight loss curve for the 40 wt% KNN composite has a less defined drop around 265 °C, compared to the same weight drop around 300 °C for the pristine fibers.

The difference between the stabilization temperature in pristine fibers and the 40 wt% composite is 33.56 °C, as shown in Table 9. The decrease in the stabilization temperature is almost linear, even though the difference between the 20 and 30 wt% KNN composites are quite close to each other. Nevertheless, the decrease in the stabilization temperature is attributed to the presence of ceramic particles, that are known for being resistant to high temperatures, thus helping in the nanofibers stabilization process by needing less energy to cycle the chemical structure with the nitrile groups. An example of this behavior in other polymers was studied by Torres-Giner and Lagaron, in 2010, where they synthesized composite materials from zein electrospun nanofibers, a type of protein found in maize, and different clay nanofillers: kaolinite, montmorillonite, mica and zeolite. The purpose of this study was to analyze the thermal and mechanical properties of the fibers with different ceramic content in the fibers. The glass transition temperature (T_g), also known as stabilization temperature, from the pure fibers was 158.90 °C, and by adding even 1 wt% of any of the ceramic nanofillers in different batches, reduced by 1 °C, and up to 3 °C in the case of the zeolite nanofiller (155.16 °C). In this case, the authors mention that ceramic fillers act as reinforcing plasticizers, helping the polymeric stabilization to occur at a lower temperature [118].

With a higher ceramic load, the stabilization temperature decreases, not allowing the nitrile groups cyclisation in PAN to happen consistently. The temperature registered for the 40 wt% KNN composite was 264 °C, and the temperature used for the stabilization of all the samples was 250 °C; this closeness in the temperatures could explain the loss of sharpness in the peaks in the XRD patterns from Figure 23. A Rietveld refinement would help understanding which proportion of the tetragonal and orthorhombic structures from the KNN is present in the 30 and 40 wt% KNN composites.

Table 9. Relation between the ceramic load in the samples and the shifting in the stabilization temperature (°C), measured with TGA-DTA.

Sample	Stabilization temperature (°C)
Pristine fibers	298.36

10 wt% KNN	291.69
20 wt% KNN	282.94
30 wt% KNN	279.20
40 wt% KNN	264.80

Comparing the TGA-DTA plots from which the information from Table 9 was collected, the exothermic peak for the stabilization temperature in the 40 wt% composite shifts to the left of the pristine PAN sample in Figure 25. Another noticeable difference is that the specific heat flow in the 40 wt% KNN sample is less than that of pristine PAN, also attributed to the presence of a ceramic material as the filling in the composite. The sharp peak in the DTA curves has an exothermic nature related to the cyclization of the nitrile groups in PAN. When the ceramic nanoparticles load increases, the peak loses sharpness, and the overall DTA curve in 40 wt% KNN does not go higher than 40 W/g, that could also correlate to the presence of a ceramic material in the composite, compared to almost 80 W/g at the end of the pristine fibers graph. Also, the content of ashes should be higher in the case of the composites, as the ceramic does not suffer a loss in mass at this temperature.

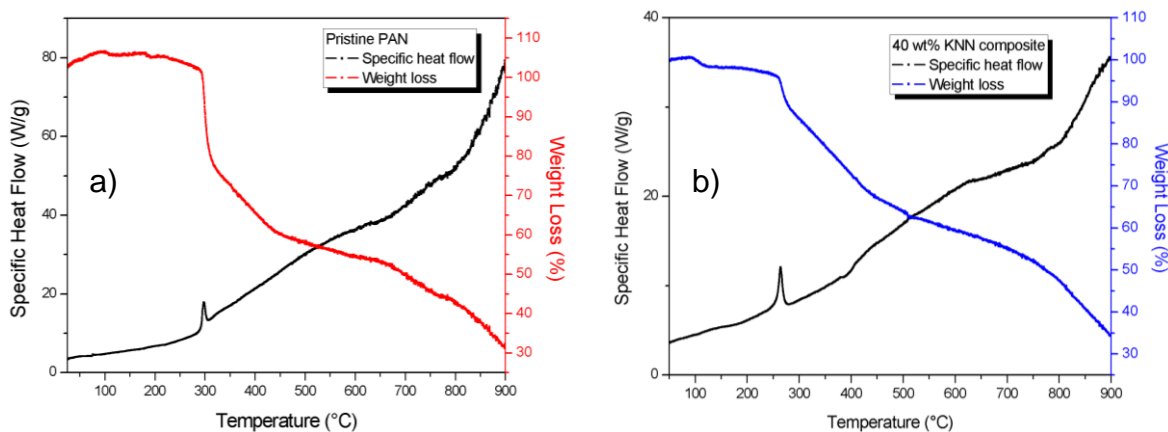


Figure 25. TGA-DTA of a) pristine PAN and b) 40 wt% KNN composite.

11.2.2. SEM

To confirm that the nanoparticles are indeed being distributed in the fibers after the electrospinning process, the samples were analyzed in SEM, to both observe the distribution and calculate the fibers diameter, as this parameter can be

changed with the concentration of the solution, the humidity and electric field administered to the deposition. In Figure 26, images from the different samples are presented, and in Table 10 the diameter size is included per sample.

Due to the use of a flat collector for the electrospun fibers, the array of these is completely random, from the pristine fibers to those with ceramic nanoparticles. Some of the pristine fibers (Figure 26a) bend in sharp angles, while others intertwine between themselves, that could be due to stress from the electrospinning process, or stress derived from the shrinkage after the stabilization [119]. Starting with the 10 wt% composite material, in Figure 26b there are two main characteristics that are present in the fibers: the particles within the fibers and what appears to be a balloon shape. This balloon appears in the fibers when the voltage is too high while electrospinning the solution.

The agglomerations vary in size and shape in the composite samples (Figure 26b, 26c, 26d and 26e), and this could be related to the static nature of the powder. While manipulating the KNN powder for weighing it, for example, it would disperse in the air when in contact with laboratory gloves. Furthermore, the use of the corona discharge for poling the powder would make it disperse in the air. The voltage used for the electrospinning process was between 15 and 17.5 kV, which could have concentrated the powder in the manner observed in Figures 26d and 25e.

Additionally, with the growth of the agglomerations, the nanoparticles tend to fold at the edges in the way a plastic product scorches. This could indicate that, with a bigger agglomerate, the nanoparticles would look to form a micelle as a more stable structure, although this behavior was not observed in any of the samples. Another interesting conduct from the fibers is that the polymeric matrix tried to wrap the particles together (Figures 26d and 26e), some even going to the point of electrospinning a fiber at the ends of the agglomerate, as observed at the bottom of Figure 26d. The distribution of ceramic particles appears to cover the surface almost homogeneously, and the agglomeration could even be beneficial for the catalysis process by having a higher surface area of nanoparticles acting as redox sites.

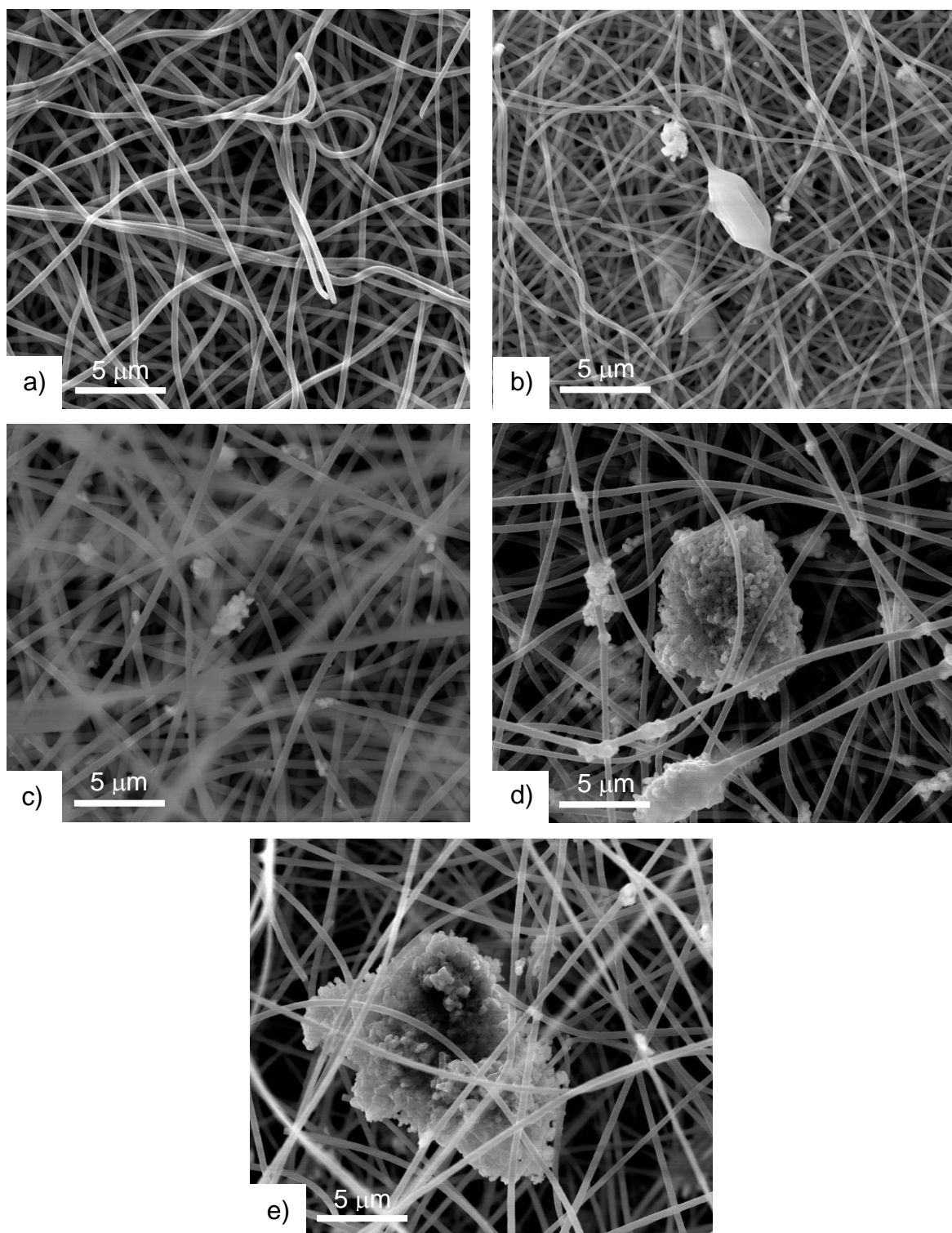


Figure 26. SEM images from pristine fibers and composite samples, stabilized at 250 °C for 2 hours, 10k magnifications. a) Pristine PAN, b) 10 wt% KNN composite, c) 20 wt% KNN composite, d) 30 wt% KNN composite, and e) 40 wt% KNN composite.

Looking at the average diameter of the fibers, the inclusion of ceramic nanoparticles changes the viscosity of the solution, and it even affected the voltage at which the solution was electrospun, starting with 17.5 kV and needing to reduce to 15 kV. This reduction was due to the presence of solution droplets in the aluminum foil, and these droplets indicate that the voltage is too high, so the solution does not have enough time to form a fiber but rather just gets spit out of the syringe. With a lower voltage, the fibers get thicker as seen in Table 10.

Zhang *et al.*, in 2012, created a correlation list between electrospinning conditions and its effect on the fibers diameter. To contradict what was seen in this project, they listed that with a higher voltage, the fibers get thicker, as does increasing the viscosity in the solution. This last point is what could be affecting the electrospinning of the KNN – PAN composite solution, as the voltage apparently did not behave as predicted by Zhang *et al.* [120].

Table 10. Average nanofibers diameter (nm) from pristine PAN and composite materials measured from SEM images, and the voltage at which the solution was electrospun.

Sample	Fibers diameter (nm)	Electrospinning voltage (kV)
Pristine PAN	306.92 ± 68.05	17.5
10 wt% KNN composite	251.58 ± 49.60	17.5
20 wt% KNN composite	455.54 ± 64.09	15
30 wt% KNN composite	396.01 ± 80.86	15
40 wt% KNN composite	344.78 ± 50.21	15

11.2.3. FT-IR

Five distinctive peaks can be attributed to the PAN fibers in the IR spectra [112]. All these peaks are present in the pristine PAN fibers, as well as the composite material.

- C=C-H (aromatic rings): 806 cm⁻¹
- C-O: 1365 cm⁻¹
- C-C: 1451 cm⁻¹
- C=C: 1587 cm⁻¹
- C≡N: 2243 cm⁻¹

For the KNN contribution, the Nb-O bond is present around 615 cm^{-1} , which its intensity increases with a higher ceramic load. This could indicate that the particles are integrating correctly inside the fibers. The PAN peaks also decrease with a higher ceramic load, as can be seen in Figure 27. The 20 wt% and 40 wt% KNN plots have a deeper pronunciation in the Nb-O curve, that could be due to the section where the sample was measured in FT-IR, as this does not happen with the other composite materials. Additionally, the 40 wt% KNN sample has a visible reduction in the nitrile bond ($\text{-C}\equiv\text{N}$), which could correlate to the stabilization temperature reduction discussed above.

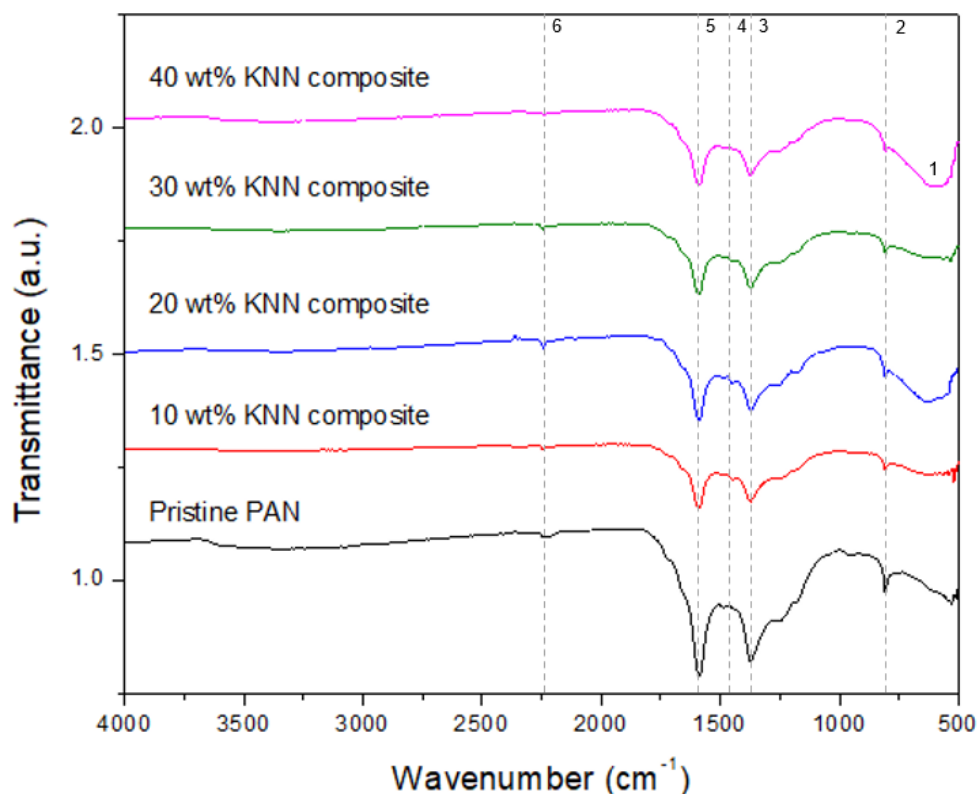


Figure 27. FT-IR spectra of pristine PAN and composite samples, with the following bonds: 1) Nb-O: 615 cm^{-1} ; 2) C=C-H: 806 cm^{-1} ; 3) C-O: 1365 cm^{-1} ; 4) C-C: 1451 cm^{-1} ; 5) C=C: 1587 cm^{-1} ; and 6) $\text{C}\equiv\text{N}$: 2243 cm^{-1} .

11.2.4. Raman Spectroscopy

Measuring the fibers with Raman turned out quite challenging: the fibers would burn where the laser was placed, and even though the parameters of intensity and the lasers were changed, only two samples could be measured and, even after

finishing, they looked melted. Two distinguishable peaks with the shape of “cat ears” are present in both spectra, corresponding to D and G (E_{2g2}) vibrational modes are shown Figure 28. In polymeric materials, these two bands are related to the graphitic degree of the samples. Due to the stabilization process, the fibers indeed possess a level of graphitic layers in them, but with the composite materials these bands appear higher and with a slight shift to the right.

Correlating with the results from TGA-DTA, the reduction in the stabilization temperature by the inclusion of ceramic particles in a polymeric matrix causes a shift and an increase in the graphitic vibrational modes. The peaks that appeared in the KNN powder, discussed in Figure 21, were expected to appear in the composite material, but it could be that the small particles are not large enough to appear in the composite spectrum like they did in the bulk sample. The rise in Figure 28b at the end of the axis was not identified.

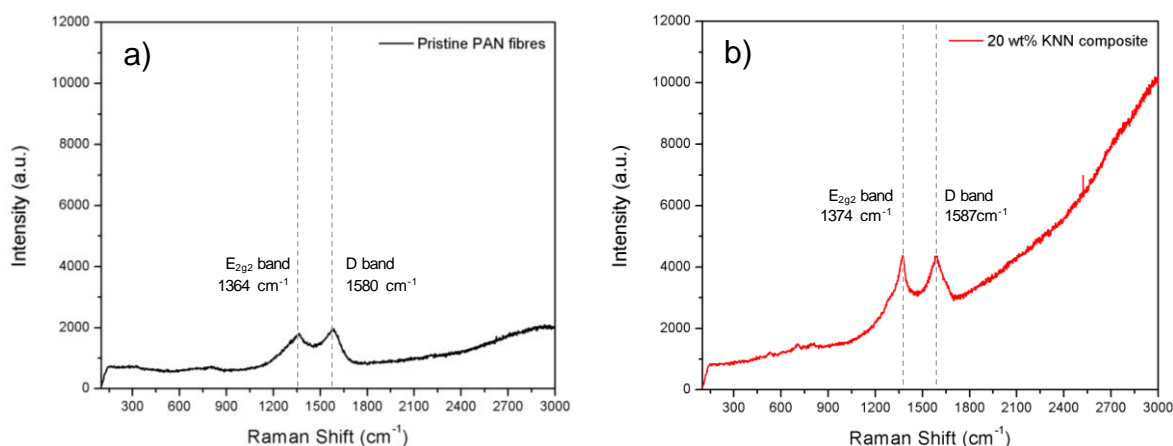


Figure 28. Raman spectra for a) pristine PAN and b) 20 wt% KNN composite, measured with a 442 nm laser.

11.2.5. Corona Poling

After the characterizations were completed for the fibers, the corona discharge setup was used for poling the samples that were used for the catalysis tests, including two control groups: pristine PAN fibers and KNN powder, and four composite samples (10, 20, 30 and 40 wt% KNN). Once the poling was complete, some visible but tiny holes were seen in the surface of the fibers, mostly in the pristine PAN sample, as can be observed in Figure 29.

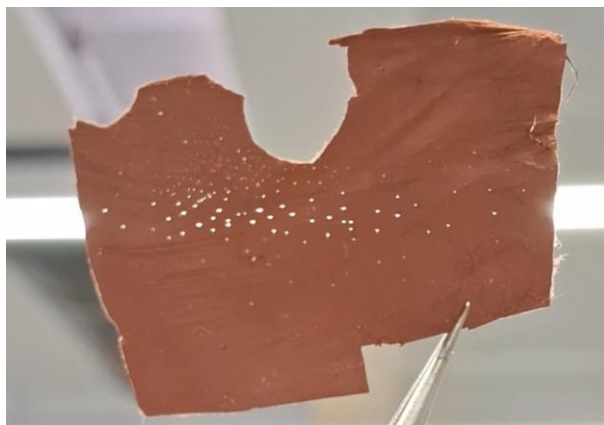
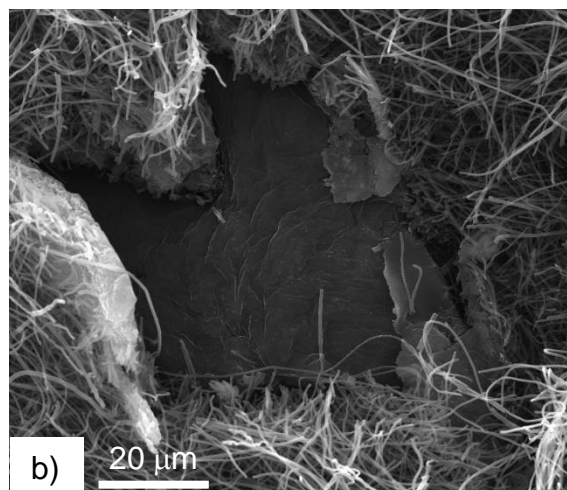
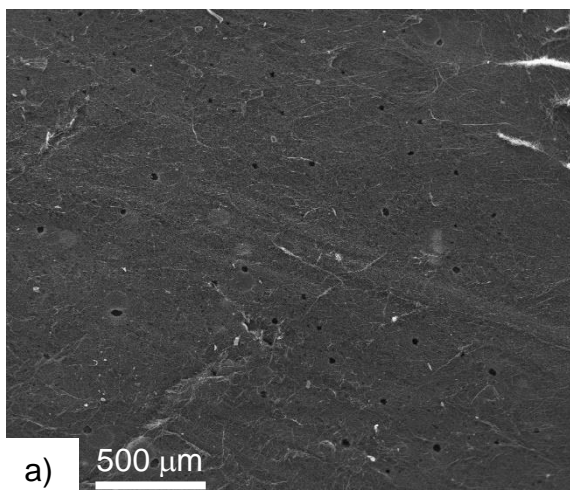


Figure 29. Pristine PAN mat after corona poling. Image conditions: Samsung A14 5G, screenshot from a video.

The samples were analyzed in SEM (Figure 30) to observeview better the holes and how they affected the fibers. From Figure 30a, more holes are visible, covering the surface of pristine fibers, not only on a visible distance with the naked eye, and looking with a higher magnification (Figure 30b), the edges of the holes are melted and the fibers underneath the hole as well. Indicating that corona poling parameters were set too high, and it burned the sample. It is interesting that the corona poling affected the sample in small holes, instead of melting the sample in general. This could be that these holes appeared in places where the volume of fibers was less dense, but also that the discharges from the corona poling looked for the easiest pathway to the sample, which had the most conductive regions in the surface.



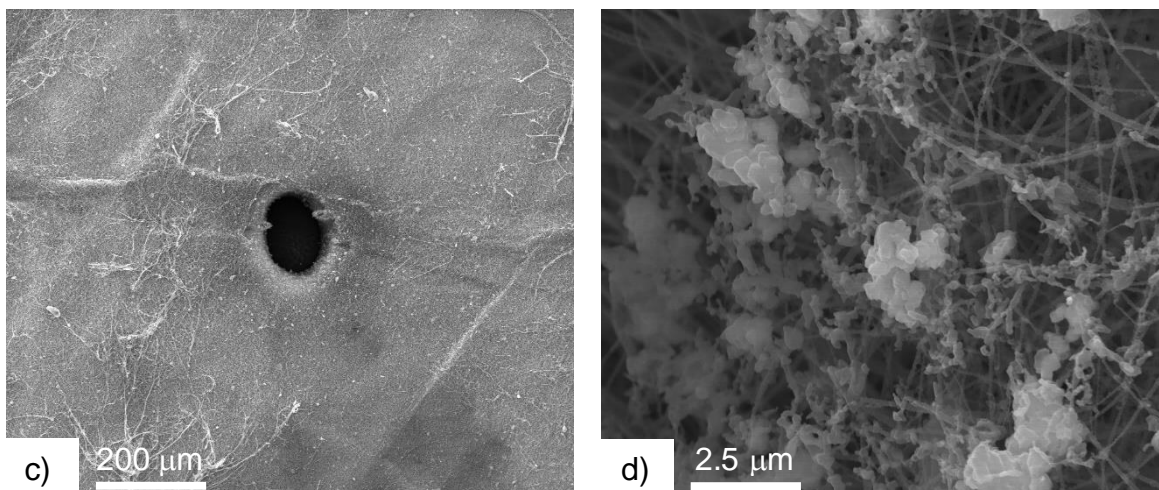


Figure 30. SEM images from poled pristine PAN (a & b) and 30 wt% KNN (c & d) samples.

Figures 30c and 30d correspond to the 30 wt% KNN composite and the holes have a rounder shape, but in Figure 30d it can be observed that the KNN nanoparticles are unveiled from the charred fibers. This could have a direct effect on the degradation capacity, but further tests would be needed to conclude this. Also, it could be that the particles, being so static, help the ionized air from the corona poling to concentrate in specific areas, as the particles do not seem affected by the discharge as the fibers do.

11.3. Catalysis Tests

The control groups for the catalysis tests were the pristine PAN fibers, and the KNN powder, while the Rhodamine B (RhB) was tested by itself in the same manner as the rest of the samples. After the fibers were used for the first set of catalysis tests (piezocatalysis), they were dried on a hot plate to evaporate the water, and were reused for the photocatalysis and, after, the piezo-photocatalysis tests. The KNN powder could not be recovered after each test, due to the particle size and its deposition at the bottom of the vessel, so new powder from the same batch needed to be poled and used.

11.3.1. Piezocatalysis

From the three catalytic tests, the piezocatalysis activity had the most abnormal performance in almost all the cases, and this could have been due to the

water evaporation from the energy of the ultrasonic bath, leading to an increase in the dye concentration. In Figure 31, the list of samples is shown between 0 and 180 min, which is the length of the tests set for this project, and what has been used in several studies [121]. RhB was evaluated by itself, to be able to discern that the samples were degrading the dye, and it was not due to the behavior of the solution in a constant stressed and heated environment.

If we consider the dye as a baseline, there are three candidates that perform better below the dye line (black line in the graph): pristine PAN, KNN powder and 10 wt% KNN composite. Before beginning this project, while doing a literature review, the option that the polyacrylonitrile was a piezoelectric polymer was even considered while looking for background information, but after this catalytic activity test, a review was written by Tao *et al.* at the end of 2023 [122]. In this review, several studies prove that PAN can be used as a piezoelectric material, but the majority focused more on its mechanical properties as a high resistance polymer rather than the piezoelectric properties.

With this latest information, the composite materials should have an enhanced piezoelectric activity, a combination from both the ceramic and the polymeric materials. Counting only with one set of results from this test, the 10 wt% KNN composite could be said to have a piezoelectric activity coming more from the PAN fibers than the KNN particles, as the quantity of KNN is based on the weight percentage of PAN in the solution rather than the solvent.

The rest of the composite materials had a weak performance, mostly the 40 wt% KNN sample. In the 30 and 40 wt% cases, compared to the others, the concentration goes up in the 60-minute mark, and they tend to stay above the concentration in the 30-minute mark, with an absorbance of 21.84% for 30 wt% KNN and 36.69% for 40 wt% KNN samples. These results could correlate to the crystallization of the fibers, as was seen in Figure 23, were less crystalline materials have a decrease in the degradation ability. All the samples have a lower relative concentration at the end of the test (180 min) compared to the dye. More tests would be required to know if the data obtained in the first place is correct, and it could be

that the rest of the samples have a better performance than what is shown in Figure 31.

In the piezocatalysis case, the best performers were the control groups (pristine PAN and KNN powder), and the 10 wt% KNN composite. For the 10 wt% composite, the initial absorbance was 100%, and the absorbance after 180 of catalytic activity was 23.29%, which translates into a 76.71% removal efficiency after 3 hours. The efficiency in the control groups were 69.14% with pristine PAN fibers, and 61.40% with KNN powder.

No visible color changes were observed in any of the cases, even though some of the samples should be almost as clear as water, all remained a bright pink shade, maybe due to lack in catalysis-action time.

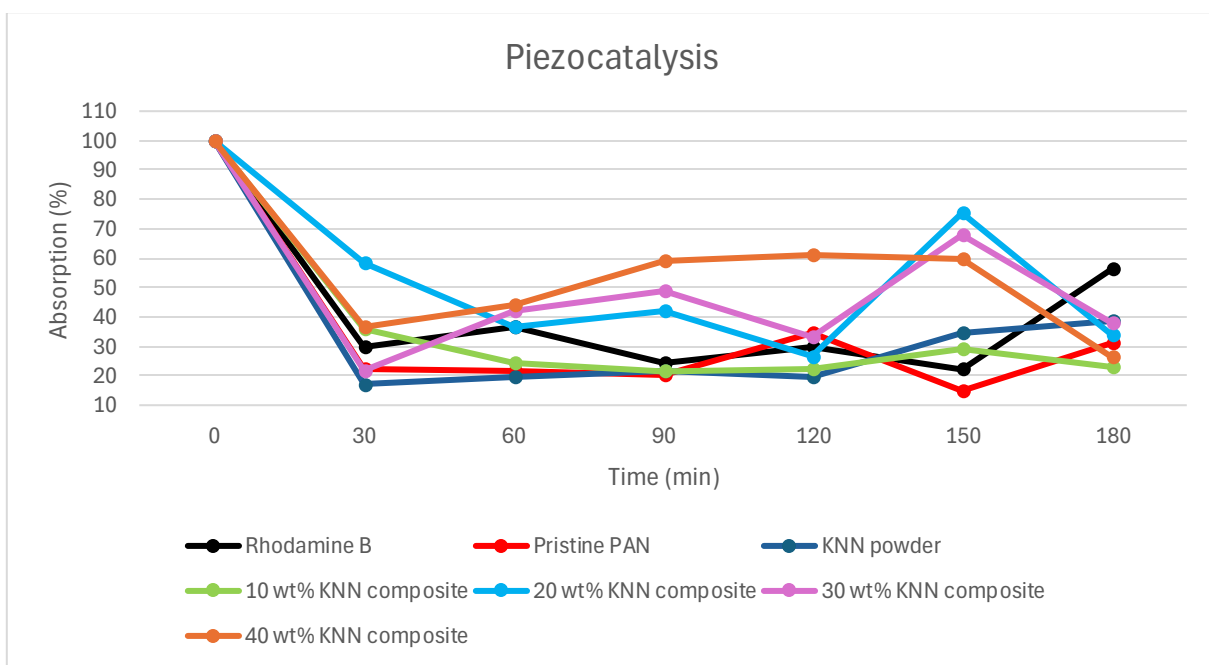


Figure 31. Piezocatalysis samples tested from 0 to 180 min, including the dye itself, the control groups and the composite materials.

11.3.2. Photocatalysis

Continuing with the photocatalytic activity tests, the performance was weaker than in piezocatalysis, but the catalytic behavior seems more stable, like pristine PAN and KNN powder, which are the control groups. A visible difference between the piezo- and the photocatalysis tests is that the dye is more stable under direct

light, as it evaporates less water compared to the ultrasonic bath, which indicates that the samples are degrading the dye more effectively than the heat in the system, as can be seen in Figure 32.

The 90-minute mark shows a change in the path of the composite materials, in some decreasing the absorbance drastically (10 wt% KNN) and in others increasing the absorbance (20, 30 and 40 wt% KNN). This could be due to an increase in the concentration of the dye due to the light shining above the vessel and evaporating the solvent. Nevertheless, the composites increase their dye degradation capacity, as the 20 and 30 wt% have a better performance than 10 wt%, which was the best in the piezocatalysis section. The trend for this catalysis test, and the other ones, was expected to be a linear behavior, due to the increase of the ceramic load. Regarding the control groups, the KNN powder has a better removal capacity compared to the pristine PAN.

Potassium sodium niobate has been previously used as a photocatalyst for Rhodamine B degradation, a study by Kujur *et al.* [44] were able to degrade RhB up to 89.5% with KNN powder synthesized via solid-state reaction. In this work, the best performers were KNN powder, 10 and 30 wt% KNN composites, considering the removal efficiency at the end of the test and their overall trend. Their removal percentages were 71.23% for 30 wt% KNN, 67.05% for KNN powder, and 55.54% for 10 wt% KNN composite. Compared to the piezocatalysis tests, the efficiency is almost the same, but the behavior is more stable, as mentioned before.

As piezocatalysis, after the photocatalysis samples were measured, no visible change in the coloration was appreciated.

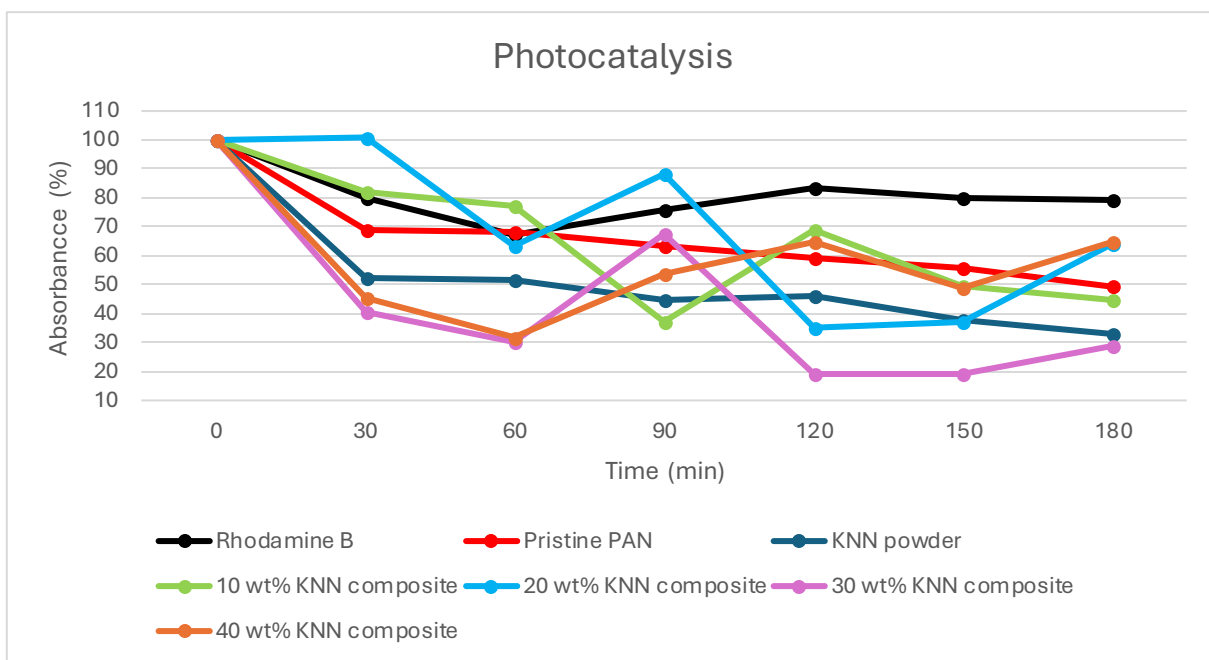


Figure 32. Photocatalysis samples tested from 0 to 180 min, including the dye itself, the control groups and the composite materials.

11.3.3. Piezo-photocatalysis

Finally, the piezo-photocatalysis tests combined the piezoelectric and the photocatalytic properties of both KNN and PAN, and the results are shown in Figure 33.

The first sample that is seemingly the best of the group, is the KNN powder, staying at the same concentration for almost three hours, which could indicate that less time would be required to degrade the dye instead of staying in the solution for 3 hours. Another sample that has a great trend is the other control sample, PAN. It is not as effective as KNN at the beginning, but at the end, it shows a similar reduction in dye concentration. From the composite materials, and from previous catalytic tests, adding above 30 wt% of KNN load into the electrospinning solution is not effective for dye degradation compared to samples that have a lower ceramic load, such as 10 wt% in piezocatalysis, and 10 and 30 wt% in photocatalysis. Furthermore, this could be correlated to the difficulty of electrospinning the 40 wt% KNN solution and its appearance before stabilizing the sample.

The 30 and 40 wt% KNN samples were less effective than the control groups. Lastly, 10 and 20 wt% composites had a degradation capacity comparable to the pristine PAN, but the 20 wt% sample had a higher degradation capacity after 120 min. This is why it was chosen, side by side with the control groups, to repeat the tests and measure that it was the best performer from this composites group. Also, the 10 wt% KNN sample started to show a bleached color in the overall surface, which will be shown in the next section.

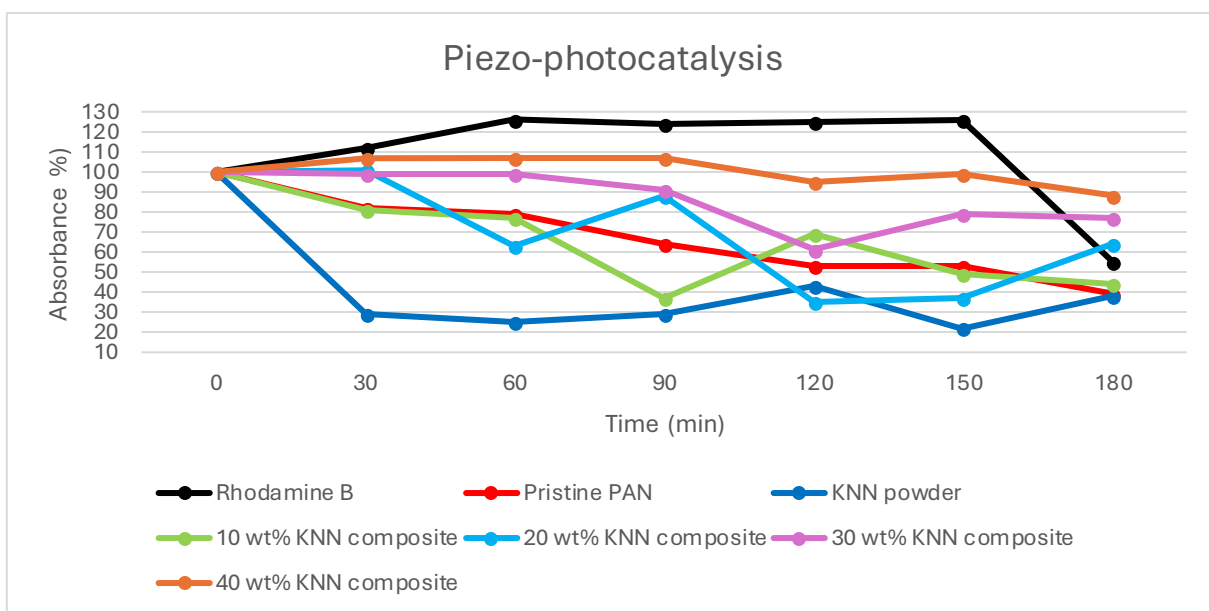


Figure 33. Piezo-photocatalysis samples tested from 0 to 180 min, including the dye itself, the control groups and the composite materials.

In Figure 34 the second and third repetition are shown. Using the piezo-photocatalytic measurement of the RhB, each graph shows four samples: the pristine PAN and KNN powder (control groups), and the 20 wt% KNN composite. As observed in Figure 33, the composite material shows a similar degradation capacity to that of the pristine fibers, with the KNN powder still being the leader in the piezo-photocatalysis activity. In the KNN case, it has both the piezoelectric and the

photocatalytic properties, which could explain why the powder had the highest performance in the piezo-photocatalysis tests.

However, the order changes with the third repetition, where the composite material surpasses the catalytic activity of the control groups. It could be possible that the continuous use of the 20 wt% KNN mat enhanced the piezo-photocatalytic activity, making it more efficient the more it is used. The average degradation efficiency for pristine PAN was 43.67%, for KNN powder was 54.02% and for the 20 wt% KNN composite was 45.46%. Comparing these results to the piezo- and photocatalytic tests, it is the weakest among the three activity tests that were done for this project.

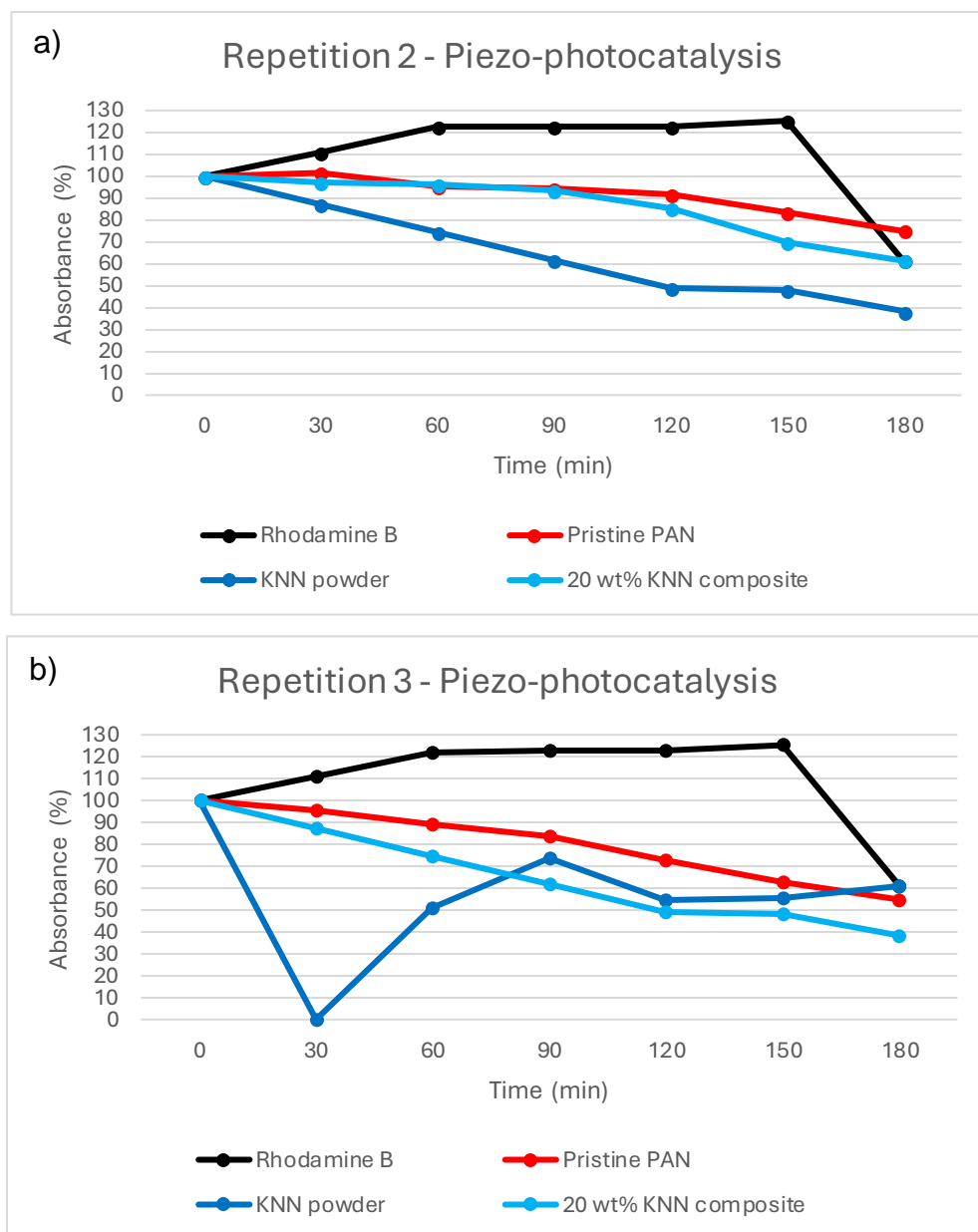


Figure 34. Repetitions of the piezo-photocatalysis tests, with the best composite material (20 wt%), along with the control groups (pristine PAN and KNN powder). a) 2nd repetition; and b) 3rd repetition.

Looking at the results from the control groups and the composite material chosen to repeat the piezo-photocatalytic test (20 wt% KNN), an average absorbance value was calculated for these three cases, shown in Table 11. Even though the KNN powder showed the best performance, the 20 wt% KNN composite was the only one that showed a distinct color change in its samples, as will be discussed in the next section.

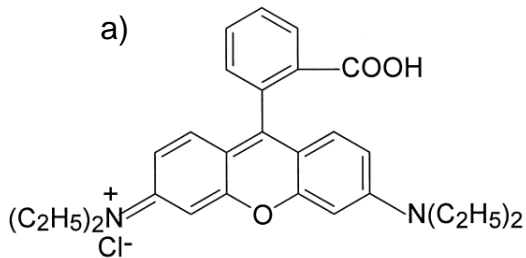
Table 11. Average absorbance (a.u.) of the piezo-photocatalysis tests, including the first round and the two repetitions with the best performer (20 wt% KNN composite) and the control groups (pristine PAN and KNN powder).

Sample	Average absorbance (a.u.)						
	0 min	30 min	60 min	90 min	120 min	150 min	180 min
Pristine PAN (Control)	1.6658 ± 0.0217	1.5495 ± 0.1600	1.4633 ± 0.1212	1.3437 ± 0.2497	1.2060 ± 0.3156	1.1012 ± 0.2476	0.9367 ± 0.2869
KNN powder (Control)	1.6964 ± 0.0503	0.9768 ± 0.6649*	0.8404 ± 0.4015	0.9251 ± 0.3705	0.8269 ± 0.0661	0.7037 ± 0.2876	0.7785 ± 0.2165
20 wt% KNN composite	1.6638 ± 0.0103	1.5820 ± 0.1235	1.2987 ± 0.2710	1.3518 ± 0.2811	0.9378 ± 0.4255	0.8605 ± 0.2752	0.9079 ± 0.1219

In Table 11, the asterisk mark (*) at the 30 min aliquot of KNN powder has a high standard deviation because when recovering the liquid after centrifuging the powder, part of the liquid was lost and the measurement in UV-Vis was practically the same as of water, and as it can be seen in Figure 34 b).

As a conclusion to these tests, in Figure 35 the UV-Vis spectra for the control groups and the 20 wt% KNN composite are shown. Before, it was mentioned that the piezo-photocatalysis tests were the weaker among the catalytic tests, but with the 20 wt% KNN sample there was a behavior with the two highest peaks of RhB that were not seen in any other sample, and this was part of the reason why it was chosen to repeat the piezo-photocatalysis tests.

The onset for RhB is 550 nm [28], but for the most part of the samples, this onset went from 554 nm down to 530, creating a shift towards blue that is even more visible in Figure 35c, the one corresponding to 20 wt% KNN sample. From the same study where they used KNN powder [28], the behavior of the dye degradation is more like the pristine PAN sample, a decrease in the main peak around 550 nm, and the shoulder to the left of it also reduces its size. The shoulder around 500 nm and the slight hypsochromic shift (to a lower wavelength) in the pristine PAN sample correlate to the *N*-deethylation of RhB. The *N*-deethylation is the process where one of the two ethyl groups in the chemical structure of RhB (Figure 35 d)) is reduced and leaves a radical open for the further reduction of the dye [123]. This change in the chemical structure causes the blue shift and the increase in the shoulder to the left of the absorbance peak.

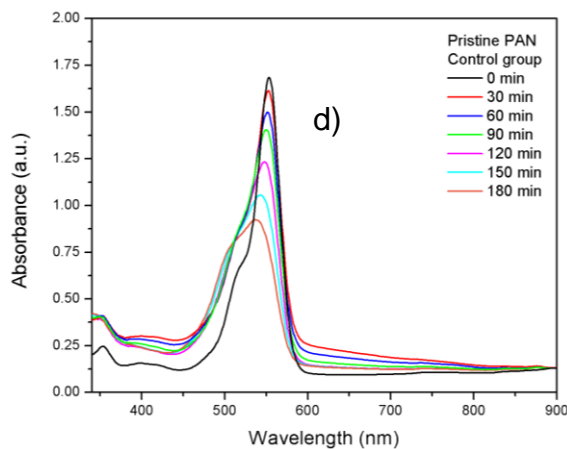


Rhodamine B

b)

; d) chemical structure of *Rhodamine B*

c)



[123].

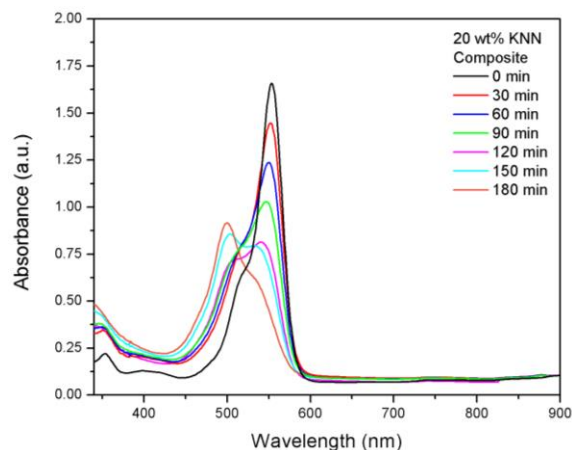
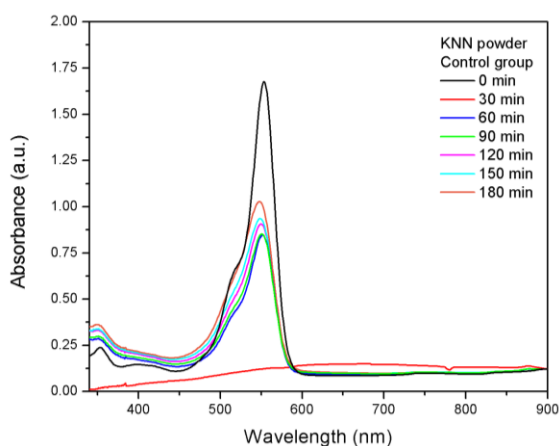


Figure 34. UV-Vis spectra from the third repetition samples from piezo-photocatalysis: a) pristine PAN, b) KNN powder and c) 20 wt% KNN composite.

11.3.4. Analysis of Post-catalysis Tests

After the catalysis tests, the third repetition of piezo-photocatalysis using the 20 wt% KNN composite mat presented the most noticeable color change, as can be

seen in Figure 36. No other sample presented this coloration change, even though the graphs discussed above hinted a reduction in the RhB concentration.



Figure 36. Rhodamine B degradation, obtained from the third repetition of piezo-photocatalysis using 20 wt% KNN composite after a) 30 min, b) 60 min, c) 90 min, d) 120 min, e) 150 min and f) 180 min of degradation.

Image conditions: Camera Canon EOS 1300D Rebel T6 with an 18 - 55 mm lens, f: 5, ISO: 400, focal distance: 41 mm, speed: 1/100 s, with a white background.

The mats were evaluated with FT-IR after being used several times in the tests, and their spectra is shown in Figure 37. For the pristine PAN sample, the appearance of a belly in the region of 3500 cm^{-1} could indicate that the fibers were absorbing part of the dye and water from the solution, and even after being dried in a hot plate at $90\text{ }^{\circ}\text{C}$ for 15 minutes, they presented some form of degradation, but more studies are required to be able to confirm that this degradation is taking place: accelerated aging tests under UV conditions, gas chromatography to analyze decomposition products, and oxidative induction time. In the case of the 10 wt% composite, the peaks are drastically reduced, compared to the other composites that still present a similar shape to those in Figure 23. While looking at the images below Figure 37, it can be inferred that the bleaching process of the fibers directly affects the FT-IR spectrum, as the 10 wt% KNN composite presents the highest contrast between the fibers before and after the degradation tests.

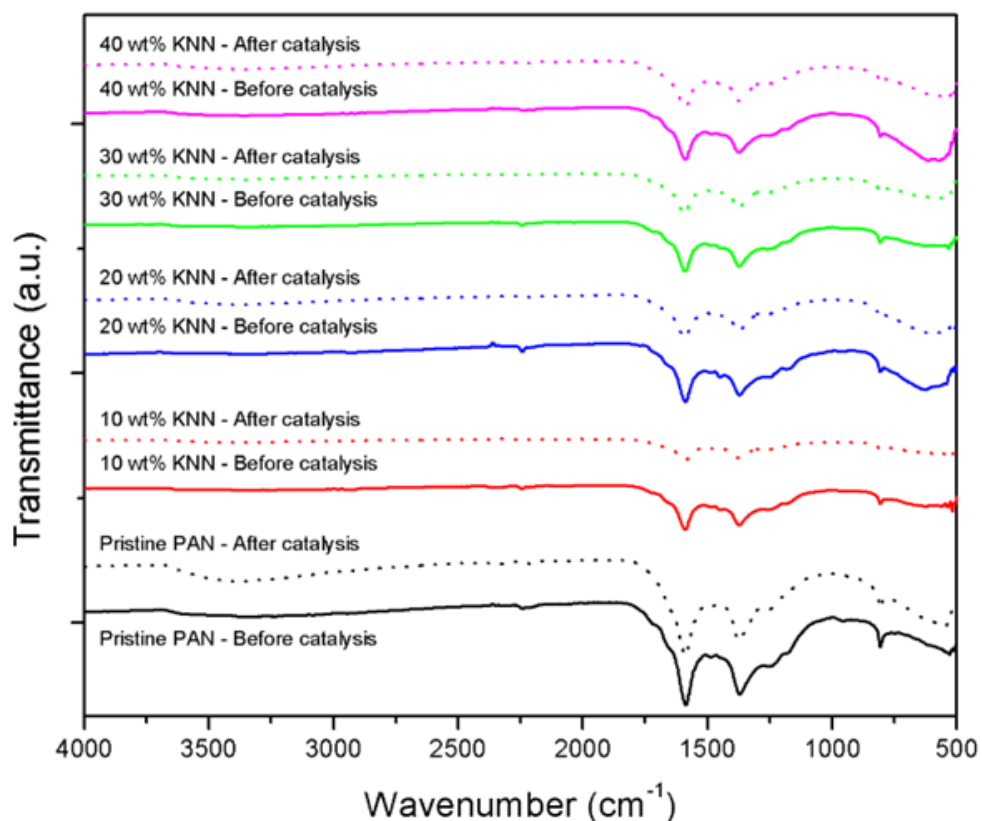


Figure 37. FT-IR spectra from the mats before and after being used in the catalysis tests.

The same camera model (Canon EOS 1300D) from the dye samples was used for taking comparison pictures between fibers from the same batch before and after the catalysis tests. While preparing the mats for the tests, all were equally weighed to be 15 mg, but some mats were bigger than the others, as they did not have the same volume of fibers. For example, pristine PAN, 20 wt% and 40 wt% mats were the biggest in size compared to 10 wt% and 30 wt%. To have 15 mg of the mats, they needed to be cut, and the comparison images have smaller strips from the same batches, so that all the samples would have the same conditions for the degradation tests.

The effect of the corona poling, and the absorption of the dye, can be seen mostly in Figure 38, corresponding to pristine PAN mats. Smaller holes can be seen in the edges of the fibers, presumably due to the lower volume of fibers that appeared after the corona poling was done. The other mats also presented these holes, but they are more visible in the pristine sample. Continuing with Figures 38c and 38e,

some darker circles appeared in the surface. A darker shade could indicate the places where the dye was absorbed, but also could be related to the agglomeration of ceramic nanoparticles discussed in Figure 26. Another explanation could be that the concentration of dye occurred in the holes left by the corona poling (Figure 30), but with the current tools and measurements it would be difficult to confirm that this is what happened to the mats.

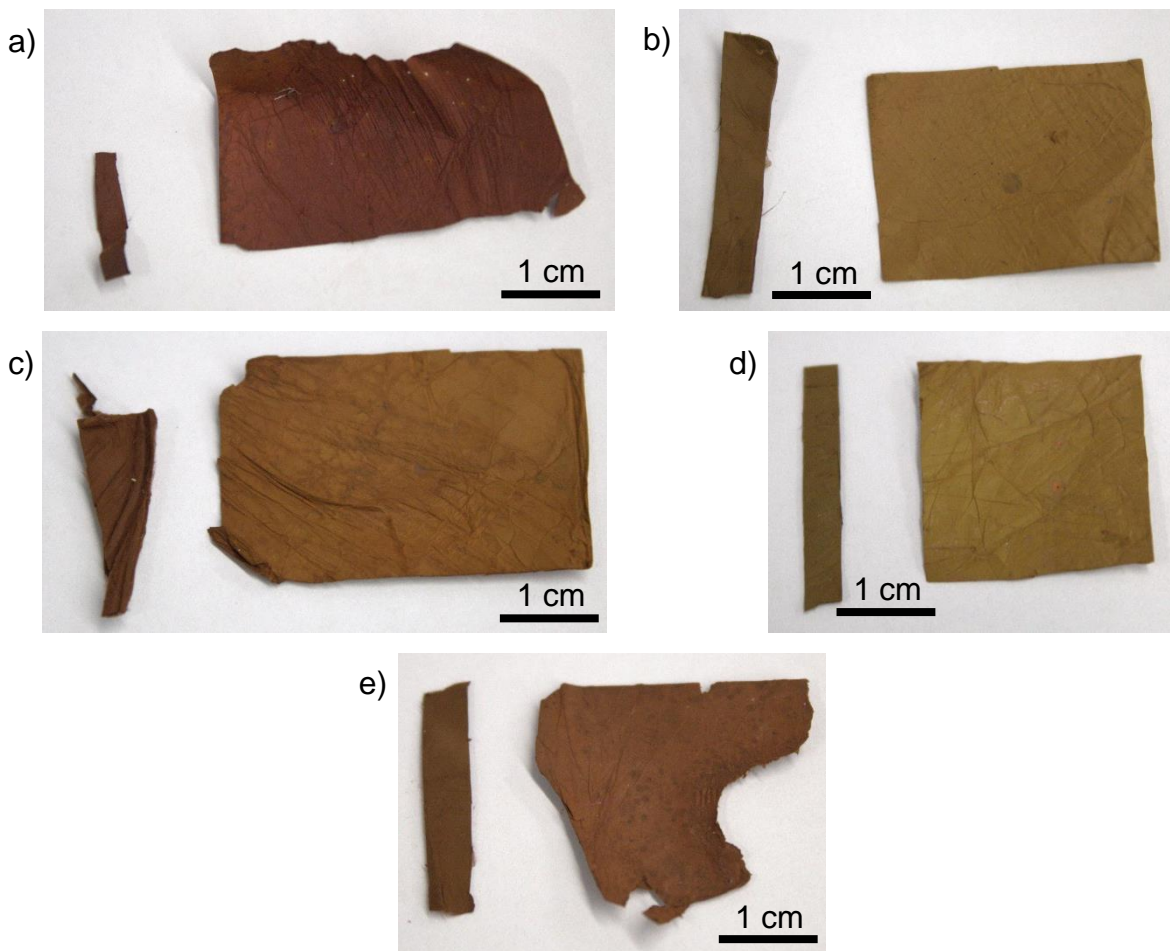


Figure 38. Images comparing fibers from the same match, before and after the catalysis tests: a) pristine PAN, b) 10 wt% KNN composite, c) 20 wt% KNN composite, d) 30 wt% KNN composite, and e) 40 wt% KNN composite. Images conditions: Canon EOS 1300D Rebel T6 with an 18 - 55 mm lens, f: 5.6, ISO: 640, focal distance: 55 mm, speed: 1/100 s, with a white paper background.

Lastly, in the 40 wt% KNN composite a big hole was made in the center of the mat, where the light from the top-down lamp fell upon the sample after the piezophotocatalysis test. Also, the quartz lid could have acted as a magnifying glass, thus

creating this hole. This is the only case where this happened, and it could be concluded that the thinner the mat is, the easier it is for the light to perforate a hole and degrade the sample. From the FT-IR spectrum (Figure 37), the measurement was taken from the edge where the hole was, but there does not appear to be a difference in the composition of the fibers. In Figure 39, an image taken from above the vessel after the piezo-photocatalysis test was finished shows that the mat was only pierced in the center, but once it was removed from the liquid, it broke apart, as seen in Figure 39 b).

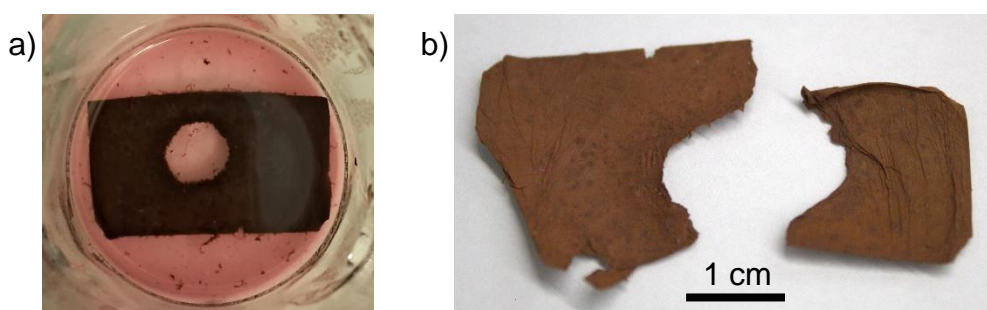


Figure 39. a) Image taken of the 40 wt% KNN composite, showing the hole on the sample. Image conditions: Samsung Galaxy A14 5G, f: 1.8, ISO: 640, focal distance: 26 mm, speed: 1/30 s. b) The same sample after it was removed from the liquid and dried on a hot plate. Image conditions: Canon EOS 1300D Rebel T6, f: 5.6, ISO: 640, focal distance: 47 mm, speed: 1/100 s.

Overall, the 20 wt% KNN composite had the highest performance from the composite materials group in the piezo-photocatalysis test with a second place, behind the KNN powder, and even though it was similar in size as the 40 wt% sample, it did not suffer any destruction after 5 catalytic tests, compared to the 3 tests that the 40 wt% KNN composite underwent.

11.4. Summary of Results

A combination of tetragonal and orthorhombic phases of $\text{K}_{0.48}\text{Na}_{0.52}\text{NbO}_3$ were obtained via solid-state reaction with manual milling, confirmed with X-Ray Diffraction and Rietveld refinement, with a shift to the right compared to $\text{K}_{0.50}\text{Na}_{0.50}\text{NbO}_3$, as the cationic ratio in the A site changes. The average crystallite size was 22.32 ± 6.69 nm using the Scherrer equation.

Measuring uncalcined powder with Thermogravimetric Analysis – Differential Thermal Analysis, the lowest calcination temperature that preserved a pure crystalline phase was 800 °C. The density in bulk of 48:52 composition sintered at 1100 °C for two hours was 3.45 g/cm³.

The ceramic particles were observed with Scanning Electron Microscopy, and with the use of the Energy Dispersive X-Ray Spectroscopy the atomic percentage of sodium, potassium, niobium, and oxygen was calculated. After 6 hours of post-calcination milling, the atomic percentage of the elements was close to the theoretical values.

The particle size was reduced via high-energy post-calcination milling, and a filter with 0.1 µm pore size was used to obtain only particles below 100 nm in size for the electrospinning solutions. Using the 0, 6 and 12-hours milled powder in Ultraviolet-Visible Spectroscopy, the optical band gap for the potassium sodium niobate resulted in 3.94 eV for the powder after 0 hours of milling, and 3.92 eV after 12 hours of milling. With the reduction of the particle size, the optical band gap of this ceramic powder decreased by 0.02 eV after 12 hours of high energy post-calcination milling, calculated with Kubelka-Munk modified Tauc plot.

It was confirmed with the use of Fourier Transform Infrared Spectroscopy that potassium sodium niobate loses the organic matter after the calcination, as the organic bonds at 2339 and 2359 cm⁻¹ from the reagents disappear and the interaction between niobium and oxygen showed a deep peak at 615 cm⁻¹. The vibrational modules were measured with Raman Spectroscopy, and as happened with Infrared Spectroscopy, the 48:52 composition had a left shift compared to the 50:50 composition. With Raman it was also confirmed that one of the phases present in the KNN is the spatial group Amm2, an orthorhombic structure; the vibrations correspond to the Nb-O₆ octahedra and movement in the alkali elements within the structure at 142 cm⁻¹.

The polyacrylonitrile fibers were successfully electrospun with a voltage of 17.5 kV, reduced to 15 kV once the ceramic load for the composite mats increased. The fibers and composites were measured with X-Ray Diffraction, where the two polyacrylonitrile peaks in 17° and 29° (2θ) were presented, but lacked sharpness

compared to the background. Once the ceramic nanoparticles were included in the solution, these peaks gained sharpness but were reduced above 30 wt% ceramic load. The niobate peaks also appeared in the composite material but, as was the case with the polyacrylonitrile peaks, they lost sharpness, and the peaks above 45° (2θ) changed their form.

The increasing ceramic load reduced the stabilization temperature, from 298.36°C in pristine fibers, to 264.80°C with a 40 wt% niobate load, but did not affect the pristine fibers peaks in Infrared Spectroscopy. The only visible change was the increase of the niobium-oxygen bond with a higher ceramic load. Regarding the vibrational modes in Raman, only the vibrations related to the graphitic structure of the fibers appeared, and the presence of the potassium sodium niobate increased the intensity of the peaks. A correlation could exist between the reduction in the stabilization temperature and the intensity increase in the Raman vibrational modes of the fibers and the composites.

Once the nanoparticles were electrospun with the polymeric solution and stabilized, the fibers were observed with Scanning Electron Microscopy, where the agglomeration of the particles was clearly observed, but they were still distributed among the fibers with the load increase. When the agglomerate was bigger in size, it tended to bend as to create a micelle, and it could be related to the static nature of the nanoparticles and the voltage at which the electrospinning process took place.

After the samples were poled with the corona effect, visible holes were observed in the fibers surface, and with Scanning Electron Microscopy it was concluded that the fibers were melted at the edges and on the layers underneath the holes. The nanoparticles were unveiled where the fibers retracted in a charred manner rather than melted.

Continuing with the catalysis tests, the best performers in piezocatalysis were 10 wt% KNN composite (76.71% removal efficiency), pristine PAN (69.14%) and KNN powder (61.40%); in photocatalysis were 30 wt% KNN (71.23%), KNN powder (67.05%), and 10 wt% KNN composite (55.54%). Lastly, the principal test for this project, piezo-photocatalysis, had the following samples as best performers: KNN powder (54.02%), 20 wt% KNN composite (45.46%) and pristine PAN (43.67%). The

only visible change in the dye color was with the 20 wt% KNN sample after the third piezo-photocatalytic test, going from a bright pink to a washed yellow, almost transparent.

XII. Conclusions

The existence of an orthorhombic phase in $\text{K}_{0.48}\text{Na}_{0.52}\text{NbO}_3$ was confirmed with Rietveld refinement after the X-Ray Diffraction patterns obtained from powder calcined at 800 °C.

By reducing the particle size with post-calcination milling, the composite materials with ceramic nanofillers and polyacrylonitrile fibers were successfully electrospun. The composite materials did show a reduction in the stabilization temperature from 298.36 °C in pristine fibers to 264.80 °C with a 40 wt% load of potassium sodium niobate nanoparticles.

Visually, the fibers were continuous and had the presence of agglomeration of the nanoparticles when the load increased, mostly in the samples with 30 and 40 wt% filler. These agglomeration were exposed after the corona poling was done, after increasing the temperature of the polymer and shrinking the fibers.

By poling the samples with corona discharge, the nanoparticles were exposed after the voltage burned the PAN nanofibers, which could lead to a higher efficiency in the catalysis tests by increasing the reaction area of the KNN particles. The addition of 20 wt% from $\text{K}_{0.48}\text{Na}_{0.52}\text{NbO}_3$ ceramic nanoparticles obtained from a solid-state route to a 10 wt% polyacrylonitrile solution and synthesized via electrospinning, can degrade Rhodamine B with 45.46% efficiency after three hours with piezo-photocatalysis.

XIII. Recommendations

A mechanical study of the fibers can be used to elucidate if the ceramic nanoparticles have any effect on the mechanical properties, as well as contact angle measurement for these hydrophilic fibers.

If a higher ceramic load is to be electrospun, reducing the PAN concentration or modifying the voltage are key for a successful fibers production, which can also be measured with rheology.

Other sets of applications can be explored for these composite materials, such as the energy conversion potential and HEPA (High Efficiency Particulate Air) filters for industry wastes.

To have a better view of the degradation, the piezo- and photocatalysis tests need to be repeated to have an average, as well as the rest of the composite materials that were not used in the second and third repetition. The subproducts from the Rhodamine B degradation need to be studied in case these can be further degraded or do not present any other harmful property.

Another test that could be useful for these fibers is to determine how many cycles these fibers are resistant for, comparing the 20 and 40 wt% KNN samples, where the first resisted five tests and the second only resisted three tests before degrading.

Finally, the reaction mechanism of the KNN + PAN composites could be studied to understand the effect that it has on Rhodamine B and, furthermore, if it could be used for other dyes.

XIV. References

1. Shinekumar K, Dutta S (2014) High-Temperature Piezoelectrics with Large Piezoelectric Coefficients. *J Electron Mater* 44:613–622
- [1] Cady, W. G. (1964). *Piezoelectricity; An Introduction to the Theory and Applications of Electromechanical Phenomena in Crystals*. Dover Publications, 1st edition, 1-450.
- [2] Shinekumar, K., & Dutta, S. (2015). *High-Temperature Piezoelectrics with Large Piezoelectric Coefficients*. *Journal of Electronic Materials*, 44(2), 613-622. DOI: 10.1007/s11664-014-3534-2
- [3] Vijatovic, M. M., Bobic, J. D., & Stojanovic, B. D. (2008). *History and challenges of barium titanate: Part I*. *Science of Sintering*, 40(2), 155-165. DOI: 10.2298/SOS0802155V
- [4] Panda, P. K., & Sahoo, B. (2015). *PZT to Lead Free Piezo Ceramics: A Review*. *Ferroelectrics*, 474(1), 128-143. DOI: 10.1080/00150193.2015.997146
- [5] Saravanan, R., Gracia, F., & Stephen, A. (2017). *Basic Principles, Mechanism, and Challenges of Photocatalysis*. *Nanocomposites for Visible Light-induced Photocatalysis*, Springer Series on Polymer and Composite Materials, 19-40. DOI: 10.1007/978-3-319-62446-4_2
- [6] Byrne, C., Subramanian, G., & Pillai, S. (2018). *Recent advances in photocatalysis for environmental applications*. *Journal of Environmental Chemical Engineering*, 3(6), 3531-3555. DOI: 10.1016/j.jece.2017.07.080
- [7] Shirane, G., Newnham, R., & Pepinsky, R. (1954). *Dielectric Properties and Phase Transitions of NaNbO_3 and $(\text{Na,K})\text{NbO}_3$* . *Physical Review*, 96(3), 581-588. DOI: 10.1103/PhysRev.96.581
- [8] Dai, Y. J., Zhang, X. W., & Chen, K. P. (2009). *Morphotropic phase boundary and electrical properties of $\text{K}_{1-x}\text{Na}_x\text{NbO}_3$ lead-free ceramics*. *Applied Physics Letters*, 94(4), 042905. DOI: 10.1063/1.3076105

- [9] Saito, Y., Takao, H., Tani, T., Nonoyama, T., Takatori, K., Homma, T., Nagaya, T., & Nakamura, M. (2004). *Lead-free piezoceramics*. *Nature*, 432(7013), 84-87. DOI: 10.1038/nature03028
- [10] Li, P., Zhai, J., Shen, B., Zhang, S., Li, X., Zhu, F., & Zhang, X. (2018). *Ultrahigh Piezoelectric Properties in Textured (K,Na)NbO₃-Based Lead-Free Ceramics*. *Advanced Materials*, 30(8), 1705171. DOI: 10.1002/adma.201705171
- [11] Xu, K., Li, J., Lv, X., Wu, J., Zhang, X., Xiao, D., & Zhu, J. (2016). *Superior Piezoelectric Properties in Potassium-Sodium Niobate Lead-Free Ceramics*. *Advanced Materials*, 28(38), 8519-8523. DOI: 10.1002/adma.201601859
- [12] Topolov, V. Yu., & Isaeva, A. N. (2017). *High piezoelectric sensitivity and related parameters of a novel lead-free 1–0–3 composite*. *Ferroelectrics Letters Section*, 44(4-6), 73-80. DOI: 10.1080/07315171.2017.1397461
- [13] Shi, C., Ma, J., Wu, J., Wang, X., Miao, F., Huang, Y., Chen, K., Wu, W., & Wu, B. (2020). *Coexistence of excellent piezoelectric performance and high Curie temperature in KNN-based lead-free piezoelectric ceramics*. *Journal of Alloys and Compounds*, 846, 156245. DOI: 10.1016/j.jallcom.2020.156245
- [14] Wang, X., Wu, J., Xiao, D., Cheng, X., Zheng, T., Lou, X., Zhang, B., & Zhu, J. (2014). *New Potassium–Sodium Niobate Ceramics with a Giant d_{33}* . *ACS Applied Materials & Interfaces*, 6(9), 6177-6180. DOI: 10.1021/am500819v
- [15] Li, F., Tan, Z., Xing, J., Jiang, L., Wu, B., Wu, J., Xiao, D., & Zhu, J. (2017). *Investigation of new lead free (1-x)KNNS–xBKZH piezo-ceramics with R–O–T phase boundary*. *Journal of Materials Science: Materials in Electronics*, 28(12), 8803-8809. DOI: 10.1007/s10854-017-6607-1
- [16] Zhang, Y., Zhai, J., & Xue, S. (2020). *Effect of three step sintering on piezoelectric properties of KNN-based lead free ceramics*. *Chemical Physics Letters*, 758, 137906. DOI: 10.1016/j.cplett.2020.137906
- [17] Yang, W., Li, P., Wu, S., Li, F., Shen, B., & Zhai, J. (2020). *Coexistence of excellent piezoelectric performance and thermal stability in KNN-based lead-free piezoelectric ceramics*. *Ceramics International*, 46(2), 1390-1395. DOI: 10.1016/j.ceramint.2019.09.102

- [18] Fikentscher, H., & Heuck, C. (1938). *Verfahren zur Herstellung von Polymerisationsprodukten*. Deutsches Reich, Reichspatentamt Patentschrift Nr 654989. <https://depatisnet.dpma.de/DepatisNet/depatisnet?window=1&space=menu&content=treffer&action=bibdat&docid=DE000000654989A>
- [19] Bode, H. (1998). *Geschichte der Chemiefaserindustrie der Deutschen Demokratischen Republik*. Mitteilungen der Gesellschaft Deutscher Chemiker, 14, 158-169. [20] Zhao, L., Li, Y., Zhao, Y., Feng, Y., Feng, W., & Yuan, X. (2012). *Carbon nanotubes grown on electrospun polyacrylonitrile-based carbon nanofibers via chemical vapor deposition*. Applied physics A: Materials Science & Processing, 108, 863-869. DOI: 10.1007/s00339-012-6770-4
- [21] Nadarajah, A., Lawrence, J. G., & Hughes, T. W. (2008). *Development and Commercialization of Vapor Grown Carbon Nanofibers: A Review*. Key Engineering Materials, 380, 196-206. DOI: 10.4028/www.scientific.net/KEM.380.193
- [22] Tibbetts, G. G., Lake, M. L., Strong, K. L., & Rice, B. P. (2007). *A review of the fabrication and properties of vapor-grown carbon nanofiber/polymer composites*. Composites Science and Technology, 67, 1709-1718. DOI: 10.1016/j.compscitech.2006.06.015
- [23] Nataraj, S. K., Yang, K. S., & Aminabhavi, T. M. (2012). *Polyacrylonitrile-based nanofibers – A state-of-the-art review*. Progress in Polymer Science, 37, 487-513. DOI: 10.1016/j.progpolymsci.2011.07.001
- [24] Duclaux, L., Frackowiak, E., Gibinski, T., Benoit, R., & Beguin, F. (2006). *Clay/Carbon Nanocomposites as Precursors of Electrode Materials for Lithium-Ion Batteries and Supercapacitors*. Molecular Crystals and Liquid Crystals Science and Technology. Section A. Molecular Crystals and Liquid Crystals. 340(1), 449-454. DOI: 10.1080/10587250008025507
- [25] Qin, X. H., Wan, Y. Q., He, J., H., Zhang, J., Yu, J. Y., & Wang, S. Y. (2004). *Effect of LiCl on electrospinning of PAN polymer solution: theoretical analysis and experimental verification*. Polymer, 45, 6409-6413. DOI:

- 10.1016/j.polymer.2004.06.031 [26] Park, S. H., Jo, S. M., Kim, D. Y., Lee, W. S., & Kim, B. C. (2005). *Effects of iron catalyst on the formation of crystalline domain during carbonization of electrospun acrylic nanofiber*. Synthetic metals, 150, 265-270. DOI: 10.1016/j.synthmet.2005.02.010
- [27] Béguin, F., Szostak, K., Lota, G., & Frackowiak, E. (2005). *A Self-Supporting Electrode for Supercapacitors Prepared by One-Step Pyrolysis of Carbon Nanotube/Polyacrylonitrile Blends*. Advanced Materials, 17, 2380-2384. DOI: 10.1002/adma.200402103
- [28] Wang, Y., Yang, Q., Shan, G., Wang, C., Du, J., Wang, S., Li, Y., Chen, X., Jing, X., & Wei, Y. (2005). *Preparation of silver nanoparticles dispersed in polyacrylonitrile nanofiber film spun by electrospinning*. Materials Letters, 59, 3046-3049. DOI: 10.1016/j.matlet.2005.05.016
- [29] Maensiri, S., & Nuansing, W. (2006). *Thermoelectric oxide NaCo₂O₄ nanofibers fabricated by electrospinning*. Materials Chemistry and Physics, 99, 104-108. DOI: 10.1016/j.matchemphys.2005.10.004
- [30] Yang, Y., Wang, H., Lu, X., Zhao, Y., Li, X., & Wang, C. (2007). *Electrospinning of carbon/CdS coaxial nanofibers with photoluminescence and conductive properties*. Materials Science and Engineering B, 140, 48-52. DOI: 10.1016/j.mseb.2007.03.010
- [31] Kim, C., Ngoc, B. T. N., Yang, K. S., Kojima, M., Kim, Y. A., Kim, Y. J., Endo, M., & Yang, S. C. (2007). *Self-Sustained Thin Webs Consisting of Porous Carbon Nanofibers for Supercapacitors via the Electrospinning of Polyacrylonitrile Solutions Containing Zinc Chloride*. Advanced Materials, 19, 2341-2346. DOI: 10.1002/adma.200602184
- [32] Im, J. S., Park, S. J., Kim, T. J., Kim, Y. H., & Lee, Y. S. (2008). *The study of controlling pore size on electrospun carbon nanofibers for hydrogen adsorption*. Journal of Colloid and Interface Science, 318, 42-49. DOI: 10.1016/j.jcis.2007.10.024
- [33] Zhang, R., Ma, Y., Lan, W., Sameen, D. R., Ahmed, S., Dai, J., Qin, W., Li, S., & Liu, Y. (2021). *Enhanced photocatalytic degradation of organic dyes by ultrasonic-assisted electrospray TiO₂/graphene oxide on polyacrylonitrile/ β -*

- cyclodextrin nanofibrous membranes*. Ultrasonics – Sonochemistry, 70, 105343(1-18). DOI: 10.1016/j.ultsonch.2020.105343
- [34] Baker, D. W., Thomas, P. A., Zhang, N., & Glazer, A. M. (2009). *A comprehensive study of the phase diagram of $K_xNa_{1-x}NbO_3$* . Applied Physics Letters, 95(9), 091903. DOI: 10.1063/1.3212861
- [35] Momma, K., & Izumi, F. (2011). *VESTA 3 for three-dimensional visualization of crystal, volumetric and morphology data*. Journal of Applied Crystallography, 44(6), 1272-1276. DOI: 10.1107/S0021889811038970
- [36] Jaffe, H. (1958). *Piezoelectric Ceramics*. Journal of the American Ceramic Society, 41(11), 494-498. DOI: 10.1111/j.1151-2916.1958.tb12903.x
- [37] Ahtee, M., & Glazer, A. M. (1976). *Lattice parameters and tilted octahedra in sodium–potassium niobate solid solutions*. Acta Crystallographica Section A, 32(3), 434-446. DOI: 10.1107/S0567739476000983
- [38] Wu, J., Xiao, D., & Zhu, J. (2015). *Potassium–Sodium Niobate Lead-Free Piezoelectric Materials: Past, Present, and Future of Phase Boundaries*. Chemical Reviews, 115(7), 2559-2595. DOI: 10.1021/cr5006809
- [39] Hao, J., Li, W., Zhai, J., & Chen, H. (2019). *Progress in high-strain perovskite piezoelectric ceramics*. Materials Science and Engineering: R: Reports, 135, 1-57. DOI: 10.1016/j.mser.2018.08.001
- [40] Safari, A., Jadidian, B., & Akdogan, E. K. (2000). *Piezoelectric Composites for Transducer Applications*. Comprehensive Composite Materials, 5, 533-561. DOI: 10.1016/B0-08-042993-9/00095-4
- [41] Zhang, S., Xia, R., & Shrout, T. R. (2007). *Lead-free piezoelectric ceramics vs. PZT?* Journal of Electroceramics, 19(4), 251-257. DOI: 10.1007/s10832-007-9056-z
- [42] Leontsev, S. O., & Eitel, R. E. (2010). *Progress in engineering high strain lead-free piezoelectric ceramics*. Science and Technology of Advanced Materials, 11(4), 044302. DOI: 10.1088/1468-6996/11/4/044302
- [43] Mabud, S. A. (1980). *The morphotropic phase boundary in PZT solid solutions*. Journal of Applied Crystallography, 13(3), 211-216. DOI: 10.1107/S0021889880011958

- [44] Kujur, V. S., Gaur, R., Gupta, V., & Singh, S. (2022). *Significantly enhanced UV-light-driven photocatalytic performance of ferroelectric (K_{0.5}Na_{0.5})NbO₃: Effect of corona-poling and particle size*. Journal of Physics and Chemistry of Solids, 167, 110751(1-9). DOI: 10.1016/j.jpcs.2022.110751
- [45] Lu, J., Lin, H., Hong, R., & Zhang, D. (2022). *Photocatalytic H₂ evolution properties of K_{0.5}Na_{0.5}NbO₃ (KNN) with halloysite nanotubes*. Optical Materials, 129, 112516. DOI: 10.1016/j.optmat.2022.112516
- [46] Yu, F., Ma, B., Xie, Z., Wang, P., Wu, X., Lin, C., Zhao, C., Gao, M., Luo, L., & Zhang, Q. (2023). *Developing «smart windows» for optical storage and temperature sensing based on KNN transparent ceramics*. Journal of the European Ceramic Society, 43(10), 4408-4418. DOI: 10.1016/j.jeurceramsoc.2023.03.034
- [47] Kumar, P., Pattanaik, M., & Sonia. (2013). *Synthesis and characterizations of KNN ferroelectric ceramics near 50/50 MPB*. Ceramics International, 39(1), 65-69. DOI: 10.1016/j.ceramint.2012.05.093
- [48] Du, H., Li, Z., Tang, F., Qu, S., Pei, Z., & Zhou, W. (2006). *Preparation and piezoelectric properties of (K_{0.5}Na_{0.5})NbO₃ lead-free piezoelectric ceramics with pressure-less sintering*. Materials Science and Engineering: B, 131(1-3), 83-87. DOI: 10.1016/j.mseb.2006.03.039
- [49] Malic, B., Bernard, J., Holc, J., Jenko, D., & Kosec, M. (2005). *Alkaline-earth doping in (K,Na)NbO₃ based piezoceramics*. Journal of the European Ceramic Society, 25(12), 2707-2711. DOI: 10.1016/j.jeurceramsoc.2005.03.127
- [50] Lau, S. T., Li, X., Zhou, Q. F., Shung, K. K., Ryu, J., & Park, D. S. (2010). *Aerosol-deposited KNN–LSO lead-free piezoelectric thick film for high frequency transducer applications*. Sensors and Actuators A: Physical, 163(1), 226-230. DOI: 10.1016/j.sna.2010.08.020
- [51] Briscoe, J., & Dunn, S. (2015). *Piezoelectric nanogenerators – a review of nanostructured piezoelectric energy harvesters*. Nano Energy, 14, 15-29. DOI: 10.1016/j.nanoen.2014.11.059

- [52] Bairagi, S., & Ali, S. W. (2020). *Flexible lead-free PVDF/SM-KNN electrospun nanocomposite based piezoelectric materials: Significant enhancement of energy harvesting efficiency of the nanogenerator*. Energy, 198, 117385. DOI: 10.1016/j.energy.2020.117385
- [53] Verma, A. S., Singh, A., Kumar, D., & Dubey, A. K. (2020). *Electro-mechanical and Polarization-Induced Antibacterial Response of 45S5 Bioglass–Sodium Potassium Niobate Piezoelectric Ceramic Composites*. ACS Biomaterials Science & Engineering, 6(5), 3055-3069. DOI: 10.1021/acsbiomaterials.0c00091
- [54] Ning, X., Hao, A., Cao, Y., Hu, J., Xie, J., & Jia, D. (2020). *Effective promoting piezocatalytic property of zinc oxide for degradation of organic pollutants and insight into piezocatalytic mechanism*. Journal of Colloid and Interface Science, 577, 290-299. DOI: 10.1016/j.jcis.2020.05.082
- [55] Li, Y., Wang, J., Liao, R., Huang, D., & Jiang, X. (2010). *Synthesis and piezoelectric properties of $K_xNa_{1-x}NbO_3$ ceramic by molten salt method*. Journal of Alloys and Compounds, 496(1-2), 282-286. DOI: 10.1016/j.jallcom.2010.01.139
- [56] Sharma, J. P., Kumar, D., & Sharma, A. K. (2021). *Structural and dielectric properties of pure potassium sodium niobate (KNN) lead free ceramics*. Solid State Communications, 334-335, 114345. DOI: 10.1016/j.ssc.2021.114345
- [57] Lu, Y., Lin, J., Wang, P., Yu, F., Wu, X., Lin, C., Zhao, C., Gao, M., Lin, T., & Zhang, Q. (2022). *Self-recoverable photochromism of tape-casting-derived Er-doped potassium sodium niobate thick films via sol-gel route*. Journal of Luminescence, 247, 118875. DOI: 10.1016/j.jlumin.2022.118875
- [58] Ramajo, L. A., Rubio-Marcos, F., Campo, A. D., Fernández, J. F., Castro, M. S., & Parra, R. (2014). *New insights into the properties of $K_xNa_{(1-x)}NbO_3$ ceramics obtained by hydrothermal synthesis*. Ceramics International, 40(9), 14701-14712. DOI: 10.1016/j.ceramint.2014.06.059
- [59] Balsubramanian, A. (2017). *CLASSIFICATION OF MATERIALS*. DOI: 10.13140/RG.2.2.12792.34567

- [60] De Faoite, D., Browne, D. J., Chang-Díaz, F. R., & Stanton, K. T. (2012). *A review of the processing, composition, and temperature-dependent mechanical and thermal properties of dielectric technical ceramics*. Journal of Materials Science, 47(10), 4211-4235. DOI: 10.1007/s10853-011-6140-1
- [61] Fuentes, J., Portelles, J., Durruthy-Rodríguez, M. D., H'Mok, H., Raymond, O., Heiras, J., Cruz, M. P., & Siqueiros, J. M. (2015). *Dielectric and piezoelectric properties of the KNN ceramic compound doped with Li, La and Ta*. Applied Physics A, 118(2), 709-715. DOI: 10.1007/s00339-014-8783-7
- [62] Curie, J., & Curie, P. (1880). *Sur l'électricité polaire dans les cristaux hémièdres à faces inclinées*. CR Acad Sci Gen, 91, 383-6.
- [63] Thomann, H. (1990). *Piezoelectric Ceramics*. Advanced Materials, 2(10), 458-463. DOI: 10.1002/adma.19900021004
- [64] Dineva, P., Gross, D., Müller, R., & Rangelov, T. (2014). *Piezoelectric Materials: Dynamic Fracture of Piezoelectric Materials*. Springer International Publishing, 212, 7-32. DOI: 10.1007/978-3-319-03961-9_2
- [65] Uchino, K. (2017). *The Development of Piezoelectric Materials and the New Perspective*. Advanced Piezoelectric Materials, 1-92. DOI: 10.1016/B978-0-08-102135-4.00001-1
- 66Liu, H., & Yang, X. (2017). *A brief review on perovskite multiferroics*. Ferroelectrics, 507(1), 69-85. DOI: 10.1080/00150193.2017.1283171
- [672] Rödel, J., Jo, W., Seifert, K. T. P., Anton, E. M., Granzow, T., & Damjanovic, D. (2009). *Perspective on the Development of Lead-free Piezoceramics*. Journal of the American Ceramic Society, 92(6), 1153-1177. DOI: 10.1111/j.1551-2916.2009.03061.x
- [683] Rödel, J., Webber, K. G., Dittmer, R., Jo, W., Kimura, M., & Damjanovic, D. (2015). *Transferring lead-free piezoelectric ceramics into application*. Journal of the European Ceramic Society, 35(6), 1659-1681. DOI: 10.1016/j.jeurceramsoc.2014.12.013
- [694] Rahman, A., Jiang, M., Rao, G., Lee, S., Kim, M. H., Habib, M., & Rahman, J. U. (2022). *Improved ferroelectric, piezoelectric, and dielectric properties in pure KNN translucent ceramics by optimizing the normal sintering method*.

- Ceramics International, 48(14), 20251-20259. DOI: 10.1016/j.ceramint.2022.03.305
- [705] Troiler-McKinstry, S. (2020). *Impact of ferroelectricity*. American Ceramic Society Bulletin, 99, 22-30.
- [716] Setter, N. (2016). *What is a ferroelectric—a materials designer perspective*. Ferroelectrics, 500(1), 164-182. DOI: 10.1080/00150193.2016.1232104
- [57] Guan, Z., Hu, H., Shen, X., Xiang, P., Zhong, N., Chu, J., & Duan, C. (2020). *Recent Progress in Two-Dimensional Ferroelectric Materials*. Advanced Electronic Materials, 6(1), 1900818. DOI: 10.1002/aelm.201900818
- [72] Inagaki, M., Kaneko, K., & Nishizawa, T. (2004). *Nanocarbons—recent research in Japan*. Carbon, 42(8-9), 1401-1417. DOI: 10.1016/j.carbon.2004.02.032
- [73] Wang, T., & Kumar, S. (2006). *Electrospinning of polyacrylonitrile nanofibers*. Journal of Applied Polymer Science, 102(2), 1023-1029. DOI: 10.1002/app.24123
- [74] Huang, C., Xu, X., Fu, J., Yu, D. G., & Liu, Y. (2022). *Recent Progress in Electrospun Polyacrylonitrile Nanofiber-Based Wound Dressing*. Polymers, 14(16), 3266. DOI: 10.3390/polym14163266
- [75] Brazdil, J. F. (2012). *Acrylonitrile*. Ullmann's Encyclopedia of Industrial Chemistry, Wiley-VCH Verlag GmbH & Co. DOI: 10.1002/14356007.a01_177.pub3
- [76] Qiao, M., Kong, H., Ding, X., Hu, Z., Zhang, L., Cao, Y., & Yu, M. (2019). *Study on the Changes of Structures and Properties of PAN Fibers during the Cyclic Reaction in Supercritical Carbon Dioxide*. Polymers, 11(3), 402. DOI: 10.3390/polym11030402
- [77] Bai, Y. J., Wang, C. G., Lun, N., Wang, Y. X., Yu, M. J., & Zhu, B. (2006). *HRTEM microstructures of PAN precursor fibers*. Carbon, 44(9), 1773-1778. DOI: 10.1016/j.carbon.2005.12.041
- [78] Khan, W. S., Asmatulu, R., Ceylan, M., & Jabbarnia, A. (2013). *Recent progress on conventional and non-conventional electrospinning processes*. Fibers and Polymers, 14(8), 1235-1247. DOI: 10.1007/s12221-013-1235-8

- [79] Taylor, G. I. (1969). *Electrically driven jets*. Proceedings of the Royal Society of London. A. Mathematical and Physical Sciences, 313(1515), 453-475. DOI: 10.1098/rspa.1969.0205
- [80] Wen, Y., Kok, M. D. R., Tafoya, J. P. V., Sobrido, A. B. J., Bell, E., Gostick, J. T., Herou, S., Schlee, P., Titirici, M. M., Brett, D. J. L., Shearing, P. R., & Jervis, R. (2021). *Electrospinning as a route to advanced carbon fiber materials for selected low-temperature electrochemical devices: A review*. Journal of Energy Chemistry, 59, 492-529. DOI: 10.1016/j.jechem.2020.11.014
- [81] Doshi, J., & Reneker, D. H. (1995). *Electrospinning process and applications of electrospun fibers*. Journal of Electrostatics, 35(2-3), 151-160. DOI: 10.1016/0304-3886(95)00041-8
- [82] Robb, B., & Lennox, B. (2011). *The electrospinning process, conditions, and control*. Electrospinning for Tissue Regeneration, 51-66. DOI: 10.1533/9780857092915.1.51
- [83] Bera, B. (2016). *Literature review on electrospinning process (a fascinating fiber fabrication technique)*. Imperial Journal of Interdisciplinary Research (IJIR), 2(8), 972-984.
- [84] Chorkendorff, I., & Niemantsverdriet, J. W. (2017). *Concepts of modern catalysis and kinetics*. John Wiley & Sons.
- [85] Cornils, B., Herrmann, W. A., Xu, J. H., & Zanthoff, H. W. (2020). *Catalysis from A to Z: a concise encyclopedia*. John Wiley & Sons.
- [86] Zhang, F., Wang, X., Liu, H., Liu, C., Wan, Y., Long, Y., & Cai, Z. (2019). *Recent Advances and Applications of Semiconductor Photocatalytic Technology*. Applied Sciences, 9(12), 2489. DOI: 10.3390/app9122489
- [87] Koe, W. S., Lee, J. W., Chong, W. C., Pang, Y. L., & Sim, L. C. (2020). *An overview of photocatalytic degradation: Photocatalysts, mechanisms, and development of photocatalytic membrane*. Environmental Science and Pollution Research, 27(3), 2522-2565. DOI: 10.1007/s11356-019-07193-5

- [88] Ahmad, H., Kamarudin, S. K., Minggu, L. J., & Kassim, M. (2015). *Hydrogen from photo-catalytic water splitting process: A review*. Renewable and Sustainable Energy Reviews, 43, 599-610. DOI: 10.1016/j.rser.2014.10.101
- [89] Saraswat, S. K., Rodene, D. D., & Gupta, R. B. (2018). *Recent advancements in semiconductor materials for photoelectrochemical water splitting for hydrogen production using visible light*. Renewable and Sustainable Energy Reviews, 89, 228-248. DOI: 10.1016/j.rser.2018.03.063
- [90] Eidsvåg, H., Bentouba, S., Vajeeston, P., Yohi, S., & Velauthapillai, D. (2021). *TiO₂ as a Photocatalyst for Water Splitting—An Experimental and Theoretical Review*. Molecules, 26(6), 1687. DOI: 10.3390/molecules26061687
- [91] Osterloh, F. E. (2008). *Inorganic Materials as Catalysts for Photochemical Splitting of Water*. Chemistry of Materials, 20(1), 35-54. DOI: 10.1021/cm7024203
- [92] Lun, M., Zhou, X., Hu, S., Hong, Y., Wang, B., Yao, A., Li, W., Chu, B., He, Q., Cheng, J., & Wang, Y. (2021). *Ferroelectric K_{0.5}Na_{0.5}NbO₃ catalysts for dye wastewater degradation*. Ceramics International, 47(20), 28797-28805. DOI: 10.1016/j.ceramint.2021.07.040
- [93] Praxedes, F. R., Nobre, M. A. L., Poon, P. S., Matos, J., & Lanfredi, S. (2021). *Nanostructured K_xNa_{1-x}NbO₃ hollow spheres as potential materials for the photocatalytic treatment of polluted water*. Applied Catalysis B: Environmental, 298, 120502. DOI: 10.1016/j.apcatb.2021.120502
- [94] Wang, K., Han, C., Li, J., Qiu, J., Sunarso, J., & Liu, S. (2022). *The Mechanism of Piezocatalysis: Energy Band Theory or Screening Charge Effect?* Angewandte Chemie International Edition, 134, e202110429 (1-13). DOI: 15081
- [95] Tu, S., Guo, Y., Zhang, Y., Hu, C., Zhang, T., Ma, T., & Huang, H. (2020). *Piezocatalysis and Piezo-Photocatalysis: Catalysts Classification and Modification Strategy, Reaction Mechanism, and Practical Application*. Advanced Functional Materials, 30, 2005158(1-31). DOI: 10.1002/adfm.202005158

- [96] Kausar, A. (2021). *Polymeric nanocomposite via electrospinning: Assessment of morphology, physical properties and applications*. Journal of Plastic Film & Sheeting, 37(1), 70-92. DOI: 10.1177/8756087920937344
- [97] Rodríguez-Carvajal, J. (2001) *Recent Developments of the Program FULLPROF*, in Commission on Powder Diffraction (IUCr). Newsletter, 26, 12-19.
- [98] Orayech, B., Faik, A., López, G. A., Fabelo, O., & Igartua, J. M. (2015). *Mode-crystallography analysis of the crystal structures and the low- and high-temperature phase transitions in Na_{0.5}K_{0.5}NbO₃*. Journal of Applied Crystallography, 48(2), 318-333. DOI: 10.1107/S1600576715000941
- [99] Zhang, L., Hou, Y., Zheng, M., Zhu, M., & Yan, H. (2015). *Microstructure and low-temperature relaxor behavior of dense K₂Nb₄O₁₁ ceramics derived from sol-gel route*. Materials Chemistry and Physics, 149, 418-423. DOI: 10.1016/j.matchemphys.2014.10.039
- [100] Acker, J., Kungl, H., & Hoffmann, M. (2010). *Influence of alkaline and niobium excess on sintering and microstructure of sodium-potassium niobate (K_{0.5}Na_{0.5})NbO₃*. Journal of the American Ceramic Society, 5(93), 1270-1281. DOI: 10.1111/j.1551-2916.2010.03578.x
- [101] Jenko, D., Bencan, A., Malic, B., Holc, J. & Kosec, M. (2005). *Electron Microscopy Studies of Potassium Sodium Niobate Ceramics*. Microscopy and Microanalysis, 11, 572-580. DOI: <https://doi.org/10.1017/S1431927605050683>
- [102] Scherrer, P. (1918). *Nachrichten von der Gesellschaft der Wissenschaften zu Göttingen, Mathematisch-Ph: "Bestimmung der Größe und der inneren Struktur von Kolloideteilchen mittels Röntgenstrahlen"*. Weidmannsche Buchhandlung, page 98.
- [103] Toby, B. H. (2006). *R factors in Rietveld analysis: How good is good enough?* Powder Diffraction, International Centre for Diffraction Data, 21(1), 67-70. DOI: 10.1154/1.2179804

- [104] Schneider, C. A., Rasband, W. S., & Eliceiri, K. W. (2012). *NIH Image to ImageJ: 25 years of image analysis*. *Nature Methods*, 9(7), 671–675. DOI: 10.1038/nmeth.2089
- [105] Makuła, P., Pacia, M., & Macyk, W. (2018). *How To Correctly Determine the Band Gap Energy of Modified Semiconductor Photocatalysts Based on UV-Vis Spectra*. *Journal of Physical Chemistry Letters*, 23(9), 6814-6817. DOI: 10.1021/acs.jpclett.8b02892
- [106] Oancea, A., Grasset, O., Le Menn, E., Bollengier, O., Bezacier, L., Le Mouélic, S., & Tobie, G. (2012). *Laboratory infrared reflection spectrum of carbon dioxide clathrate hydrates for astrophysical remote sensing applications*. *Icarus*, 2(221), 900-910. DOI: 10.1016/j.icarus.2012.09.020
- [107] Cantão, F., Melo, W., Oliveira, L., Passos, A., & Silva, A. (2010). *Utilization of Sn/Nb₂O₅ composite for the removal of methylene blue*. *Quimica Nova*, 33. DOI: 10.1590/S0100-40422010000300007
- [108] Saha, M., Niranjana, M. K., & Asthana, S. (2024). *Polarized Raman, infrared and dielectric spectra of lead-free K_{0.5}Na_{0.5}NbO₃ piezoelectric system: insights from ab-initio theoretical and experimental studies*. *Journal of Physics: Condensed Matter*, 36, 425703(1-15). DOI: 10.1088/1361-648X/ad61aa
- [109] Kakimoto, K. I., Akao, K., Guo, Y. & Ohsato, H. (2005). *Raman Scattering Study of Piezoelectric (Na_{0.5}K_{0.5})NbO₃-LiNbO₃ Ceramics*. *Japanese Journal of Applied Physics*, 44(9B), 7064-7067. DOI: 10.1143/JJAP.44.7064
- [110] Dwivedi, S., Pareek, T., & Kumar, S. (2018). *Structure, dielectric, and piezoelectric properties of K_{0.5}Na_{0.5}NbO₃-based lead-free ceramics*. *Royal Society of Chemistry Advances*, 8, 24286. DOI: 10.1039/c8ra04038a
- [111] Wojdyr, M. (2010). *Fityk: a general-purpose peak fitting program*. *Journal of Applied Crystallography*, 43, 1126-1128. DOI: 10.1107/S0021889810030499
- [112] Mathur, R., Bahl, O., Mittal, J., & Nagpal, K. (1991). *Structure of thermally stabilized PAN fibers*. *Carbon*, 29, 1059-1061. DOI: 10.1016/0008-6223(91)90189-P

- [113] Lee, S., Kim, J., Ku, B., Kim, J., & Joh, H. (2012). *Structural Evolution of Polyacrylonitrile Fibers in Stabilization and Carbonization*. *Advances in Chemical Engineering and Science*, 02(02), 275-282. DOI: 10.4236/aces.2012.22032
- [114] Doumeng, M., Berthet, F., Delbé, K., Marsan, O., Denape, J., & Chabert, F. (2021). *Effect of size, concentration, and nature of fillers on crystallinity, thermal, and mechanical properties of polyetheretherketone composites*. *Journal of Applied Polymer Science*, e51574(1-19). DOI: 10.1002/app.51574
- [115] Gupta, A., & Harrison, I. R. (1996). *New aspects in the oxidative stabilization of PAN-based carbon fibers*. *Carbon*, 34(11), 1427-1445. DOI: 10.1016/S0008-6223(96)00094-2
- [116] Qin, X., Lu, Y., Xiao, H., & Pan, D. (2011). *Improving preferred orientation and mechanical properties of PAN-based carbon fibers by pretreating precursor fibers in nitrogen*. *Carbon*, 49, 4595-4607. DOI: 10.1016/j.carbon.2011.06.011
- [117] Dang, W., Liu, J., Wang, X., Yan, K., Zhang, A., Yang, J., Chen, L., & Liang, J. (2020). *Structural Transformation of Polyacrylonitrile (PAN) Fibers during Rapid Thermal Pretreatment in Nitrogen Atmosphere*. *Polymers*, 12, 63(1-12). DOI: 10.3390/polym12010063
- [118] Torres-Giner, S., & Lagaron, J. M. (2010). *Zein-Based Ultrathin Fibers Containing Ceramic Nanofillers Obtained by Electrospinning. I. Morphology and Thermal Properties*. *Journal of Applied Polymer Science*, 118, 778-789. DOI: 10.1002/app.32180
- [119] Molnár, K., Szolnoki, B., Toldy, A., & Vas, L. M. (2014). *Thermochemical stabilization and analysis of continuously electrospun nanofibers*. *Journal of Thermal Analysis and Calorimetry*, 117, 1123-1135. DOI: 10.1007/s10973-014-3880-6
- [120] Zhang, Z., Wu, X., Kou, Z., Song, N., Nie, G., Wang, C., Verpoort, F., & Um, S. (2022). *Rational design of electrospun nanofiber-typed electrocatalysts for water splitting: A review*. *Chemical Engineering Journal*, 428, 131133. DOI: 10.1016/j.cej.2021.131133

- [121] Sang, L., Yang, W., Gao, S., Li, S., Ku Shang, J., & Li, Q. (2022). *Photocatalytic activity of polyacrylonitrile under simulated solar illumination*. Chemical Engineering Journal, 434, 134697. DOI: 10.1016/j.cej.2022.134697
- [122] Tao, J., Wang, Y., Zheng, X., Zhao, C., Jin, X., Wang, W., & Lin, T. (2023). *A review: Polyacrylonitrile as high-performance piezoelectric materials*. Nano Energy, 118, 108987. DOI: 10.1016/j.nanoen.2023.108987
- [123] Qu, P., Zhao, J., Shen, T., & Hidaka, H. (1997). *TiO₂-assisted photodegradation of dyes: A study of two competitive primary processes in the degradation of RB in an aqueous TiO₂ colloidal solution*. Journal of Molecular Catalysis A: Chemical, 129, 257-268. DOI: 10.1016/S1381-1169(97)00185-4